THE THESIS OF DOCTOR OF PHILOSOPHY

Study on an Amphibious Father-son Robotic System

Maoxun Li

Graduate School of Engineering
Kagawa University

Abstract

With the increasing needs for underwater intervention tasks, underwater vehicles have been extensively applied in intervention missions instead of human. To implement the underwater intervention, a father-son robotic system was proposed, which is composed of an amphibious father robot and several microrobots used as the manipulators of the system. We have described a spherical robot configuration for amphibious applications. The amphibious robot can move with a relatively high velocity and for a relatively long period of time on land and underwater. Furthermore, by carrying the microrobot, the robot can be employed to do the sample collections and monitoring in an underwater space.

An amphibious spherical robot that consists of a sealed upper hemispheroid, two quarter spherical shells, and a plastic circular plate was proposed. It has a plastic shelf for carrying the microrobots, and four actuating units for movement. Each unit is composed of a water-jet propeller and two servomotors, each of which can rotate 90º in the horizontal and vertical directions. The robot is capable of motion on land, as well as underwater. A braking mechanism is designed to transform the state of each passive wheel between free rolling and braking states by compressing and releasing the spring, which is controlled by the vertical servo motor on each leg. Besides, in order to improve the walking stability of the wheeled robot in longitudinal direction, a closed-loop control method is presented to control the stability of the direction of movement while walking.

The on-land experiments on smooth flat surface and on a slope were carried on to evaluate the on-land performance of the amphibious robot. At low frequencies, the sliding velocity and walking velocity on the flat terrain were roughly equal. At a control frequency of 5.56 Hz, we got a maximum roller-skating velocity of 37.8 cm/s. And the robot was able to move down a slope with an incline of 10 ° with roller-skating gait. Roller-skating gait showed a better performance than walking gait in terms of mobile velocity and energy efficiency, especially moving down a slope.

Since there is a different step loss for four legs during walking, the direction of movement of the robot is unstable. For the improvement of the walking stability of the wheeled robot in longitudinal direction, we proposed a closed-loop control method by carrying a gyroscope sensor to measure the yaw angle of the robot in real time. And plenty of walking experiments were conducted to evaluate a good performance of directional control.

Additionally, underwater thrust and velocity experiments in the semi-submerged state were conducted to evaluate the underwater performance. Under a duty of 100%, we got a maximum thrust of 180 mN in horizontal direction, and a maximum upward thrust of 333.2 mN and a downward thrust of 362.6 mN in vertical direction. And a maximum surge velocity of 16.1 cm/s and rotational velocity of 64.3 °/s were obtained, and a maximum rising velocity of 8.4 cm/s and a sinking velocity of 8.4 cm/s were achieved. Furthermore, the microrobot deployment experiment was carried out to prove the feasibility of the fixture and deployment mechanism.

As the crucial equipment of underwater vehicles, underwater manipulators typically play an important role in the underwater tasks. An ICPF actuator-based crayfish-like son robot has been developed to be adopted as the manipulator of the father-son robot system. The son robot is actuated by ten ICPF actuators, which can perform walking, rotating and grasping motions underwater. A proximity sensor and two photodiodes are mounted in front of the microrobot to implement the functions of autonomous grasp and blue LED tracking. A blue LED-based underwater optical communication system is designed to enable the communication between father robot and son robot for the microrobot recovery.

The walking, rotating and grasping experiments are conducted to verify the performance of the basic motions of the robot. From the experimental results, a maximum walking speed of 18.6 mm/s and a maximum rotational speed of 0.51 rad/s at a control frequency of 3 Hz are achieved. We also carry out the underwater experiments to evaluate the performance of the optical communication system, in which the blue LED and the photodiode are used as the transmitter and the receiver respectively. By measuring the detectable maximum distance of the photodiode at different input angles, we achieve the detectable range of the communication system. From the results of the blue LED-based tracking experiments, the microrobot can be recovered by the father robot.

And a biomimetic cableless microrobot has been developed as the manipulator of the father-son robot system. The microrobot actuated by nine ICPF actuators can implement the walking, rotating and grasping motions. A blue LED-based underwater optical communication method was proposed to realize the communication between the father robot and the cableless son robot. The father robot is able to carry the cableless son robot and send the optical signals to control the motion of it according to the proposed communication protocol.

The walking and rotating experiments were conducted to evaluate the performance of the microrobot. From the experimental results, a maximum walking speed of 9.85 mm/s and rotational speed of 13.13 º/s were achieved at a control frequency of 1.25 Hz. Finally, the communication experiments were carried out to verify that the proposed communication protocol can be used for the communication between the father and son robot.

Contents

List of Table

List of Figures

Acknowledgements

The author wishes to express her great gratitude to her supervisor Professor Shuxiang Guo for his invaluable guidance, support and friendly encouragement throughout her Ph.D. course and for providing her with first class resources. The author appreciates her supervisor not only for his guidance on the author's research, but also the great encouragement and help on the author's life.

The author would like to thank Prof. Hideyuki Hirata and Prof. Keisuke Suzuki. Thank them for their valuable advices and suggestion on her research. The author has improved the thesis greatly with their suggestions and advice.

Also the author would like to acknowledge the efforts of her laboratory members, especially Dr. Jin Guo and Dr. Chunfeng Yue whose time and expertise were greatly appreciated.

This research is supported by Kagawa University Characteristic Prior Research Fund 2012 and the author is supported by the Japanese Government (Monbukagakusho) Scholarship so that the author can pay more attention to her research. Here, the author would like to express her gratitude.

Finally, the author gives special appreciation to her parents and her husband Jin Guo for their love, patience and support.

Declaration

I hereby declare that this submission is my own work and that to the best of my knowledge and belief. It contains no material previously published or written by another person nor material which to a substantial extent has been accepted for the award of any other degree or diploma of the university or other institute of higher learning, except where due acknowledgment has been made in the text.

Chapter 1

Introduction

1.1 Thesis scope

Approximately 71% of the Earth's surface is covered by oceans, and there are a number of additional underwater environments, including rivers, lakes, moorlands, tanks, and pipelines. Because of the hazards of working in underwater environments, it is often desirable to use robots to carry out work instead of human beings.

Comparing with the robots moving on land, underwater robots are relatively difficult to design because they have the water proof issues, and more importantly, the hydraulics and kinetics analysis on them are much more complicated. However, with the development of the design skill, sensing and controlling technologies, underwater robots are applied more and more widely to the practical applications. Underwater robots have been used for several years in applications including submarine topography surveys, water-quality monitoring, pipeline cleaning, water sample collection, and recovering underwater objects.

Autonomous underwater vehicles (AUVs) and Remote Operated Vehicles (ROVs) are two main types of unmanned underwater vehicle (UUVs). Generally, ROV operations require an expensive mother ship, adequate deck support, and special expertise. Moreover, the tether limits the robots' positioning and manipulation performance. However, AUVs do not require a tether and continuous surface support, which leads to superior positioning performance and system management efficiency. Thus, AUVs can achieve a better positioning performance and a higher flexibility than ROVs. The conventional AUVs have the following features: (1) streamline and rectangular-shaped vehicles; (2) actuated by external screw-type thrusters; (3) high power consumption; (4) large size and heavy weight; (5) need to be shipped to the water.

Compared with AUVs, amphibious robots possess great abilities to adapt to various complex environments, on land and underwater. The amphibious robots move from the water to the ground without manpower, and vice versa. With a high adaptive faculty, amphibious robots can be used in broad applications including topography surveys, water-quality monitoring, sample collection, and recovering objects on land and underwater.

Different applications or tasks require the amphibious robots with different configurations, shapes, and sizes. As the crucial equipment of underwater vehicles, underwater manipulators typically play an important role in the underwater tasks. In order to implement the underwater missions, underwater vehicle-manipulator system has been proposed. The mechanical arm is a kind of conventional manipulator. By carrying the mechanical arms, amphibious robots can perform the underwater object recovery. However, the conventional manipulators are commonly enormous and they are mounted on a free floating vehicle platform. The weightlessness of a vehicle underwater is similar to that in space. During the underwater manipulation tasks, the underwater vehicle has to overcome the reaction from the mechanical arm in order to keep it in its position. Furthermore, considering the nonlinear and hydrodynamic coupling between the underwater vehicle and the mechanical arm, developing a control scheme is required to compensate for the movement of the vehicle induced by the movement of the arm, which increases the complexity of the control system.

Design and development of the amphibious robots involve different technologies, like mechanics, electronics, material science and hydrodynamics. Sensor, navigation, propulsion, and power systems are all essential components for amphibious robots. Typical sensors include compasses, depth sensors, proximity sensors, side-scan and other sonar devices, magnetometers, thermistors, and conductivity probes.

The propulsion system is one of the critical factors to evaluate the on-land and underwater performance of the amphibious robots, because it provides the basis of the control layers of the entire system. For underwater motions, amphibious robots rely on a number of propulsion techniques, such as paddlewheels, poles, magneto-hydrodynamic drives, sails, and oars. Until now, motor-based thrusters are the most common underwater propulsion system. These thrusters powered by electric motors are usually for actuating regular sized robots. And for the on-land motions, the amphibious robots are actuated by multi-articulated legs or wheels or leg-wheel hybrid actuation systems.

Wired and wireless controls are also one of the key factors for performance evaluation of the amphibious robots. Wired robots have the advantages of the adequate power supply and compact structure and effective communication; while, the tether restricts the positioning and performance of the robot. Also the lack of an umbilical cable limits the robot to its own power source, thus reducing the feasible mission duration. Most of the wireless amphibious robots in use today are powered by rechargeable batteries (lithium ion, lithium polymer, nickel metal hydride, etc.).

1.2 Literature review

Amphibians possess great abilities to adapt to various complex environments, both on land and underwater. Researches of the amphibious robots inspired by amphibians have been focused on by researchers around the world. With a high adaptive faculty, amphibious robots can be used in broad applications including topography surveys, water-quality monitoring, sample collection, and recovering objects on land and underwater.

As the typical amphibious robots, snake-inspired robots propel themselves through undulating their bodies on land and underwater.

ACM-R5, as shown in Figure 1-1, is one of the snake-like robots with good property of water-proof and high obdurability [1]. Unlike snake robots, a number of amphibious robots employ different propulsion methods to cope with different environments. The actuator of an amphibious robot named Whegs, as shown in Figure 1-2, is a combination of propellers and legs, which allows the robot to move on rough terrain and underwater [2]. AmphiRobot-II, as shown in Figure 1-3, is an amphibious biomimetic fish-like robot with a wheel–propeller–fin mechanism and a specialized swivel mechanism. [3]. More specifically, the wheel–propeller–fin mechanism functions as a driving wheel for crawling on land, as a common screw propeller or a pectoral fin in water. With the specialized swivel mechanism, AmphiRobot-II is able to freely switch between fish-like (lateral) and dolphin-like (dorsoventral) swimming motions. A salamander-like amphibious robot named Salamander Robot can mimic the ability of motion transformation from terrestrial to aquatic locomotion by utilizing body undulation and limb walking, and vice versa [4]. An amphibious mobile robot with a spherical rotary paddle mechanism is reported in Ref. [5]. The spherical rotary paddle mechanism functions as a rotary paddle in water, as a wheel for moving on land. The robot with “Omni-Paddle” can realize an effective movement on the border of ground and water. AQUA series robots are the most attractive ones among amphibious robots [6]. AQUA is a cockroach-inspired hexapod robot with splendid land performance. AQUA's legs are interchangeable: flippers for swimming and for limited walking along the beach, and rubber-treaded legs for walking. Figure 1-3 shows AmphiHex-I with a transformable fin-leg composite propulsion mechanism, which can pass through rough land, soft substrate and water simultaneously [7].

Figure 1- 1 ACM-R5 developed by Tokyo Institute of Technology [1]

Compared with underwater robots, amphibious robots are able to move from the water to the ground without manpower, and vice versa. Furthermore, each amphibious robot has its own characteristics and advantages. Wheeled robots have good performance on even ground, while tracked and legged robots have good mobility on rough terrain. Compared with screw propellers, undulatory and oscillatory propulsion with lower environmental disturbance can also achieve high efficiency and maneuverability. Some robots utilize two sets of propulsion mechanism for terrestrial and aquatic motions, which leads to a heavy body. To simplify the structure, robots like ACM-R5, Whegs and AQUA2 use composite propulsion mechanism to move in amphibious environments. However, it is still problematic for these amphibious robots to move in confined spaces. In order to improve mobility on the complex terrains, there are no manipulators carried on the existing amphibious robots for on-land and underwater operations. Moreover, it is difficult for these amphibious robots to achieve accurate control of position underwater through swimming motion. Once there are continuous currents under the sea, amphibious robots without legs cannot keep themselves still for precise manipulation.

Figure 1- 2 Whegs Case Western Reserve University, USA [2]

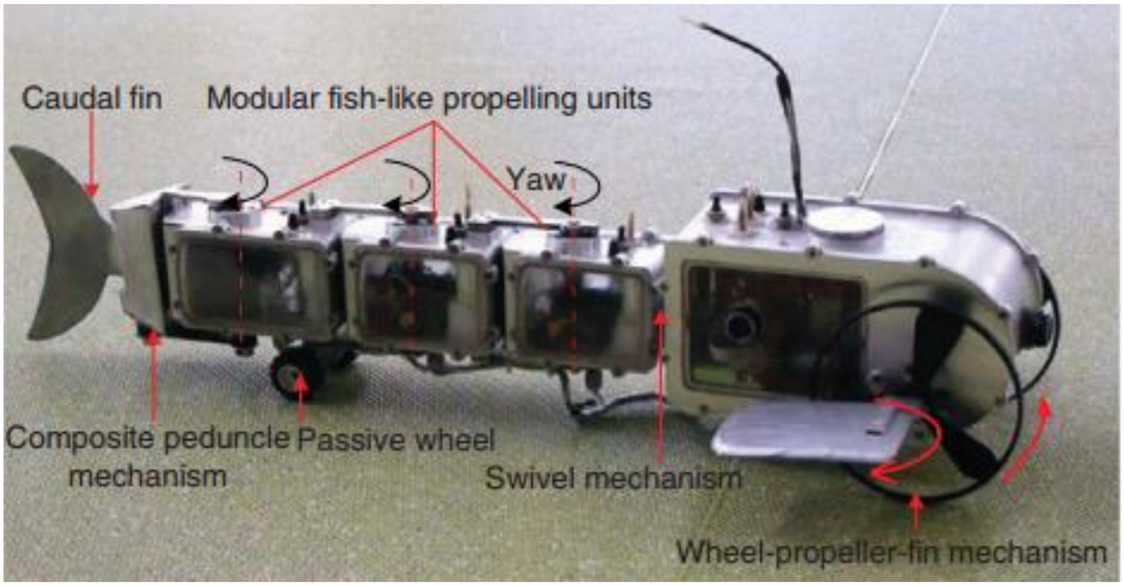

Figure 1- 3 AmphiRobot-II developed by Chinese Academy of Sciences [3]

Figure 1- 4 AmphiHex-I developed by University of Science and Technology of China [7]

For the on-land motions, many researches proposed the combination of the advantages of the locomotion of the legged robots and wheeled robots through leg-wheel hybrid vehicles. In the previous researches, some of the hybrid vehicles are equipped with driven wheels, while others are outfitted with passive wheels. Compared to active wheel-legged robots, passive wheel-legged robots have the advantages of low energy consumption and low weight and compact structure, because driving the active wheels requires actuators, which are usually heavy and bulky. Since the robot in walking mode is already heavy enough, equipping driven wheels will cause in a serious defect during walking.

As the early leg-wheel hybrid mobile robots, the passive wheel-legged robot named Roller-Walker with two actuating modes is proposed, as shown in Figure 1-5 [8]-[11]. The quadruped robot has one passive wheel on each leg, which can be transformed into sole mode by rotating the ankle roll joint. With this transformation mechanism, the locomotion can be switched from quadruped walking to roller-skating on the flat ground. Each leg has three degrees of freedom, one of which is just used for the transformation of the actuation modes. Body extendable quadruped robot (BEQR) is a novel wheel-legged robot with extendable body [12]. Each leg is equipped with a passive wheel and has four degrees of freedom. These two kinds of robots are actuated by passive wheels while roller-skating. Another leg-wheel hybrid platform named Quattroped is designed, which has two separate mechanisms, wheels and legs [13]. With a leg-wheel switching mechanism, the robot can implement the locomotion switching from the wheel mode to the leg mode by shifting the hip point out of the center of the rim. And a leg-track-wheel articulation-based robotic platform, AZIMUT, as shown in Figure 1-6, possessing abilities of adaptation to three-dimensional environments, is developed [14]. However, these two kinds of active wheel-legged robots are heavy and bulky because active wheels need to be driven by additional motors. And all the robots should consider their ability of directional control during walking.

And to implement the underwater tasks, underwater manipulators carried on the robots typically play an important role. Nowadays, only few AUVs are equipped with underwater manipulators. Figure 1-7 shows SAUVIM, which is capable of autonomous manipulation and can perform an autonomous underwater intervention in the oceanic environment [15]. And it completed an underwater recovery mission, which includes searching for the target and bringing it back to the surface. In addition, an underwater vehicle-manipulator system was used on an underwater robot with six degrees of freedom (DOF) [16] [17]. A 3-DOF underwater manipulator was mounted on the robot for underwater intervention. RAUVI, a reconfigurable AUV, was designed and developed for intervention, which was equipped with acoustic and optic sensors for the environmental perception and a robotic arm for simple tasks, as shown in Figure 1-8 [18]. These researches are relying on the multi-link arm to implement underwater missions. As a traditional manipulation system, the multi-link arm is appropriate for heavy-type work and continuous manipulation.

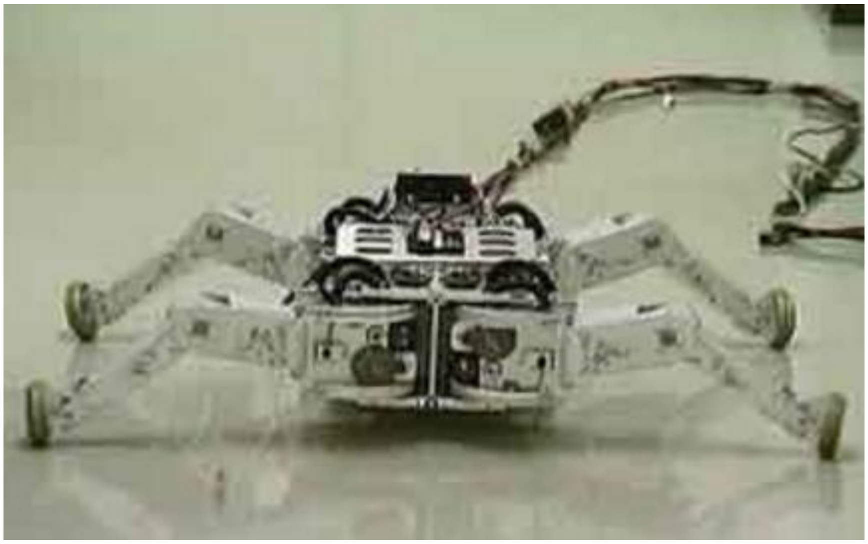

Figure 1- 5 Roller-Walker [8]-[11]

Figure 1- 6 AZIMUT [14]

Figure 1- 7 SAUVIM developed by University of Hawaii [15]

Figure 1- 8 RAUVI developed by University of Bologna [18]

To overcome these difficulties, some researchers begin to use a small, deployable and highly maneuverable ROV as the manipulator. A novel manipulation system concept was proposed for AUVs. An agent vehicle, as a manipulator, was developed to be connected to a main

AUV by a smart cable to implement underwater manipulations, which is very useful for the target not on the seabed [19]. As the size of the agent is slightly large, it is not suitable for the small-sized AUV. In our lab, a microrobot was designed as a grasper of FURIS to be connected to a small-sized AUV for underwater missions [20]. But since the microrobot can only realize the grasping motion, it is hard for the AUV to detect the target and control the microrobot to move to the position directly above the target. For these AUVs, performing the underwater tasks in restricted and complicated environments is more difficult.

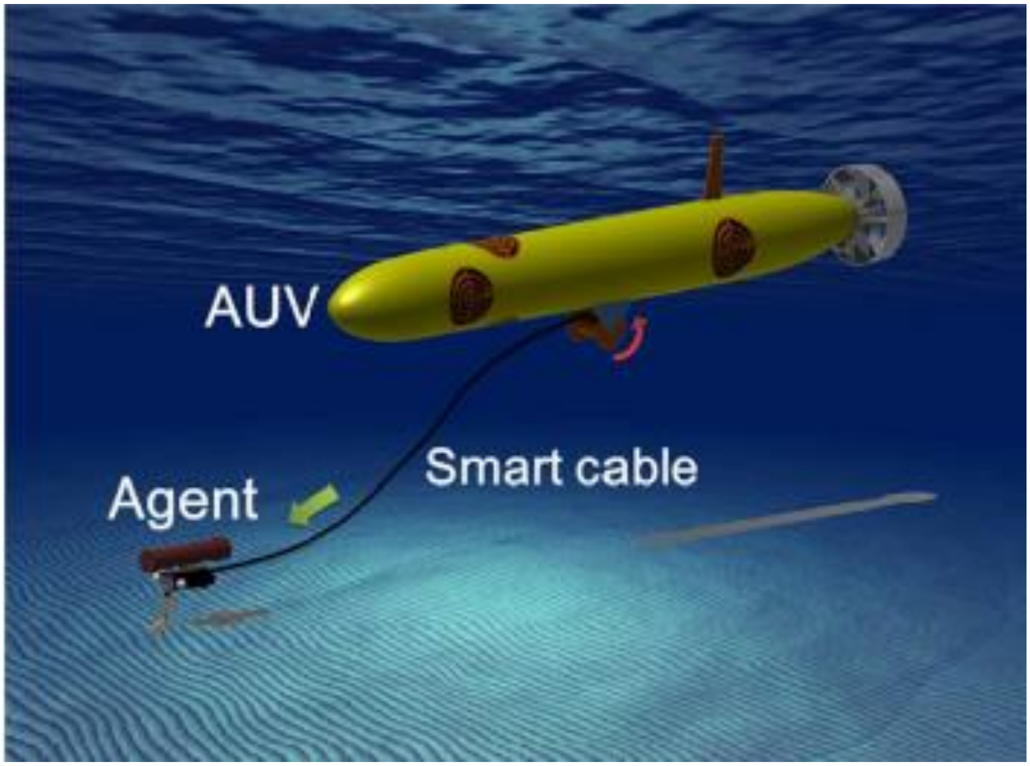

Figure 1- 9 The main vehical equipped with highly maneuverable agent ROV [19]

1.3 Thesis objectives

The objective of my research is to present a novel father-son robotic system for underwater intervention missions. In this system, an amphibious spherical robot is designed and developed as the father robot, which has three actuating modes. Two kinds of smart actuator-based biomimetic microrobots are developed as the son robots of the father-son robot system, which are mounted on the plastic plate in the lower hemisphere of the father robot to be used as the manipulators of the father robot.

1) To adapt to the complex underwater environments, an amphibious spherical father robot was developed with three actuating modes: quadruped walking mode, roller-skating mode and water-jet propulsion mode. To improve the walking stability, a closed-loop control method was employed to control the stability of the direction of movement.

2) To implement the underwater missions, two kinds of biomimetic son microrobots driven by smart actuators were developed as the manipulators of the father-son robotic system. Additionally, the release and recovery mechanisms of the manipulators were designed.

3) To realize the communication between the father robot and the wireless son robot, a blue LED-based underwater optical communication system was designed.

1.4 Thesis structure

Figure 1-10 shows the structure of the thesis. Chapter 1 is the introduction. It is composed of thesis scope, literature review, research purposes, research approaches and thesis structure. In chapter 2, overview of the father-son robotic system is introduced. The father-son robotic system is composed of an amphibious father, and several micro son robots developed as the manipulators of the system. Chapter 3 introduces the proposed amphibious spherical father robot. The amphibious father robot was designed and developed with three actuation modes to adapt to various complex environments, on land and underwater. In chapter 4, the on-land and underwater performance of the father robot was evaluated. And the performance of the robot was improved, including the obstacle avoidance ability and the control of the moving direction. In chapter 5, an insect-like cable son robot was developed as the manipulator of the father-son robotic system. Chapter 6 presented a biomimetic cableless son robot employed as the manipulator. And chapter 7 presents the deployment and recovery of the manipulator of the father robot. In chapter 8, conclusions and future work were given.

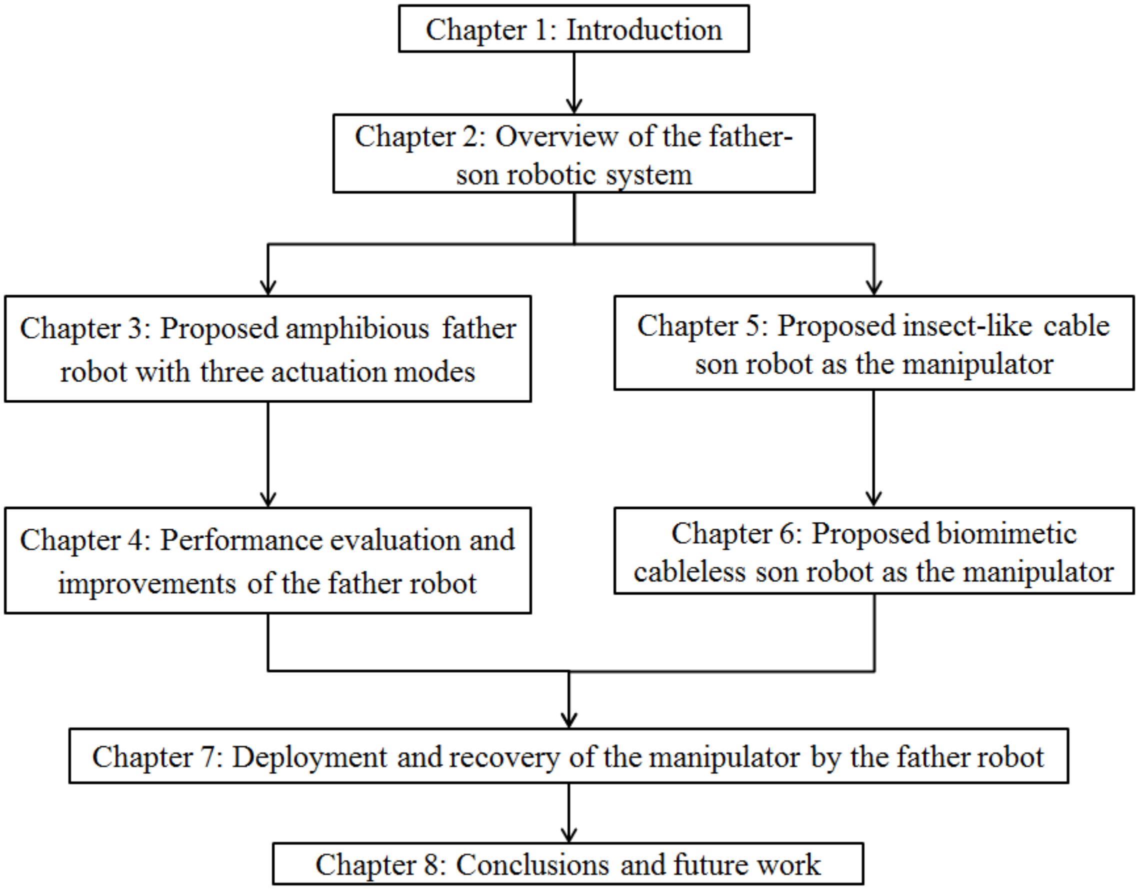

Figure 1- 10 The structure of the thesis

Chapter 2

Overview of the father-son robotic system

To implement the underwater intervention tasks, a father-son robotic system was proposed, which is composed of an amphibious father robot and several microrobots used as the manipulators of the system. The manipulators of the father robot include a cable son robot and a cableless son robot. The father robot with a high mobile velocity provides the power and sends control signals to the cable microrobot. And the father robot controls the cableless microrobot by the underwater optical communication system. With the ability of carrying microrobots actuated by smart actuators [23], [25], spherical robot can be employed to collect samples or carry out water-quality monitoring in a confined underwater space [19], [26]. Microrobots are used as the manipulators to grip objects underwater or a monitor to monitor the water quality and so on. The conceptual design of the father-son robotic system is shown in Figures 2-1 and 2-2.

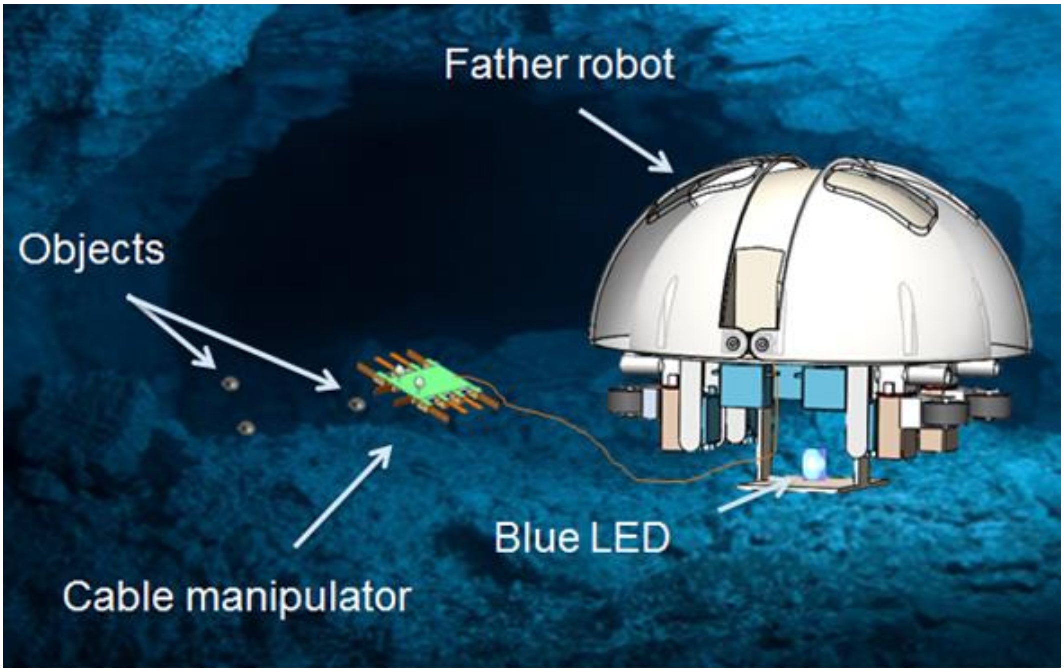

Figure 2- 1 The conceptual design of the father-son robotic system (cable son robot)

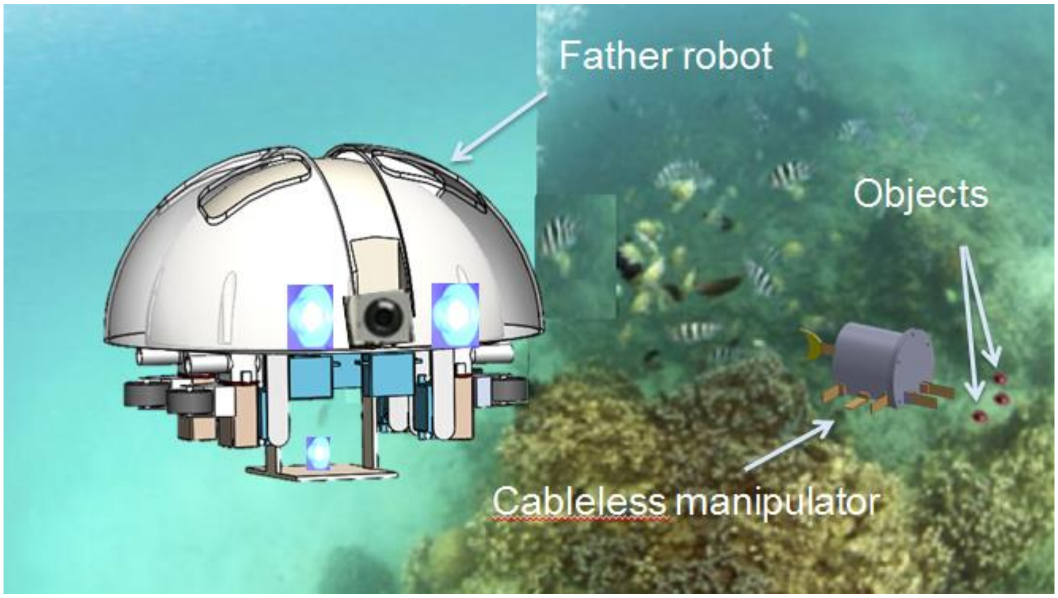

Figure 2- 2 The conceptual design of the father-son robotic system (cableless son robot)

2.1 The amphibious spherical father robot

Generally, underwater vehicles need to be shipped to the operation waters and recycled after underwater tasks. Compared with underwater robots, amphibious robots can walk from the ground to the water without shipping, and vice versa [6], [7]. A novel amphibious spherical robot with transformable composite propulsion mechanisms was designed and developed, which can control and carry microrobots. The composite mechanism is designed to switch between water-jet propeller, leg and wheel. A sphere provides maximum internal space, and symmetry of the spherical shape provides superiority of flexibility and no dynamic coupling [21], [22]. Figure 2-3 shows the father-son configuration.

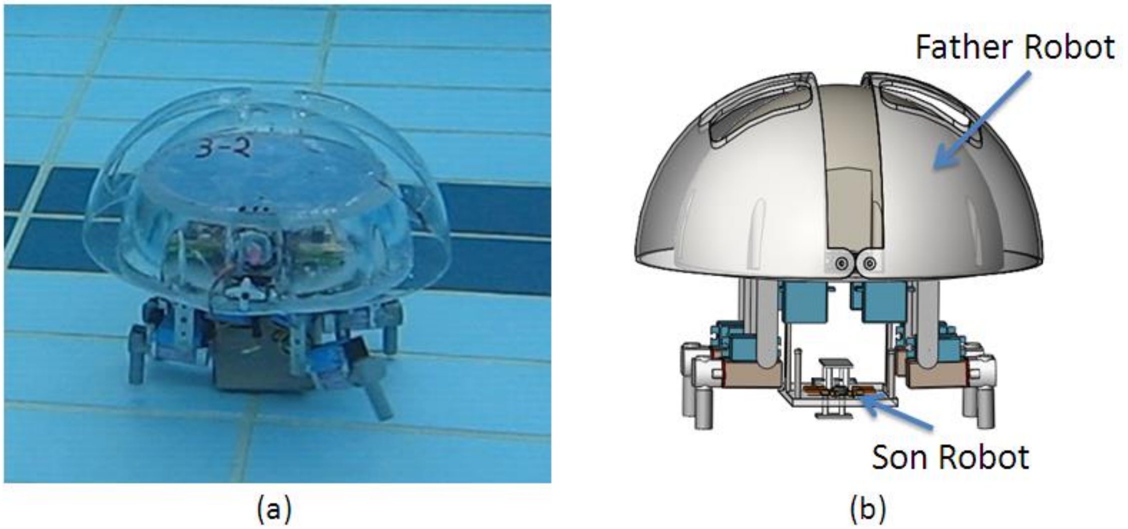

Figure 2- 3 Father-son robot configuration: (a) prototype of the amphibious father robot and (b) the conceptual design of the father-son robot system

2.2 The proposed son robots

When designing the microrobot, several constraints must be taken into account. First, as the holder on the amphibious robot for carrying microrobots has a finite size, the microrobot should be designed to be miniaturization. Second, since the father robot is a small-sized vehicle, it cannot provide too high energy for itself and the microrobots. Thus, the low-powered actuators are required for driving microrobots. Finally, in view of the implementation of the low power consumption, the microrobot should be light in weight.

According to the above restrictions, smart material-based microrobots are appropriate to be the mechanical arms of the father-son robot system. In contrast to traditional actuators, smart materials, like ionic conducting polymer film (ICPF), shape memory alloy (SMA), piezoelectric elements, and pneumatic actuator etc., can be employed as actuators directly and it is easy for them to realize the flexible movements with the advantages of small size and light weight. A fish-like biomimetic microrobot driven by SMA actuators was developed with a maximum speed of 112 mm/s [29]. And another fish-like robot used an ICPF actuator passive tail fin to mimic the swimming motion of the real fish [30]. Moreover, an ICPF actuator-based jellyfish-like robot utilized a balloon to regulate its buoyancy and an insect-like robot used ICPF actuators as legs for walking motions [23], [31].

Compared with other smart materials, ICPF actuators have the advantages of compact structure, low driving voltage, and low noise, ability of driving in water, soft characteristic, and quick response properties. Therefore, ICPF actuators are more suitable to drive the son robot of the father-son robot system. As swimming motion cannot realize a comparatively precise position control, designing a legged robot as the son robot is an excellent option for underwater tasks.

To realize the underwater object recovery, two kinds of the smart actuator-based biomimetic microrobots are developed as the son robots of the father-son robotic system, which are mounted on the plastic plate in the lower hemisphere of the father robot to be used as the manipulators of the father robot. One is an ICPF-actuated eight-legged cable microrobot, the other is an ICPF actuator-based cableless microrobot. The father robot sent the control signals and power supply to the cable son robot through cables and communicated with the cableless son robot through a proposed underwater optical communication system.

2.3 Summary

In this chapter, an amphibious father-son robotic system has been introduced. The system is consisted of an amphibious father robot and two kinds of microrobots employed as the manipulators of the robotic system. The father robot was developed with three actuation modes.

The cable son robot is controlled by the father robot through the cables; while, the cableless robot can communicate with the father robot through the underwater optical communication system.

Chapter 3

Proposed amphibious father robot with three actuation modes

3.1 General design

The design concept of the amphibious spherical robot is illustrated in Fig. 1. With transformable composite propulsion mechanisms, the robot has three actuating modes: water-jet propulsion mode, quadruped walking mode and roller-skating mode. The amphibious robot is capable of movement from the water to the ground without manpower, and vice versa. Underwater microrobots with flexible movement and compact structure are carried on the amphibious robot. The amphibious robot can provide power and send signals to cable microrobot with cables and control the cableless microrobot through the underwater optical communication system. Microrobots can be controlled to collect underwater objects as a manipulator or monitor underwater environment in a restricted space.

The amphibious robot consists of a sealed transparent upper hemispheroid, two transparent quarter spherical shells that can be opened, a plastic plate for carrying the micro-robots, and four actuating units, which are fastened to a plastic circular plate, as shown in Figure 3-1. The two quarter-spherical shells are controlled by two servomotors to open the shells by rotating them through an angle of 90º. The control circuits, power supply, and sensors are placed in the sealed upper hemispheroid, which is waterproof. The space in the lower hemisphere is connected to the outside environment via gaps on the hull. The plastic plate and actuating system are installed in the lower hemisphere. Each actuating unit consists of a water-jet propeller and two servomotors, which are perpendicular to each other, and can realize two degrees of freedom. The holes on the quarter spherical shell provide the space for the water-jet propellers to rotate to allow the robot to maneuver when it is closed. The diameter of the upper hemisphere is 234 mm, and the diameter of the lower hemisphere is 250 mm. The height of the actuating unit in the standing state is 108 mm, and it is 85 mm long.

Figure 3-2 shows the opening mechanism of the amphibious robot. The quarter spherical shells are mounted on two parallel axles, which are fixed to the upper hemisphere at a distance for independent control. From Figure 3-2, we can see that this structure avoids collisions between the two quarter-spherical shells and the upper hemisphere. The two axles are actuated by two JR DS3836 servomotors.

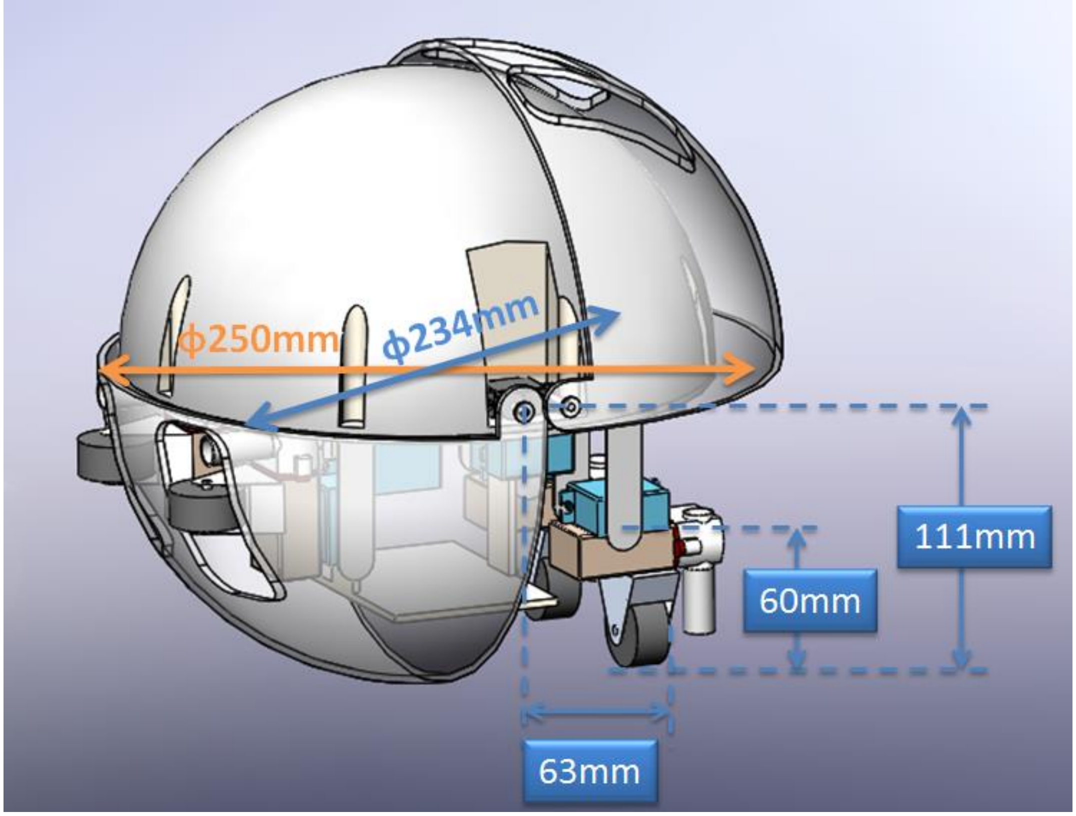

Figure 3- 1 Structure of the amphibious spherical robot

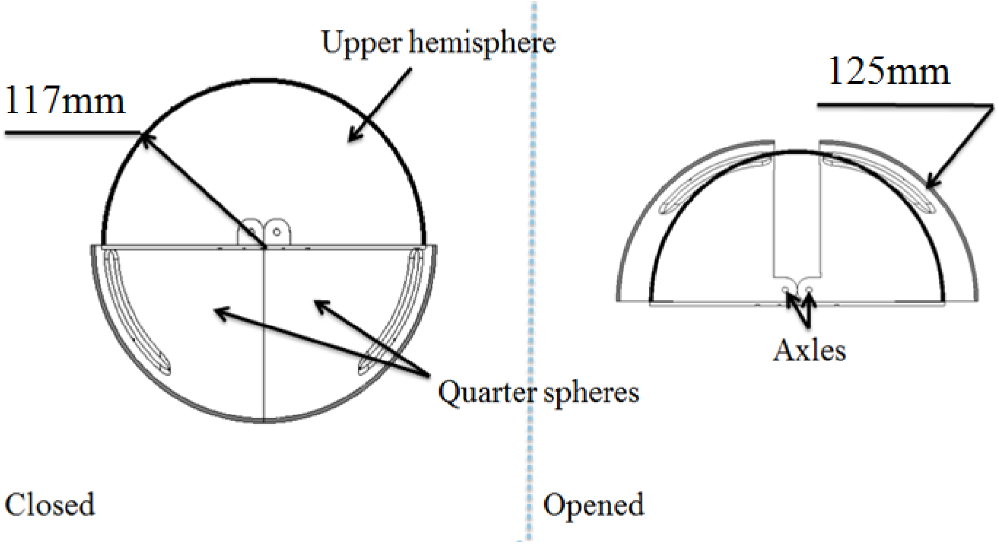

Figure 3- 2 Opening mechanism of the amphibious spherical robot

3.2 Actuation and control system

There are three actuation systems: a water-jet actuation system, a quadruped walking actuation system and a roller-skating actuation system [45]. The actuation system consists of four main units. Each unit includes a water-jet propeller, two servomotors, a passive wheel and a stainless-steel stand. The motor connected to the circular plate is controlled to move horizontally, and the motor fixed on the water-jet propeller is controlled to move vertically. Each unit has two degrees of freedom. Figure 3-3 shows the structure of the robot in three actuating modes.

3.2.1 Quadruped actuation system

The quadruped actuation was built to realize walking motion [24], [34]. Two servomotors, which are located on the surface of the plastic circular plate outside the upper hemisphere, are used to control the spherical shells.

To identify the appropriate servomotors for the legs of the robot, we carried out force analysis calculations. Figure 3-4 shows the force analysis of the robot on land. In the standing state, each vertical servomotor provides a torque $\boldsymbol{M_1}$. In the walking state, each vertical servomotor of the stationary legs provides a torque $\boldsymbol{M_2}$ and each horizontal servomotor of the moving legs provides a torque $\boldsymbol{M_3}$. Here, we assume that at a given moment, the supporting force on each leg in contact with the ground is the same. Considering that the torque on each servomotor cannot exceed the rated torque $\boldsymbol{M}$, we arrive at the following relationships:

$$mg = 4F_{N1} = 2F_{N2} \tag{Eq. 2-1}$$

$$\overrightarrow{M_1} = \overrightarrow{F_{N1}} \cdot l \tag{Eq. 2-2}$$

$$\overrightarrow{M_2} = \overrightarrow{F_{N2}} \cdot l \tag{Eq. 2-3}$$

The condition of frictional motion of each leg without longitudinal and transversal slipping is:

$$\left|\overrightarrow{M_3}\right| = \left|\vec{F}\right| \cdot s < \mu\left|\overrightarrow{F_{N2}}\right| \cdot s \tag{Eq. 2-4}$$

where F_{N1} and F_{N2} are the normal forces exerted on the surfaces, F is the force due to friction, μ is the coefficient of friction of the contact surface, l is the moment of the arm of the vertical motor, and s is the moment arm of the horizontal motor.

$$\max(M_1, M_2, M_3) < M \tag{Eq. 2-5}$$

The normal force F_N varies depending on the walking gait. The force F_{N1} is the minimum force that supports the robot; when robot stands with four legs, this is given by (Eq. 2-1). When the robot walks on land, there are times when only two or three legs are in contact with the ground. The supporting force F_{N2} is the maximum supporting force. We chose a servomotor that allows (Eq. 2-5) to hold.

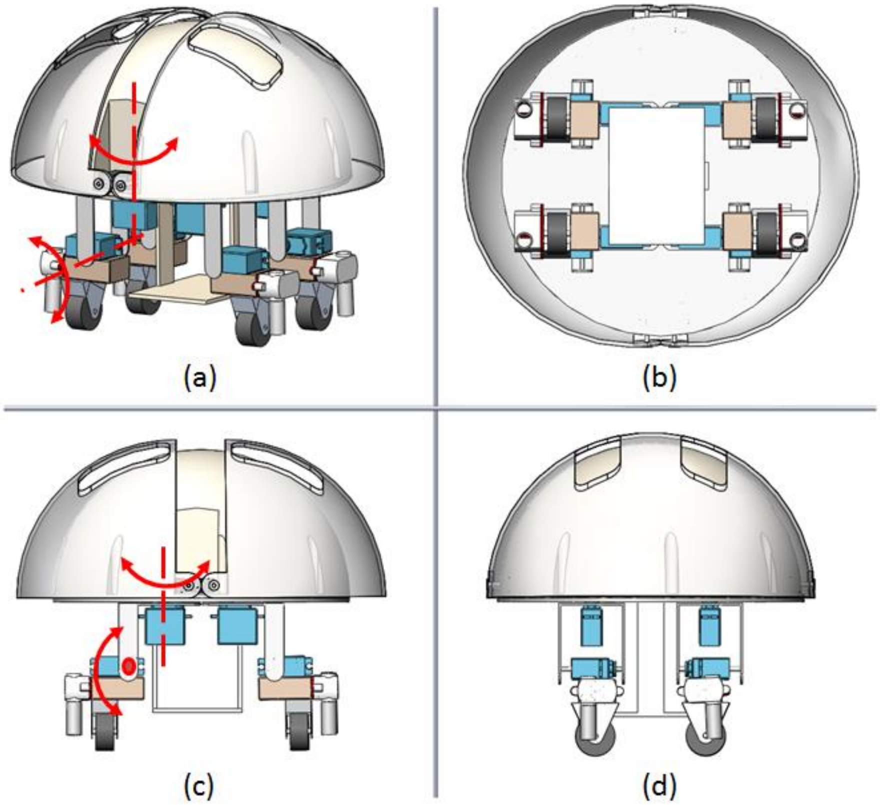

Figure 3- 3 Structure of the robot in three actuating modes: (a) overall structure, (b) bottom view, (c) front view and (d) side view

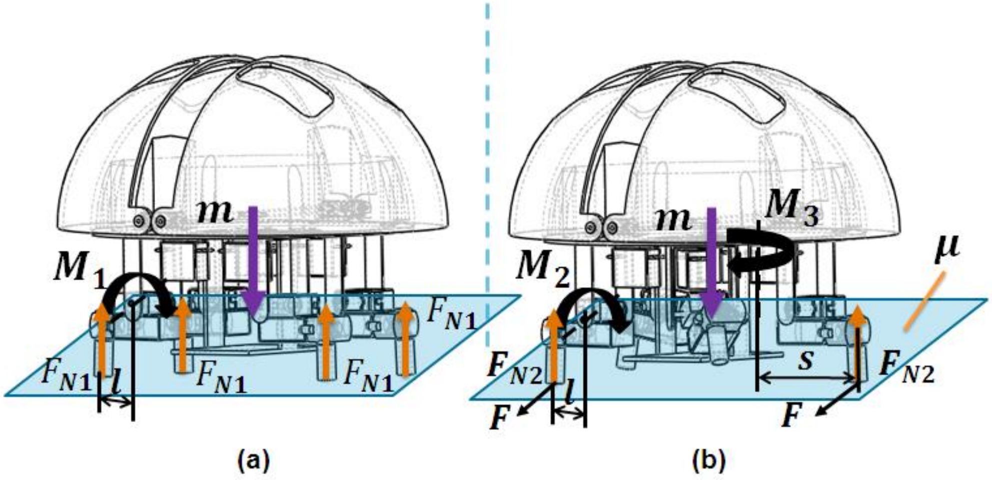

Figure 3- 4 Force analysis on land: (a) standing and (b) walking

To adapt to different environments, quadruped robots with two degrees of freedom in each leg may use a number of different gaits [38]. A proper walking gait has been implemented in the spherical robot. For this walking gait, the front leg is lifted while the ipsilateral hind leg is set down, which can achieve a good stability margin. And there are times when the robot has only two legs in contact with the ground. Accordingly, the gait event sequence and the gait timing can be defined by the duty factor β and the relative phase of the left-hind leg $\boldsymbol{\varphi}_{\mathbf{LH}}$. The relative phases of all the legs are defined so that $\boldsymbol{\varphi}_{\mathbf{LF}}$ = 0 and $\boldsymbol{\varphi}_{\mathbf{RF}}$ = 0.5; the right-hind (RH) leg has a phase difference of 0.5 relative to the left-hind (LH) leg. Figure 3-5 (a) shows the event sequences of the first gait with a duty factor of β = 0.67. The relative phases of the legs for the first gait are shown in Figure 3-5 (b).

The velocity of the robot is related to the step size and frequency of the gait cycle, i.e.,

$$v = d * f \qquad \text{(Eq. 2-6)}$$

where v is the velocity of the robot, d is the step size of the robot, f is the frequency of one step cycle. The step size is proportional to the angle of rotation of the leg, which is the given by the angle of rotation of the horizontal motor and the duty factor of the gait-timing sequence, i.e.,

$$d = (\frac{\theta}{180} * \pi * s)/\beta = 0.1483 * \theta/\beta \qquad \text{(Eq. 2-7)}$$

where β is the duty factor of the gait-timing sequences, and θ is the rotation angle of the horizontal motor.

Substituting (Eq. 2-7) into (Eq. 2-6), we can achieve the following:

$$v = 0.1483 * \theta * f/\beta \qquad \text{(Eq. 2-8)}$$

which is related to the frequency and the duty factor of the gait cycle.

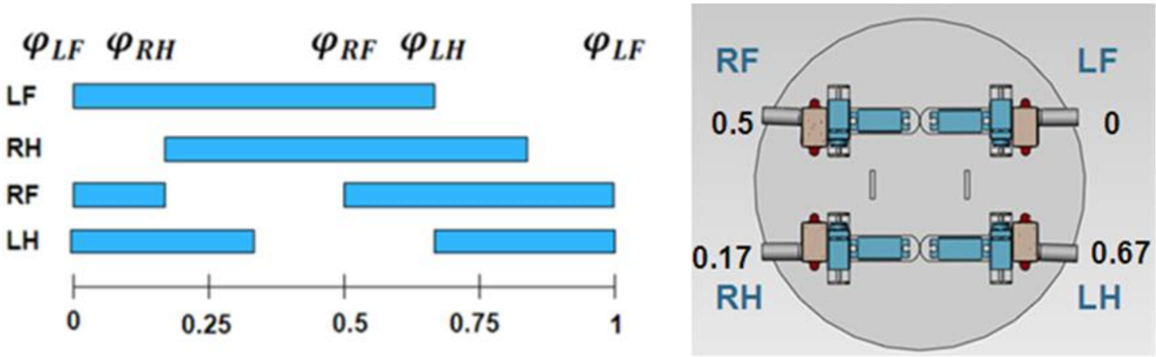

(a) (b)

Figure 3- 5 Event sequences (a) and relative phases (b) of one gait cycle for the walking gait

3.2.2 Roller-skating actuation system

Roller-skating uses wheels initially to provide pushing force by exploiting high lateral ground reaction forces and subsequently to reduce friction along the direction of motion, which allows the subject to slide forward. In the moving range of legs, there are a large number of possible trajectories. In a classic roller-skating motion, the human skater pushes one leg out and then makes it get full extension. In this process, the other leg is used as a supporter with its passive wheel freely rotating until the skater recovers the preceding extended leg to its starting position. The two legs drive the skater alternately and each leg pushes off the ground consistently in one direction (e.g. the right leg only moves to the right) [35].

A roller-skating gait proposed for the quadruped robot is inspired by the classic roller skating motion of human being. In the initial state of the skating motion, all the legs should keep vertical to the ground and should be aligned with the direction of motion of the robot. In the skating process, two front legs remain in contact with the ground at all times with the horizontal and vertical servo motors fixed at a constant angle and keep the rolling surface of each wheel facing forward; two rear legs implement the pushing movement periodic alternately. When one rear leg is actuated to push the ground, the rotational angle of the two servo motors of the other rear leg is fixed and the leg keeps its wheel’s rolling surface facing forward as the front legs. For the sliding forward motion, two rear legs are controlled by the robot to implement an alternately cyclical motion with at least three wheels facing forward at any one time, which indicates that the robot’s center of gravity must remain inside a polygon formed by the supporting legs.

With roller-skating gait, the front legs only have one phase, the free rolling phase; while the rear legs have three phases, including the free rolling, sliding and propulsion phases. In the free rolling phase, the leg remains stationary and the passive wheel rotates freely around the axle which is fixed at a right angle to the leg. In the sliding phase, the horizontal servo motor of the rear leg will rotate 60 ° anti-clockwise, while the vertical motor will rotate 20 ° anti-clockwise. During this period, due to the low friction generated by the rolling motion of the wheel, the friction resistance can be overlooked or ignored. In the propulsion phase, the rotational angle of the horizontal motor remains the same as the final state in the sliding phase and the vertical motor will rotate 40 ° clockwise to produce driving force for the robot, as shown in Figure 3-6. Assuming that there is no slip in the propulsion phase, the friction force formed by relative motion between the moving wheel and the ground, as the driving force of the robot in roller-skating mode, can be expressed as follows:

$$f(t) = F_2(t) = F \cdot cos\,\theta(t) = \frac{T}{h} \cdot cos\,\theta(t) \qquad \text{(Eq. 2-9)}$$

$$F_r(t) = f(t) = \frac{T}{h} \cdot cos\,\theta(t) \qquad \text{(Eq. 2-10)}$$

where $f(t)$ is the friction force generated by the vertical servo motor, T is the rated torque of the servo motor, h is the moment arm, $F_r(t)$ is the driving force of the robot, $\theta(t)$ is the amplitude of the swing angle around the axis of vertical servo motor, θ_m is the maximum amplitude, and μ is the friction coefficient between the wheel and ground.

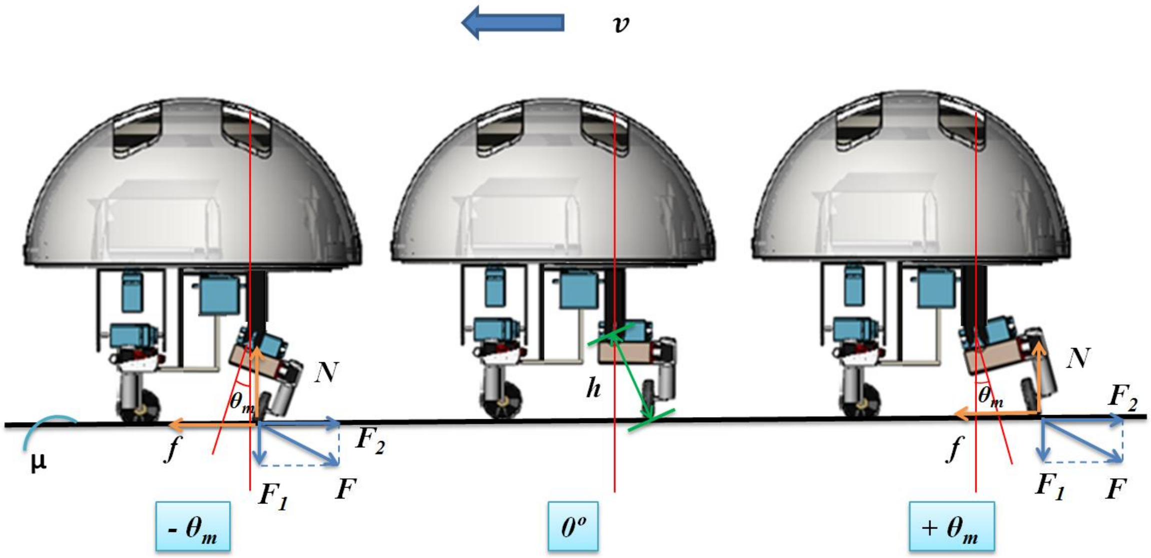

Figure 3- 6 Force analysis in the propulsion phase (side view). The blue arrows indicate the direction of the force applied on the ground by robot. The orange arrows indicate the direction of the force applied on the wheel of the robot by ground

The resultant force F_r is the driving force while roller-skating. However, the resultant force acting along the ground plane can be summarized as the longitudinal force to actuate the robot to slide forward and the transversal force to generate a lateral displacement as shown in Figure 3-7. Due to the presence of the transversal force, the robot will not go straight exactly. The force imposed by the left rear leg is the same with that formed by the right rear leg at any position. Consequently, the robot will move along a wave trajectory, as shown in Figure 3-8 (a). The wave trajectory can be fixed by the amplitude and frequency of the swing motion of each rear leg. Due to the symmetry, the transversal reaction force generated by the two rear legs can be counteracted after finished one-cycle sliding motion. Therefore, the robot will move to a destination right ahead. The longitudinal force and the transversal force can be obtained as follows:

$$F_{r1}(t) = F_r(t) \cdot \sin\alpha(t) \qquad \text{(Eq. 2-11)}$$

$$F_{r2}(t) = F_r(t) \cdot \cos\alpha(t) \qquad \text{(Eq. 2-12)}$$

where $F_{r1}(t)$ is the driving force acting parallel to the robot's moving direction, $F_{r2}(t)$ is the driving force acting perpendicularly to the moving direction, α is the maximum amplitude of the swing angle around the axis of horizontal servo motor.

Utilizing alternating movements of two rear legs, the robot can realize the sliding forward motion with the rolling surfaces of the front wheels facing forward. Since the rear legs can produce an actuating force through pushing off the ground, the robot can make turns by steering the front legs. During the turning motion, the horizontal servo motors of the two front legs are controlled to rotate clockwise or anticlockwise to change the turning direction.

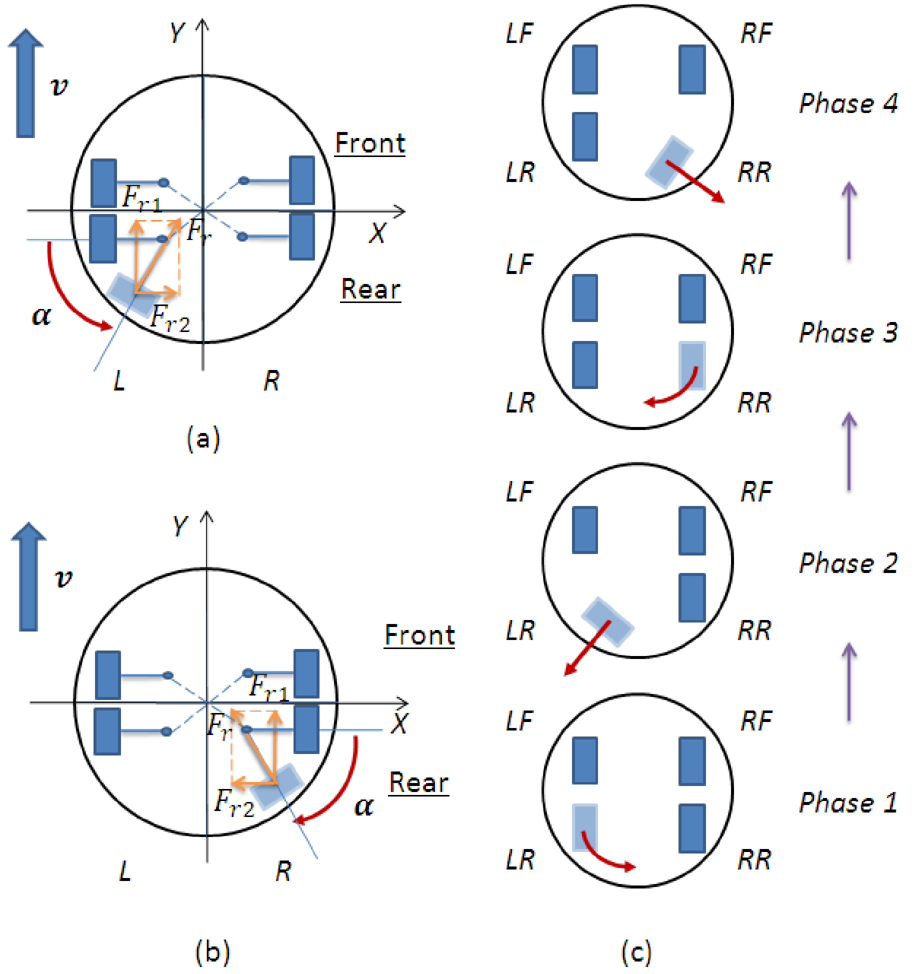

Figure 3- 7 Ground reactive force analysis on (a) left rear wheel and (b) right rear wheel while roller-skating and (c) gait cycle diagram in sliding and propulsion phases (top view). Phase 1 and 3 are sliding phases; phase 2 and 4 are propulsion phases. The legs are labeled as follows: left fore (LF), right fore (RF), left rear (LR), and right rear (RR). The light blue rectangle indicates the driven leg moving with three degrees of freedom, while the dark blue one indicates the leg moving with passive degree of freedom. The red arrow indicates the direction of movement of the rear wheel

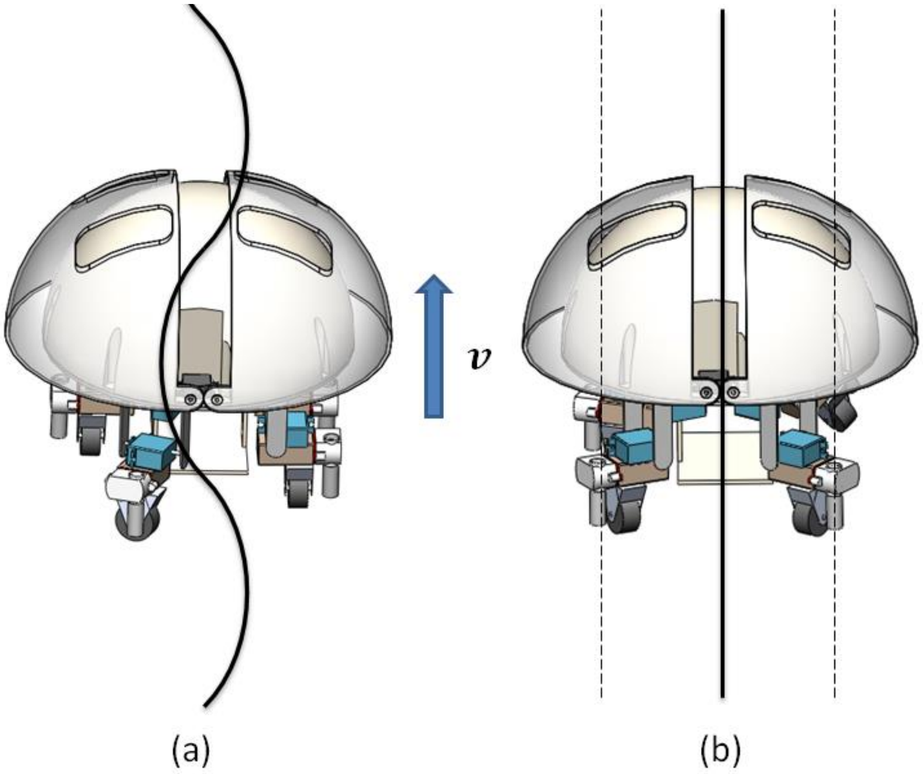

Figure 3- 8 Leg trajectory when (a) roller-skating and (b) walking

3.2.3 Braking/Transformation Mechanism

From the images segmented by the level set equation, a skeletonization technique is applied to obtain the vessels centerlines. This process allows our simulator to efficiently perform collision detection and blood flow computation by supplying an abstract topological representation of the vascular network.

As we mentioned , two front legs remain their initial positions at any time while sliding and two rear legs perform the pushing movements alternately. In a classic braking motion for roller-skating, the human skaters drag the toe stop along the ground to produce a resistance along the direction of motion or change their pose to a pigeon-toed pose to slow down. Since a human ankle has three active degrees of freedom, human can realize these two braking motions quickly and easily. However, it is difficult for the quadruped robot to stop with these two methods due to the wheel part only having one passive degree of freedom. Therefore, a braking mechanism is required to stop the robot instead of the traditional ways.

Adding braking equipment for each leg will cause serious weight increment and volume increases on the robot. Since the robot has a compact structure and actual torque of servo motor is limited according to the rated torque, additional braking equipment should not be carried on the robot's legs. Accordingly, a novel braking mechanism of wheel is proposed to implement the braking motion, as shown in Figure 3-9. Using this mechanism, no more additional devices are needed for braking motion. By changing the rotational angle of the vertical servo motor, the robot can apply brake and loose brake.

Figure 3-9 (b) shows the proposed braking equipment, which is composed of a fulcrum, a spring, a plastic plate, a rigid wire and a rubber. The rough rubber is used as a brake pad to be squeezed against the wheel. The rigid wire linked to the end of the plate is connected to the vertical motor bracket, as shown in Figure 3-10 (a). When the rigid wire is in a tight state, the spring is compressed to separate the rubber from the wheel, which implements a free rolling for the passive wheel. When the rigid wire is in a loose state, the compressed spring will apply an elastic force on the rubber to make the rubber contact with the wheel completely, which makes the actuation unit be a leg while walking.

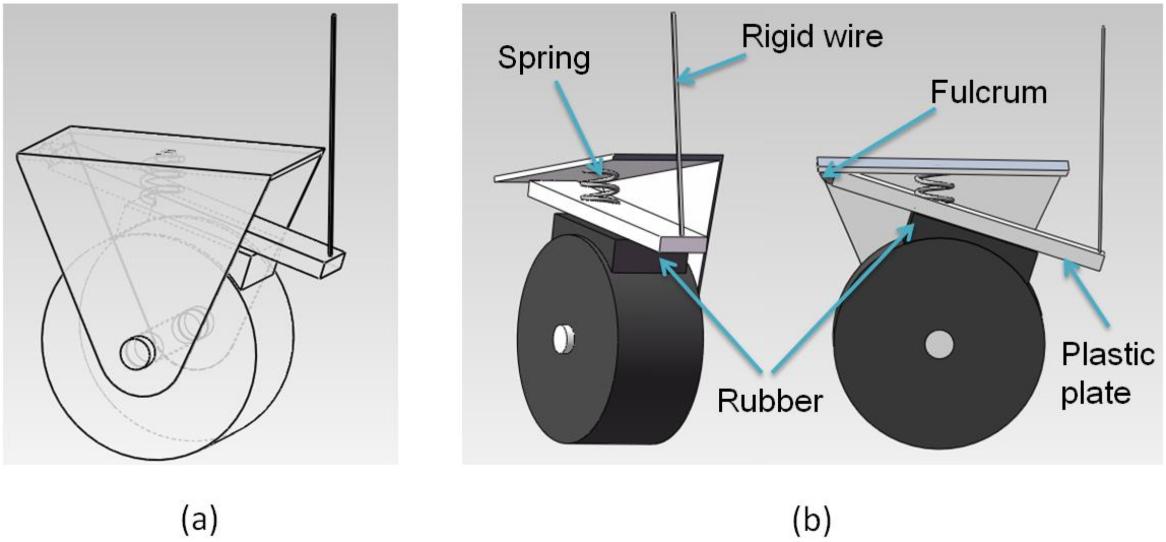

Figure 3- 9 Braking mechanism of the wheel: (a) overall structure and (b) cross-section diagram

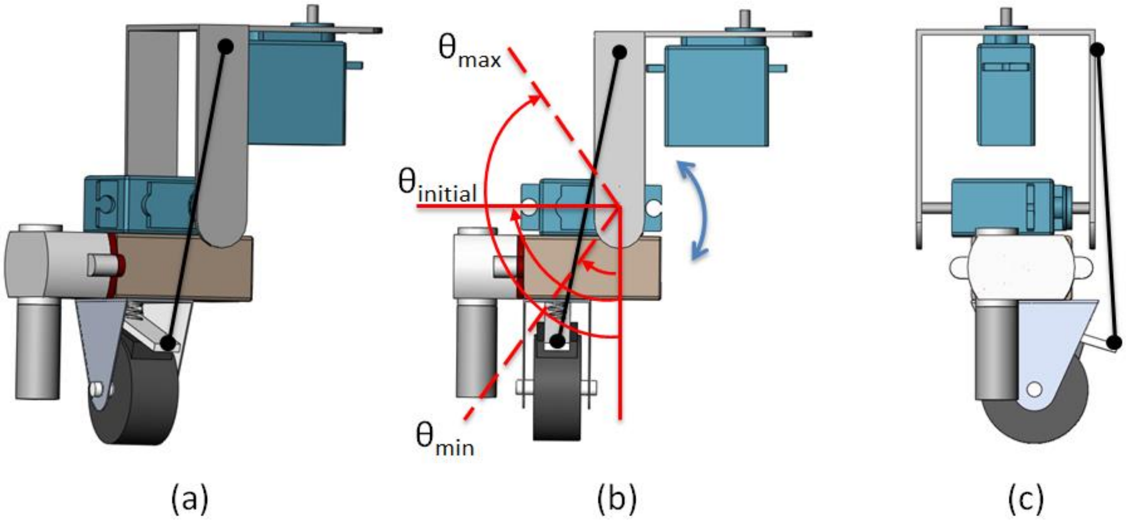

Figure 3- 10 Leg-wheel hybrid actuation system: (a) overall structure, (b) front view and (c) side view

In order to implement the walking and roller-skating motions for the robot in the new structure at the meantime, a transformation mechanism, which can switch the robot's locomotion between roller-skating and quadruped walking, is required. As rotating the vertical servo motor can tense and loose the rigid wire to change the state of wheel between free rolling and braking states, the proposed braking mechanism can also be used as a transformation mechanism to perform the mode switching between walking and roller-skating modes.

The rotational angle of the vertical motor is in a range of θ_{min} to θ_{max} while walking and roller-skating. The initial angle $\theta_{initial}$ shown in Figure 3-10 (b) indicates the initial state of the robot's leg when roller-skating. The vertical servo motor in the initial state tenses the rigid wire just right to separate the rubber from the wheel, remaining the wheel in free rolling state. When the motor rotates anticlockwise from the initial position, the wire will be pulled tighter to loose brake as like in the initial state; when the motor rotates clockwise from the initial position, the wire will be released to apply brake.

We have mentioned that two front legs and one rear leg are in the initial state and the other rear leg implements the sliding and propulsion phases during roller-skating. In the initial state, wheels can roll freely without applying brake. In sliding phase, as the rotational angle of the motor is less than the initial angle, the wheel of active rear leg performs the free rolling motion. Additionally, in the propulsion phase, the wheel rotates around the axis of the vertical motor, which is perpendicular to the axle, to push off the ground to generate the driving force in two directions. In the propulsion phase, the robot will loose brake at first and then apply brake, which has no effect on the movement of the robot.

The rotational angle of the vertical motor in the initial state is 1 degree larger than $\theta_{initial}$ while walking motion. The rotational angle in walking mode is in a range of the walking initial angle to the maximum angle θ_{max}. During the walking motion, all the wheels are in braking state at any time.

3.2.4 Water-jet actuation system

From the images segmented by the level set equation, a skeletonization technique is applied to obtain the vessels centerlines. This process allows our simulator to efficiently perform collision detection and blood flow computation by supplying an abstract topological representation of the vascular network.

The robot is actuated by water-jet propellers when underwater [36]. By controlling the angles of the servomotors, the spray angle of the water-jet propellers can be varied to control the motion of the robot. A force analysis was carried out to assess the requirements of the servomotors on the actuator units. Figure 3-11 shows the force analysis for one actuator unit during horizontal motion, floating motion, and sinking motion. By changing the angle of the vertical motor, thrust can be realized in all directions. The torque of the motor can be calculated as follows:

$$\overrightarrow{M_1} = \overrightarrow{F_{w1}} \cdot s = \overrightarrow{F_{w2}} \cdot s = \overrightarrow{M_2} \tag{Eq. 2-13}$$

$$\overrightarrow{M_3} = \overrightarrow{F_{w3}} \cdot s \tag{Eq. 2-14}$$

where F_{w1}, F_{w2}, and $\mathrm{F_{w3}}$ are the thrusts generated by the water-jet propeller, M_1, M_2, and M_3 are the torque on the servomotor, and s is the moment arm of the vertical motor. Appropriate servomotors were chosen by considering the maximum required torque.

To achieve the dynamic model of water-jet propeller, we build a fluid model of water-jet propeller by reference to a previous method [22], [37], as shown in Figure 3-12. The shaft of the motor, on which four blades are fixed, is perpendicular to the nozzle. Due to the small diameter of the nozzle, we can ignore the velocity difference across the nozzle. So we consider the axis flow velocity V_a as a linear combination of incoming flow velocity V_i and the central flow velocity V_c. In Figure 3-12, Ω is the rotational velocity of motor shaft, V_f is velocity of ambient flow, V_i is velocity of incoming flow, V_o is velocity of outlet flow, θ is incoming angle of ambient flow and D is diameter of the nozzle. Finally, the axis flow velocity can be obtained:

$$V_a = k_1 V_i + k_2 V_c$$

$$V_i = V_f \cos\theta \tag{Eq. 2-15}$$

$$V_c = \frac{1}{2} D\Omega$$

Assuming that the flow is incompressible, according to the equation of continuity, we know that the volume of incoming flow must be equal to the outlet flow, as shown in (Eq. 2-16).

$$\rho_a V_a A_a = \rho_o V_o A_o \qquad \text{(Eq. 2-16)}$$

where: the fluid density ρ_a and ρ_o are equal to ρ, the cross-section of the nozzle A_a is equal to A_o.

Hence, we arrive at the following relationship:

$$V_a = V_o \qquad \text{(Eq. 2-17)}$$

The thrust of the water-jet propeller in two directions can be calculated as (Eq. 2-18) and (Eq. 2-19) respectively.

$$F_{w1} = F_{w2} = \rho A {V_a}^2 \qquad \text{(Eq. 2-18)}$$

$$F_{w3} = \rho A {V_c}^2 \qquad \text{(Eq. 2-19)}$$

By substituting (Eq. 2-15) in (Eq. 2-18) and (Eq. 2-19) respectively, the thrust generated by water-jet propeller can be computed as (Eq. 2-20) and (Eq. 2-21).

$$F_{w1} = F_{w2} = \frac{1}{4} \rho\pi D^2 ({k_1}^2 {V_i}^2 + k_1 k_2 \pi D V_i + \frac{1}{4} {k_2}^2 D^2 \Omega^2) \qquad \text{(Eq. 2-20)}$$

$$F_{w3} = \frac{1}{16} \rho\pi D^4 \Omega^2 \qquad \text{(Eq. 2-21)}$$

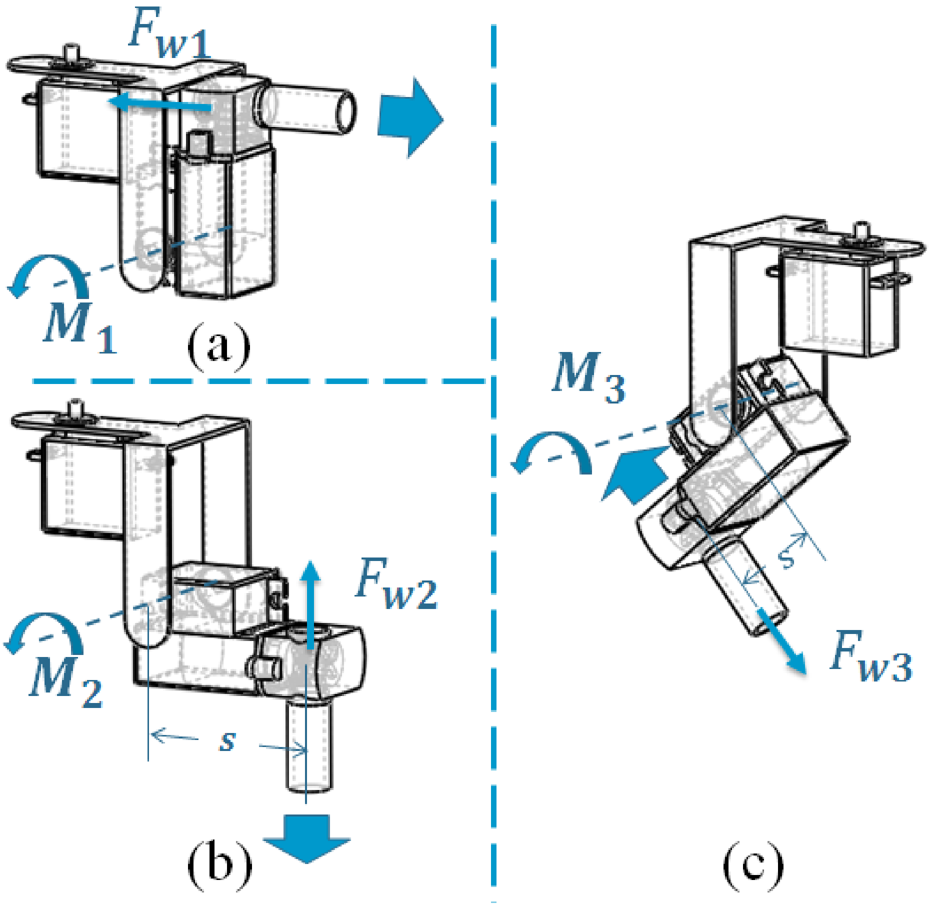

Figure 3- 11 Force analysis on one actuating unit during (a) horizontal motion, (b) floating motion, and (c) sinking motion. The blue arrows indicate the water-jet direction

3.2.5 Sensing mechanism

The amphibious robot can detect and avoid obstacles around it using proximity sensors. The spherical symmetry allows the robot to move in any direction by spinning prior to forward or backward motion. The sensors should therefore be placed symmetrically at the bottom of the upper hemisphere next to the transparent hull. Eight Sharp

GP2Y0A21YK infrared proximity sensors were used.

Because of the amphibious requirements, the robot must be able to determine whether it is on land or underwater. A Panasonic ADPW11 pressure sensor that can measure the air pressure and water pressure is located on the robot, fixed to the plastic circular plate.

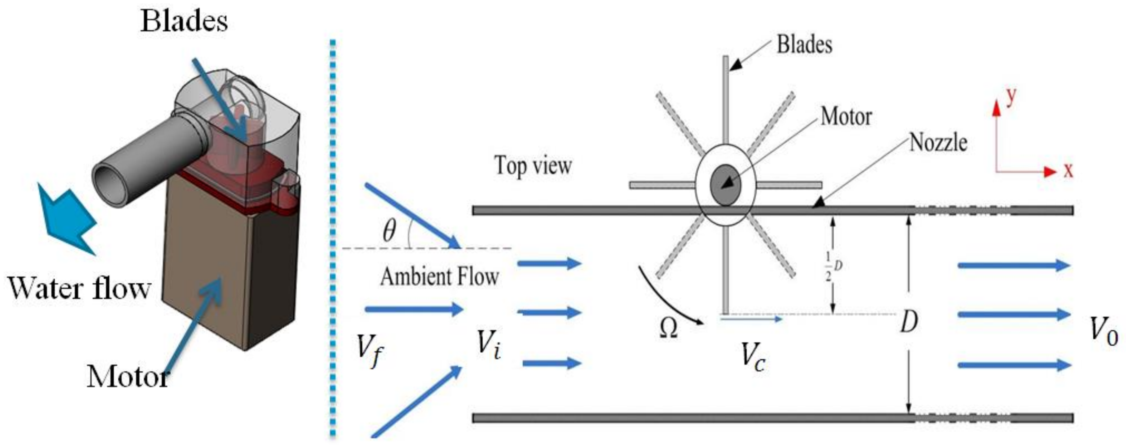

Figure 3- 12 Fluid model of water-jet propeller

3.3 Electrical system and power supply

The control center of the spherical robot is shown in Figure 3-13. It is based on an AVR ATMEGA2560 micro-controller, and uses ten PWM channels to control the eight servomotors to drive the robot and the two servomotors on the upper hemisphere to open and close the two quarter-spherical shells. Furthermore, eight input/output ports are used to control the four water-jet propellers. Using two data transmission ports, we utilized analog-to-digital conversion so that the microcontroller could receive and transmit data that control the infrared proximity sensors and pressure sensors, thereby realizing closed-loop control. The control system also included a radio frequency (RF) remote control module. Thus, a further four input/output ports were connected to the receiver module with four channels to control remotely the movement of the robot.

The power supply used three batteries: one 6TNH22A/8.4V battery to provide power to the AVR micro-controller, and two YBP216BE/7.4V batteries to provide power to the ten servomotors and the four water-jet propellers.

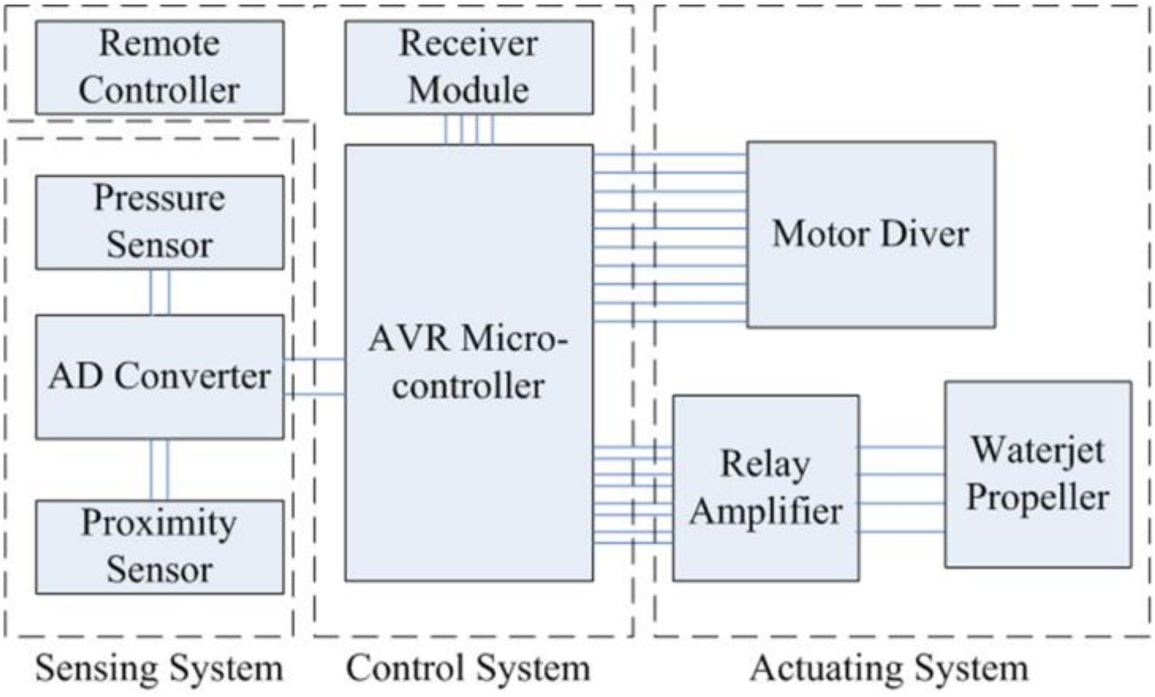

Figure 3- 13 Control system

3.4 Summary

An amphibious spherical robot with three actuating modes was proposed as the father robot of the father-son robotic system, including the quadruped walking mode, roller-skating mode and water-jet propeller mode. The father robot consists of a sealed upper hemispheroid, two quarter spherical shells, and a plastic circular plate. The robot is capable of motion on land, as well as underwater.

Chapter 4

Performance evaluation and improvements of the father robot

4.1 Prototype father robot

As shown in Figure 4-1, a prototype amphibious spherical robot was constructed with three actuating modes. The robot consisted of two main parts: the upper hemisphere and two transparent quarter-spherical shells. The actuating system and the plate for the microrobots were located in the lower hemisphere. Four passive wheels were installed on four legs of the robot. And each leg has one passive and two active degrees of freedom. Moreover, a braking mechanism is added to the wheel on each leg to apply brake when required. We chose to use HS-5086WP servomotors, supplied by the Hitec Company, which are waterproof. The water-jet propellers were not waterproof, and were supplied by Raboesch Company. The total mass of the robot is 2.3 kg.

The basic structure of control system has been introduced in Chapter 3. Figure 4-2 shows the prototype control system with a compact structure. AVR ATmega2560 was used as the central controller. And Omron G6K-2P relays were used to build the amplifier circuit for water-jet motors. A 16ch AD convertor made by Asakusa company was used to support sensors. And a remote controller kit was used to realize remote control during experiments. And a gyroscope sensor was used to keep the moving direction stable.

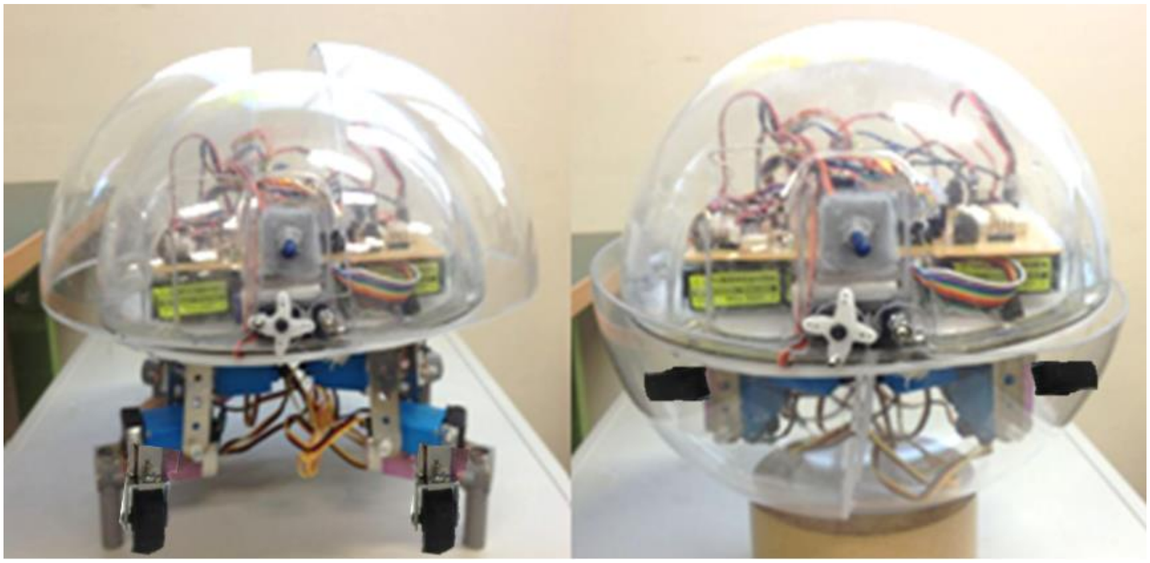

Figure 4- 1 Prototype amphibious robot in (a) quadruped walking and roller-skating modes, and (b) water-jet propulsion mode

4.2 Sliding/walking experiments on a smooth flat surface

In order to evaluate the performance of the robot while roller-skating and walking, both sliding and walking experiments on a smooth flat surface were conducted. With roller-skating gait, the robot used the friction force as the driving force to move along a wave trajectory, as shown in Figure 4-3. Although the rear legs cannot provide propulsion when sliding motion stops, the robot can move forward with lower friction between wheel and ground due to the inertia effect. With braking mechanisms, four brake pads are separately controlled to be squeezed against each wheel to reduce the speed of the robot and finally stop the robot. The experimental results of roller-skating motion at different control frequencies are shown in Figure 4-4. The curve marked in red shows that the roller-skating velocity initially increased as a function of control frequency, and then decreased. At high frequencies, as the slip between the wheel and the ground becomes serious as a function of the frequency, the sliding velocity decreases. And a maximum roller-skating velocity of 37.8 cm/s was achieved.

With the transformation mechanism, the robot can realize walking and rotating motions with walking gait. To evaluate the walking performance, we measured the walking velocity at different frequencies with walking gait. In Figure 4-4, the curve marked in green indicates the walking velocity. From the results, as the frequency increased, the walking velocity increased at first, and then decreased to zero. The velocity of the robot is related to the step size and frequency. We achieved a maximum walking velocity of 22 cm/s. At relatively low frequencies, the walking and roller-skating velocities of the robot were approximately equal. It is obvious that at relatively high frequencies the sliding motion shows better performance than the walking motion. Compared to walking motion, sliding motion is not affected by the response time of the servo motor, which had a big influence on walking motion at relatively high frequencies.

Besides, rotating experiments were conducted to evaluate the performance of rotating motion with rotating gait. As shown in Figure 4-5, the green curve indicates the results of rotating velocity at different frequencies. The rotating velocity has the same rule change with the walking velocity as a function of frequency with walking gait. As we mentioned in Chapter 3, at low frequencies, the step size increased as a function of the frequency of the gait cycle, and then decreased towards zero at high frequencies. And we achieved a maximum rotating velocity of 66.7 °/s.

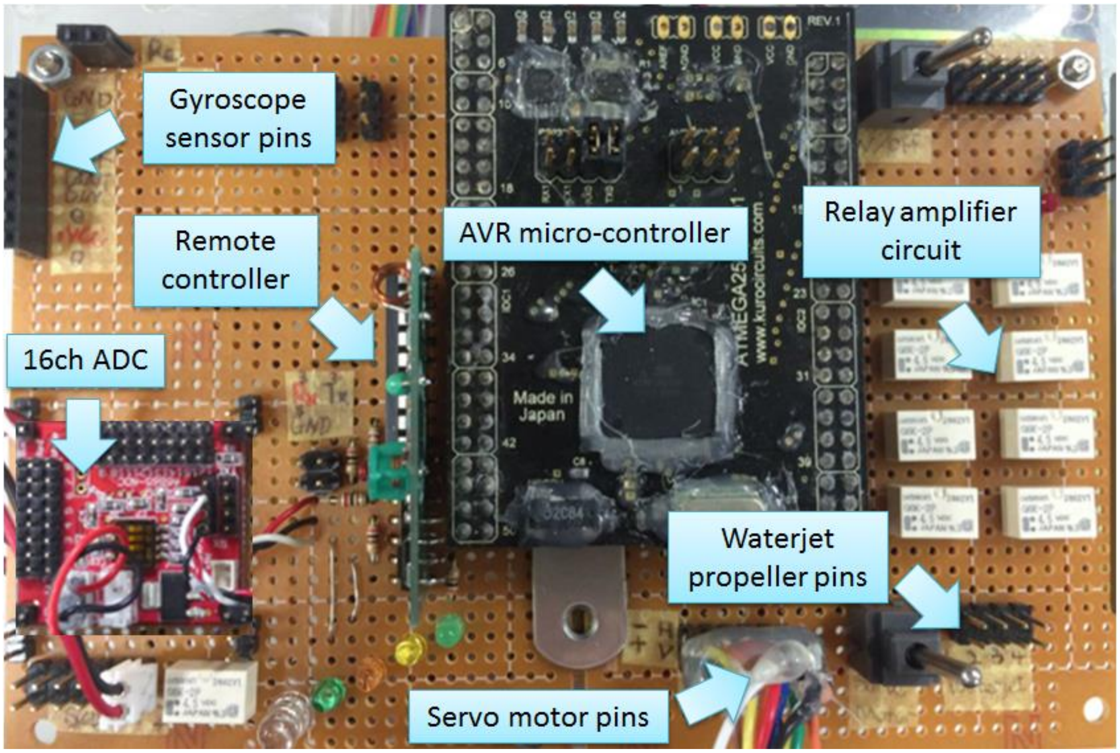

Figure 4- 2 Prototype control board

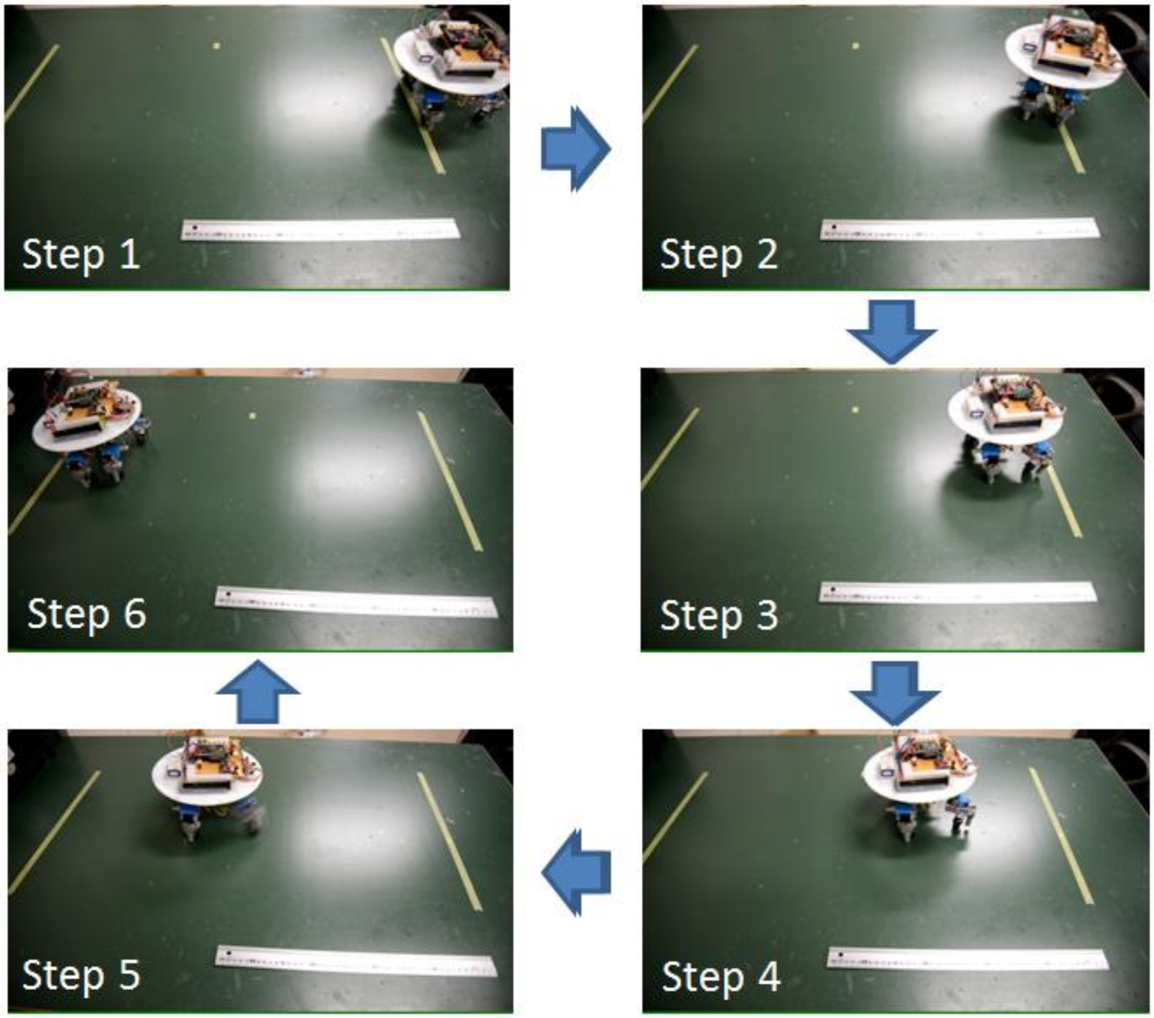

Figure 4- 3 Sliding experiments with roller-skating gait

4.3 Sliding/Walking Experiments on a Slope

To evaluate the slope performance of the robot when walking and sliding, walking and roller-skating experiments were carried out down a slope. On a slope, the component force of gravity of the robot provides part of the driving force, which causes the robot to achieve a relatively high velocity. A crucial aspect of moving down a slope is to maintain balance, which means that the robot's center of gravity must remain inside a polygon formed by the supporting legs. Since the two front legs are in the initial state all the time during sliding, sliding motion will be stable than walking motion.

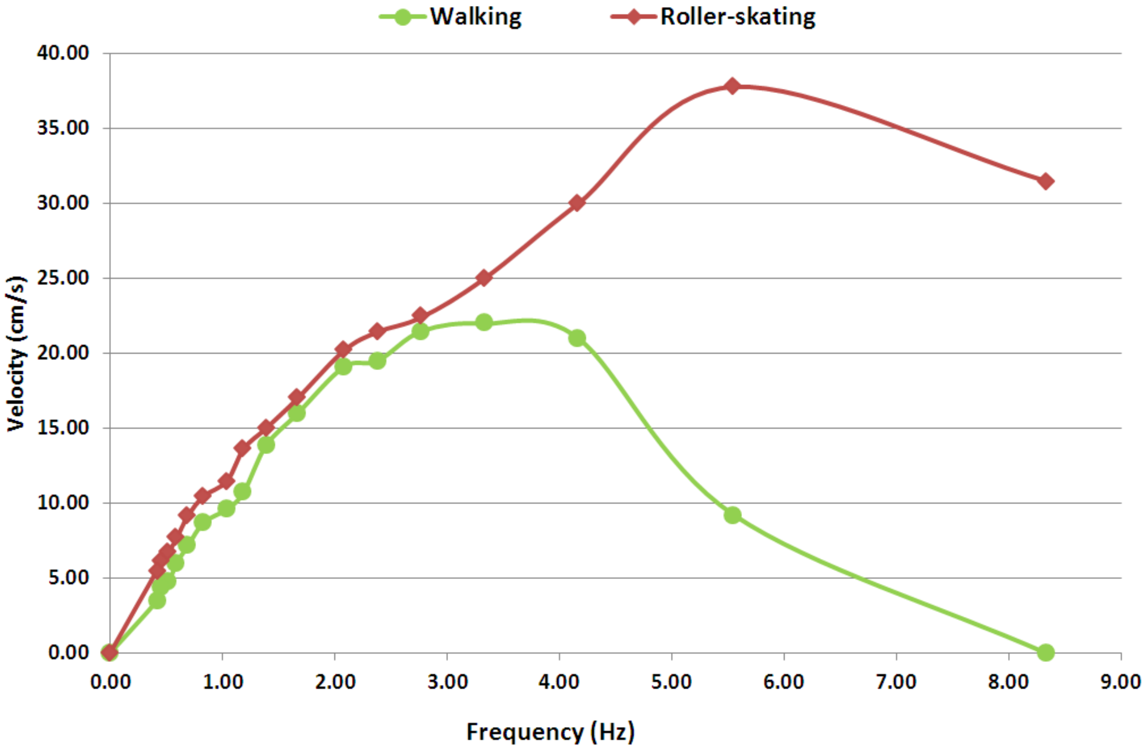

Figure 4- 4 Experimental results of the robot in roller-skating and walking modes. The control frequency is the movement frequency of the driving leg. The red and blue lines correspond to roller-skating and walking motions respectively

Figure 4-6 shows the experimental results of the walking and sliding velocities down a slope at an inclination angle range of 0 º to 10 º. The curve marked in red shows that as the incline increased, the roller-skating velocity of the robot increased; while the curve marked in green shows that the walking velocity initially increased as a function of incline, and after the inclination angle is over 7 ° the robot cannot keep balance on the incline. We achieved a maximum roller-skating velocity of 62.1 cm/s. Roller-skating gait showed a better performance than walking gait down a slope, allowing the robot to move downhill an inclination of 10 °.

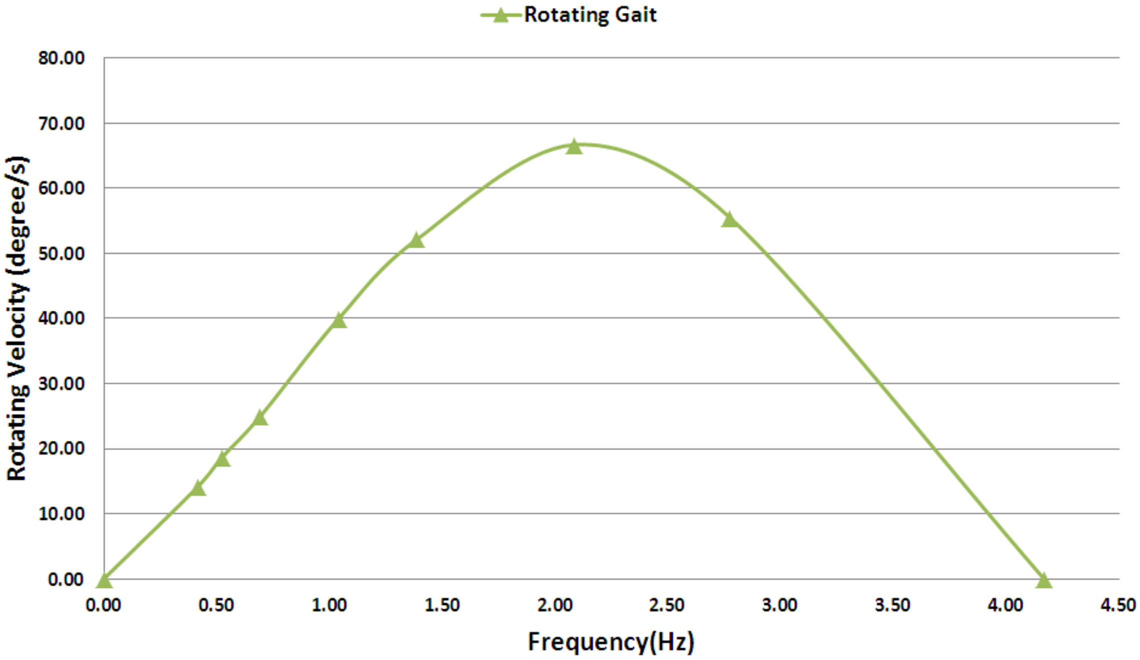

Figure 4- 5 Experimental results of rotating velocity of the robot with rotating gait

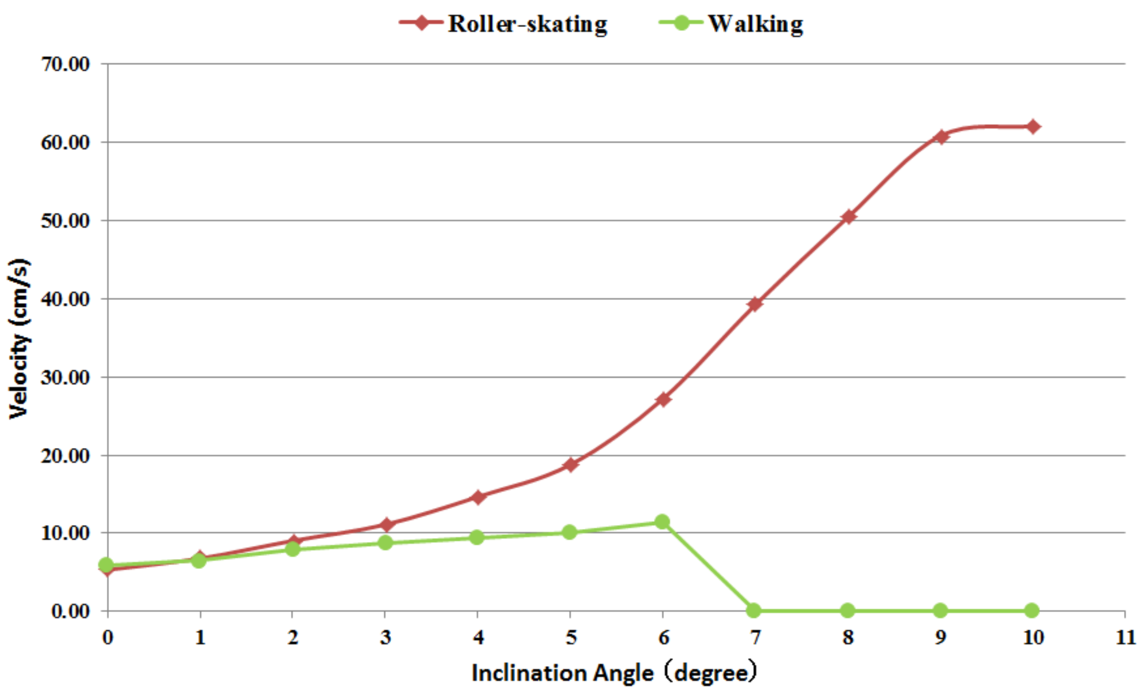

Figure 4- 6 Experimental results of the robot in roller-skating and walking modes down a slope with different inclination angles

4.4 Closed-loop control of the direction of movement

4.4.1 Design of the closed-loop control system

Gait stability is a principal element to evaluate the motion of a mobile robot, because precise position control is necessary for operations and all the tasks both on land and underwater need a stable working platform. Attitude information of a robot contains three angles, including pitch, roll and yaw angles. According to the results of the previous gait stability experiments, the vibration of the robot’s body in pitch and roll directions during walking and rotation existed and could not be avoided, but it had less influence on the direction of movement of the robot. However, vibration in yaw direction makes a great influence on the robot’s locomotion. For the improvement of the walking stability of the wheeled robot in longitudinal direction, a closed-loop control method is designed to control the stability of moving direction during the walking motion.

For the previous robot, because of the torus contact surface between the robot legs and ground, it is easy for the robot legs to stumble over the bulges on the ground, which causes the moving direction unstable. However, for the revised robot with four wheels, the wheels support the robot on the ground instead of the nozzles with the advantages of big contact surface and not easy to stumble. Compared to the previous robot, the revised one shows a better performance on the stability of longitudinal motion. But the robot still has vibration in yaw direction due to the complex ground environments. Therefore, the yaw angle, an attitude angle, must be obtained to realize a closed-loop control on the movement stability. A gyroscope sensor, ADIS16265, was carried on the robot to measure the yaw angle for the control of moving direction. During the walking motion, when a yaw angle measured by ADIS16265 is over 10 ^{o}, the robot is set to change its motion from walking to rotation to make its body face forward. According to this setting, the rotational angle of one gait cycle should be over 10 ^{o} and as close to 10 ° as possible. Consequently, an appropriate control frequency with the walking gait is required to achieve a rotational angle as close to 10 ° as possible during one gait cycle.

In order to achieve an appropriate rotational angle during one gait cycle, we did the calculation using the gained rotating velocities in Figure 4-5 to get the relationship between step angle and step frequency. The rotating velocity is related to the step angle and step frequency of the gait cycle, i.e.,

$$\omega = \theta * f \tag{Eq. 4-1}$$

where ω is the rotating velocity, θ is the step angle of one gait cycle, f is the control frequency of the gait cycle.

According to the equation (Eq. 4-1), we achieved the relationship between the step angle and step frequency. As shown in Figure 4-7, the green points imply the results of the step angle of one gait cycle as a function of control frequency. From the results, we can see that as the step frequency increases, step angle slightly increases at first, and then decreases to zero. Figure 4-7 shows the approximate curve and the equation of the step angle of the robot with the rotating gait. Considering the range of the yaw angle, a step rotational angle of 11 ° at a control frequency of 3.3 Hz is set for the robot.

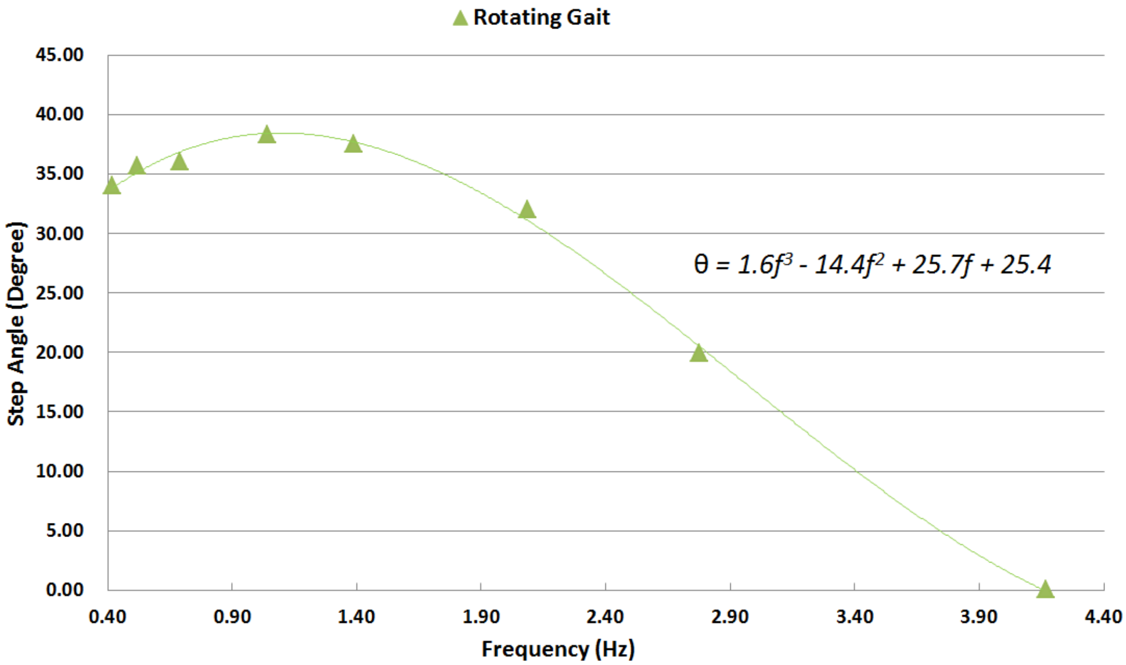

Figure 4- 7 Experimental results of the step angle of the robot with rotating gait

Figure 4-8 shows a flow chart of the control system of longitudinal motion. The gyroscope sensor is applied to measure the yaw angle of the robot. Depending on the degree of yaw angle, the robot implements the locomotion transformation from walking to rotation. When the degree of yaw angle is less than 10 °, the robot is controlled to move two steps forward; when the angle is over 10 °, the robot is controlled to spin clockwise or anticlockwise for getting back to the initial direction.

4.4.2 Performance evaluation of the gyroscope sensor

In order to control the direction of movement, a closed-loop control method is proposed with a gyroscope sensor equipped on the robot.

ADIS16265, a yaw rate gyroscope sensor, operated by a single supply in a range of 4.75 V to 5.25 V is used for the motion control of the robot. Four SPI signals of the gyroscope sensor are used to produce data and make it available to a processor.

By calculating the relative error of the data of rotational angle collected from ADIS16265 by PC, we can achieve the accuracy of the sensor. AVR microcontroller communicates with ADIS sensor by SPI (Serial Peripheral Interface) and transmits the ADIS16265 data to PC over UART (Universa Asynchronous Receiver/Transmitter). We use COMDEBUG on the PC to receive data from ADIS sensor. Serial debug terminal settings are as following: 9600 baud rate, 8 data bit, one stop bit, no parity bit. We manually rotated the ADIS sensor by 90 ° clockwise and recorded the data from COMDEBUG at intervals of 10 °. The data at each angle was recorded after 20 seconds and the experiment at each angle was repeated 10 times to get the average value. Figure 4-9 shows the experimental values of the rotational angle of the sensor and the relative error in the measurements. According to the results in the histogram, we achieved a minimum relative error of 0.5 %. Although the relative error at a rotational angle of 10 ° is 13.6 %, which seems to be a little large, the angle error between experimental value and theoretical value is approximately 1 °. Therefore, the accuracy of the gyroscope sensor is high enough to implement the longitudinal motion control of the robot.

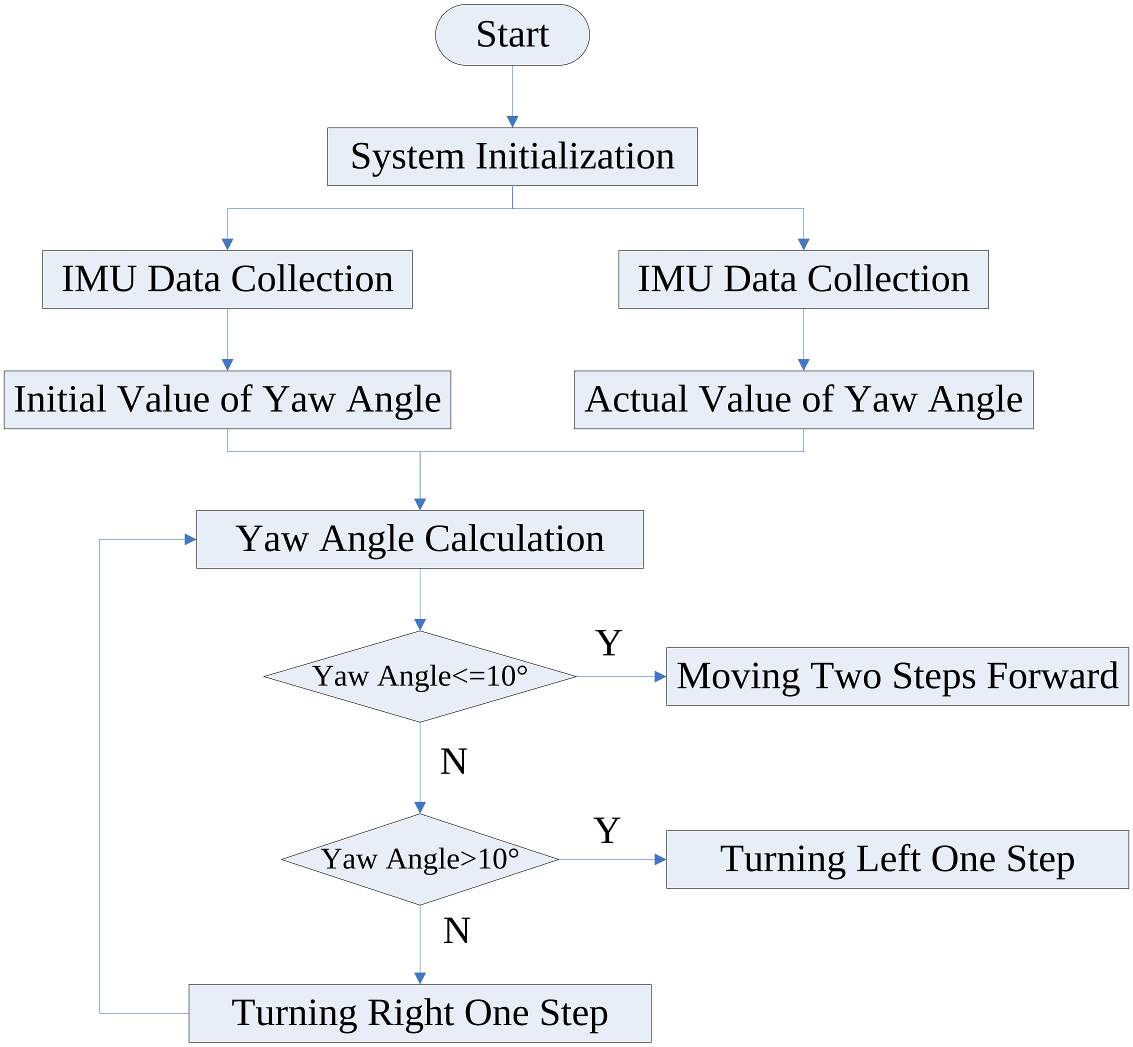

Figure 4- 8 Flow chart of the longitudinal motion control system

4.4.3 Closed-loop control experiments

In order to improve the walking stability of the wheeled robot with the walking gait in longitudinal direction, the ADIS sensor is carried on the robot to measure the yaw angle. Additionally, two kinds of closed-loop control experiments are conducted to evaluate the performance of the control of the direction of movement for the robot based on the closed-loop control system. One kind of the experiments is that the robot moves on the uneven ground. During the walking motion, a yaw angle happens to the robot due to the different step loss of the four legs. The other kind of the experiments is that the robot moves on the even ground and an external force is applied on the robot to cause a deviation in the moving direction. Using the closed-loop control system, the moving direction is offset by the rotating motion.

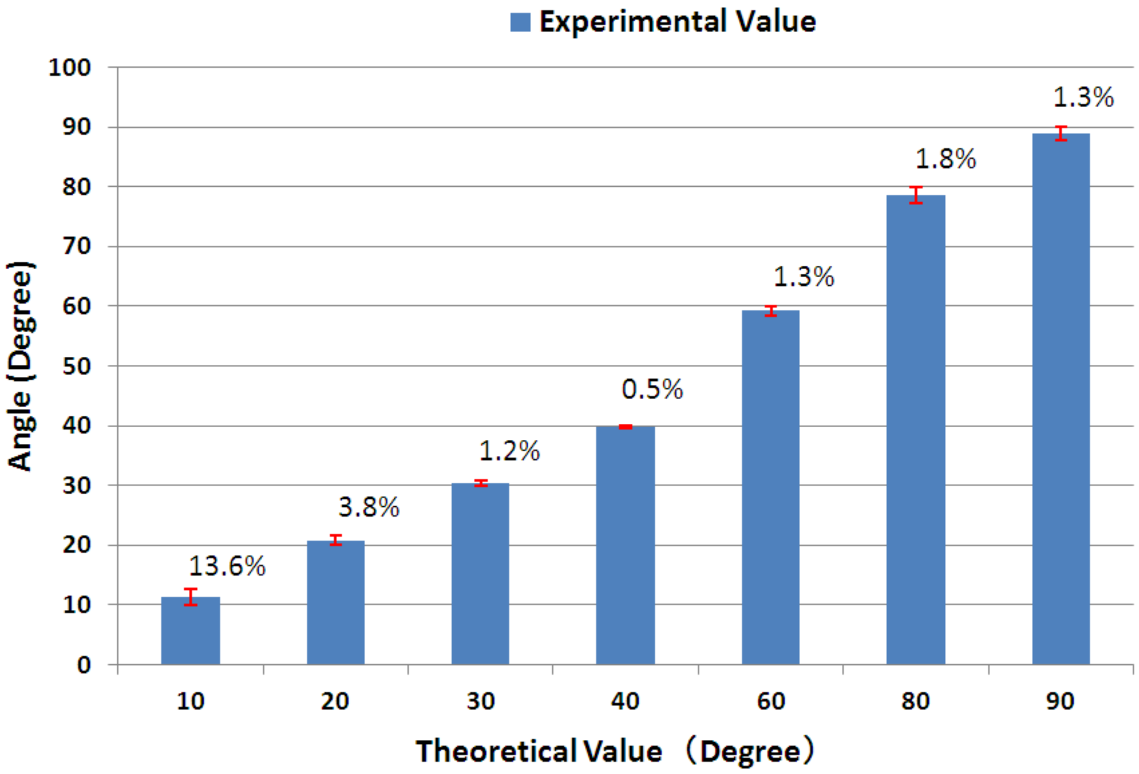

Figure 4- 9 Experimental results of the robot in roller-skating and walking modes down a slope with different inclination angles

A walking experiment of the robot acted upon by an external force was done for evaluating the ability of the control in longitudinal direction, as shown in Figure 4-10. An ADIS gyroscope sensor was employed to measure the change of yaw angle. Through the measurement of the yaw angle in real time, the robot can keep its moving direction by the rotating motion after an external force is applied on it. From the experimental results, the robot performs well in the directional control.

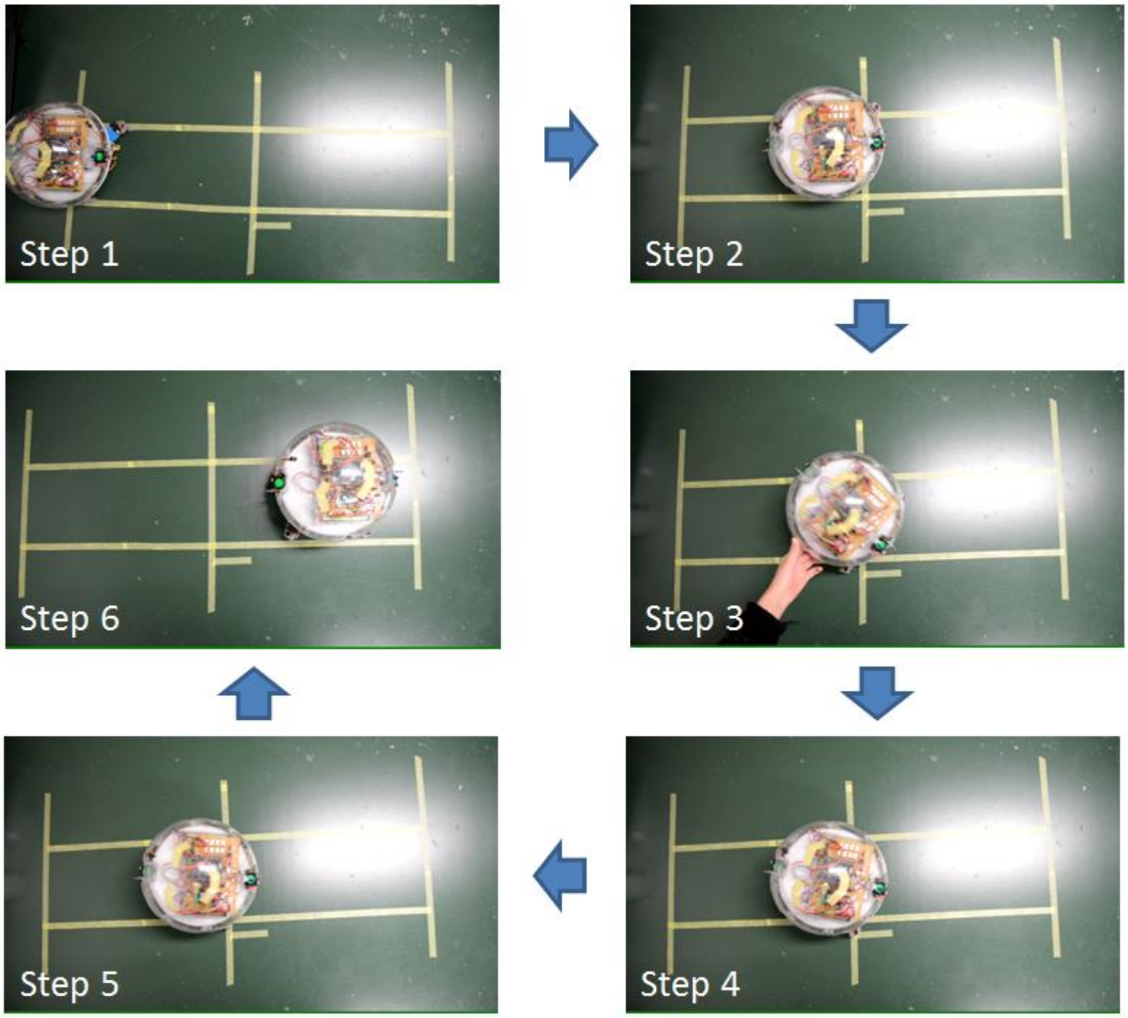

Figure 4- 10 Closed-loop control experiments of the moving direction of the robot acted upon by an external force

4.5 Underwater experiments and analysis

4.5.1 Underwater thrust experiments

To implement a controllable thrust of the water-jet propeller, the rotational velocity of the motor was controlled to change in a range as the duty of PWM signals changed. According to (Eq. 2-20) and (Eq. 2-21), we know that the thrust is related to the rotational velocity which varies depending on the duty of PWM signals. For the purpose of the thrust control, experiments of thrust measurement of a single water-jet propeller were conducted to get the relationship between the duty of PWM signals and the thrust of the water-jet propeller. Additionally, experiments of horizontal thrust and vertical thrust measurement of the robot as a function of the duty were carried out. All experiments were repeated ten times at a set of control signals to achieve an average thrust.

The experimental setup, as shown in Figure 4-11, was designed to measure the thrust of the water-jet propeller according to leverage principle. The propeller can generate two kinds of thrust: thrust generated by the flow passing through the long nozzle (Situation 1) and the flow passing through the nozzle on the opposite direction (Situation 2). An electronic scale was used to measure the thrust. Assume that the length of two levers are a and b respectively, and the difference between the two readings displayed on the electronic scale is m. We calculated the thrust of the water-jet propeller according to the following:

$$F = \frac{mga}{b} \qquad \text{(Eq. 4-2)}$$

The results of the average thrust measurement of a water-jet propeller in two situations are shown in Figure 4-12. The thrust increases as the duty of PWM signals increases. From the results, the water-jet propeller in Situation 2 shows the better performance than Situation 1. A maximum thrust of 99.5 mN in Situation 1 and a maximum thrust of 125.8 mN in Situation 2 were achieved at a duty of 100%.

The experimental setup for measuring the horizontal thrust was designed by employing leverage principle, as shown in Figure 4-13. An electronic scale was used to measure the thrust generated by the water-jet propellers of the robot. Assume that the length of two levers are a and b respectively, and the difference between the two readings displayed on the electronic scale is m. The horizontal thrust can be calculated according to (Eq. 4-2).

There are two kinds of actuating modes while moving forward and backward. The first actuating mode of the robot is to use two actuating units opposite to the moving direction. The thrust (in Situation 1) generated by the flow passing through the long nozzle is the main thrust of the robot. For the second actuating mode, the robot is actuated by the remaining two actuating units. The thrust (in Situation 2) produced by the flow passing through the nozzle on the opposite direction is the assist thrust of the robot. In order to gain a larger thrust, four actuating units work at the same time to get both the main thrust and the assist thrust.

Figure 4-14 shows the results of the average horizontal thrust as a function of the duty. From the results of two graphs, the thrust increases in terms of the duty of PWM signals. A maximum main thrust of 120 mN and a maximum assist thrust of 60 mN, which is approximately half of the main thrust, were achieved. The big difference between ideal thrust and actual thrust is caused by the thrust loss. The assist thrust of the robot is relatively small, because that the two nozzles are deployed inside the robot, which causes part of the thrust to be offset by other components. At a duty of 100%, a maximum actual thrust of 180 mN was achieved with all the actuating units working.

Figure 4-15 shows the designed experimental setup for measuring the vertical thrust based on leverage principle. The electronic scale was also used to measure the thrust of the robot. Assume that the length of two levers are a and b respectively, and the difference between the two readings displayed on the electronic scale is m. The upward thrust and downward thrust of the robot can be computed by (Eq. 4-2).

In the experiments of vertical thrust measurement, four actuating units were actuated to develop vertical thrust, including upward thrust for floating upward and downward thrust for sinking down. Compared with horizontal movement, actuating four water-jet propellers together can gain a relatively large actuating force while vertical movement.

Figure 4-16 shows the results of the average vertical thrust as a function of the duty. From the results of two graphs, the thrust increases in terms of the duty of PWM signals, and the actual thrust is close to the ideal thrust due to less thrust loss. A maximum upward thrust of 333.2 mN and a maximum downward thrust of 362.6 mN were achieved. The direction of the buoyancy of the robot leads to the difference between the two kinds of thrust. The experiments of both horizontal thrust measurement and vertical thrust measurement proved that PWM control method is effective for underwater thrust control.

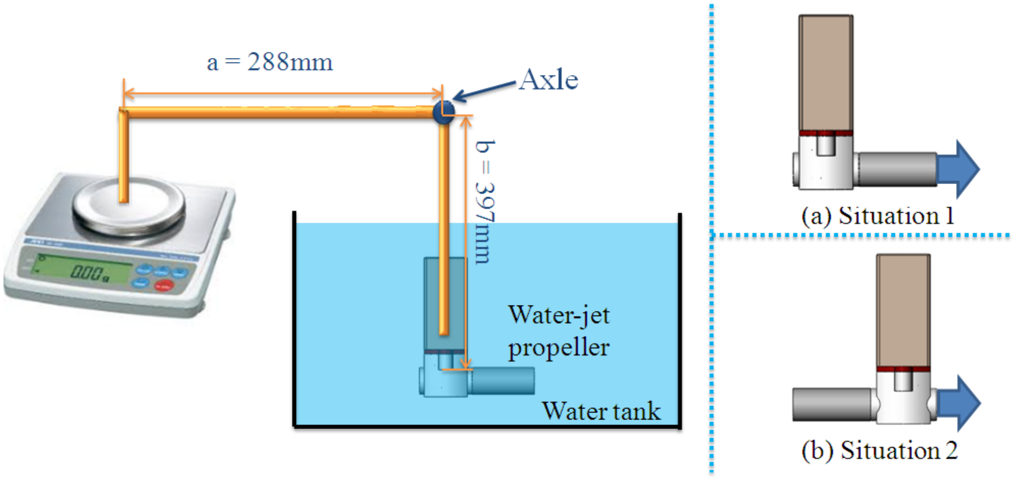

Figure 4- 11 Experimental setup for thrust measurement of a water-jet propeller in two situations. Blue arrows indicate the thrust direction

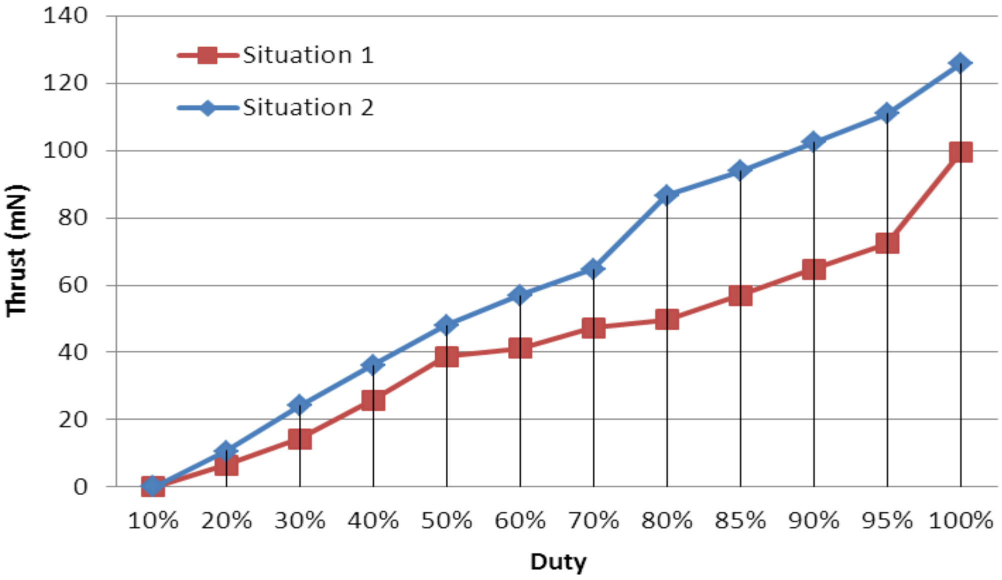

Figure 4- 12 Results of the average thrust of a water-jet propeller

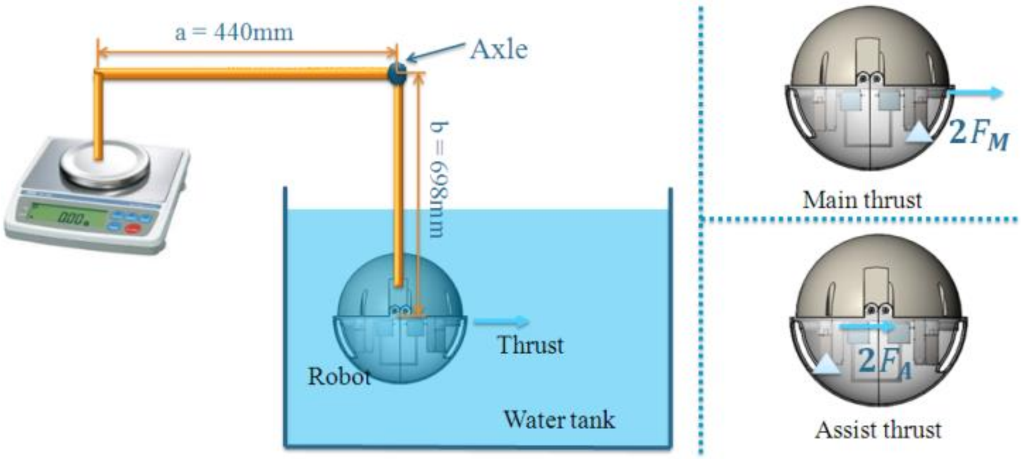

Figure 4- 13 Experimental setup for horizontal thrust measurement. Blue arrows indicate the thrust direction. Blue triangles indicate applied actuating units

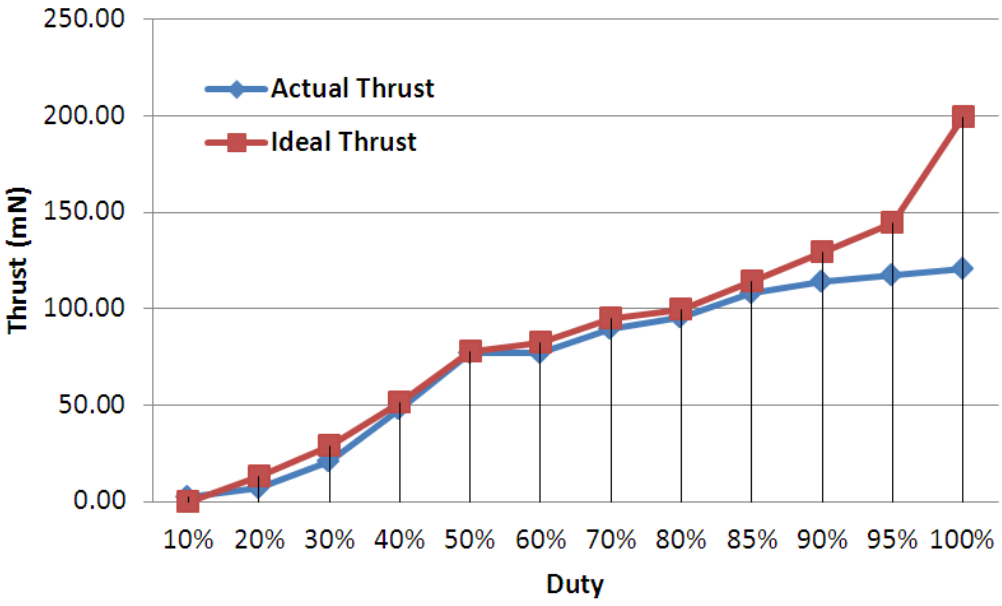

(a) Main thrust

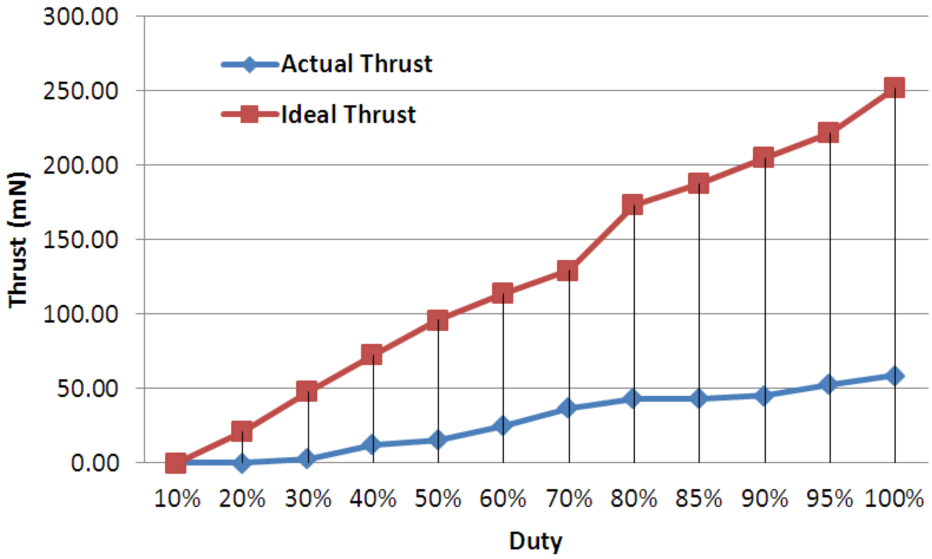

(b) Assist thrust

Figure 4- 14 Results of average horizontal thrust

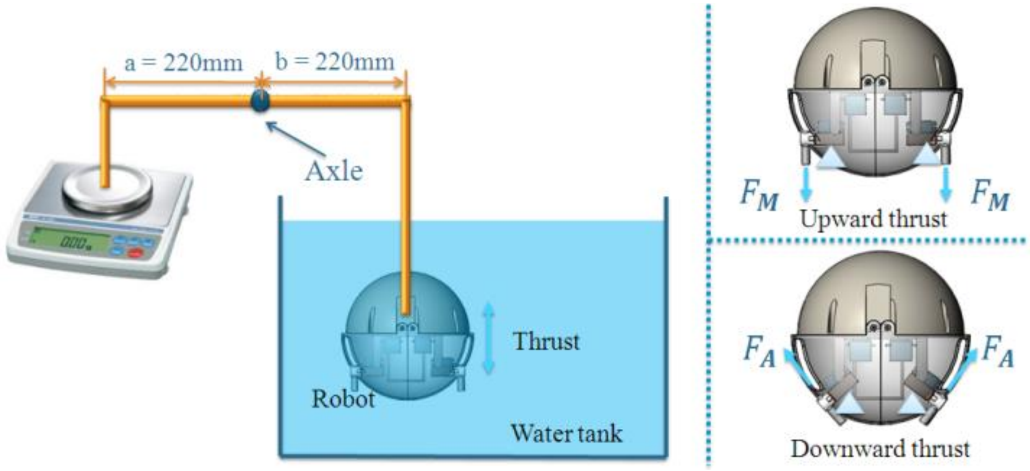

Figure 4- 15 Experimental setup for vertical thrust measurement. Blue arrows indicate the thrust direction. Blue triangles indicate the applied actuating units

4.5.2 Underwater velocity experiments

There are two states for the amphibious robot while underwater, which are the semi-submerged state and submerged state. The semi-submerged state is a state that all necessary loadings are equipped and no additional weight is added on the robot. And the submerged state is a state that additional weight is added on the robot to keep it suspend in water. In the semi-submerged state, the robot can float on water with approximately one-third of the body over the water surface.

The underwater experiments of the robot in the semi-submerged state were carried out to evaluate the underwater velocity performance of the robot. All experiments were repeated ten times at a set of control signals to achieve an average velocity. With the advantage of symmetry, the spherical robot shows the same performance while moving forward and backward or rotating clockwise and anticlockwise. Thus, the robot was programmed to move forward for 1m and then rotate 360° in a pool. The displacement distance and the rotation angle were measured by a ruler and a protractor respectively. By using the timer to measure the movement time, the average velocity of the robot was calculated. In order to make an overall analysis of the robot, the experiments of surge motion of the robot actuated by two main actuating units and four actuating units were conducted respectively.

Figure 4-17 shows the experimental results of the robot driven by different actuating units. The surge velocity increased smoothly as the duty of PWM signals increased. The blue line in the graph shows the surge velocities of robot as a function of the duty of PWM signals under the control of two main water-jet propellers. And the red line shows the velocities of robot actuated by all the water-jet propellers, which can provide a maximum thrust combining of main thrust and assist thrust. From the results, we got a maximum surge velocity of 16.1 cm/s under the control of four water-jet propellers. The results also indicate that the velocity difference in the two kinds of actuating modes is relatively small. Under a maximum duty of PWM signals, the velocity difference was only 2.4 cm/s. However, the energy consumption of a four-propeller-driven robot was considerable. In order to realize a high efficiency of the robot, we chose the two-propeller-driven mode during the surge motion. So, we got a maximum velocity of 13.7 cm/s under such a mode.

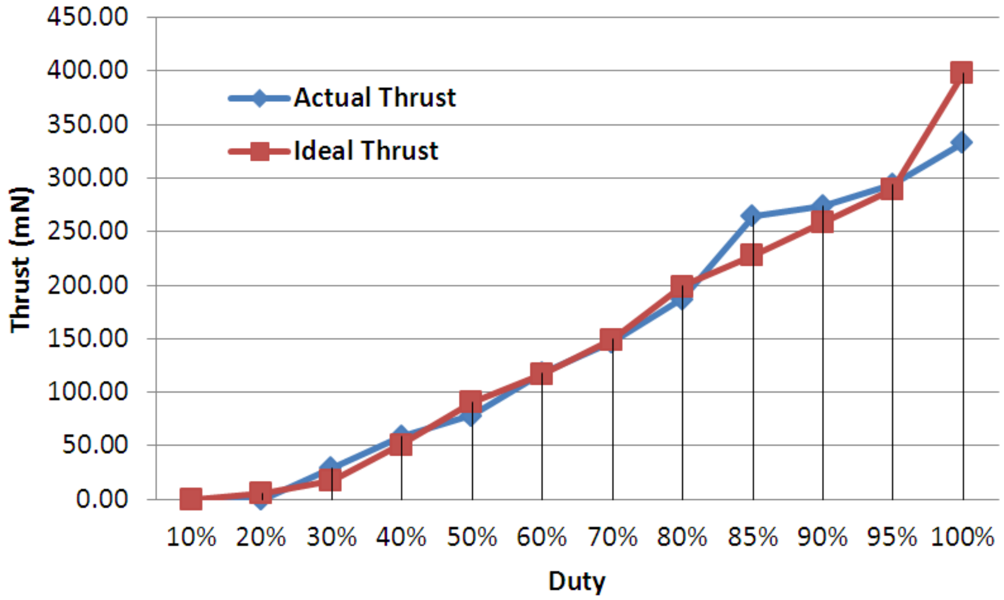

(a) Upward thrust

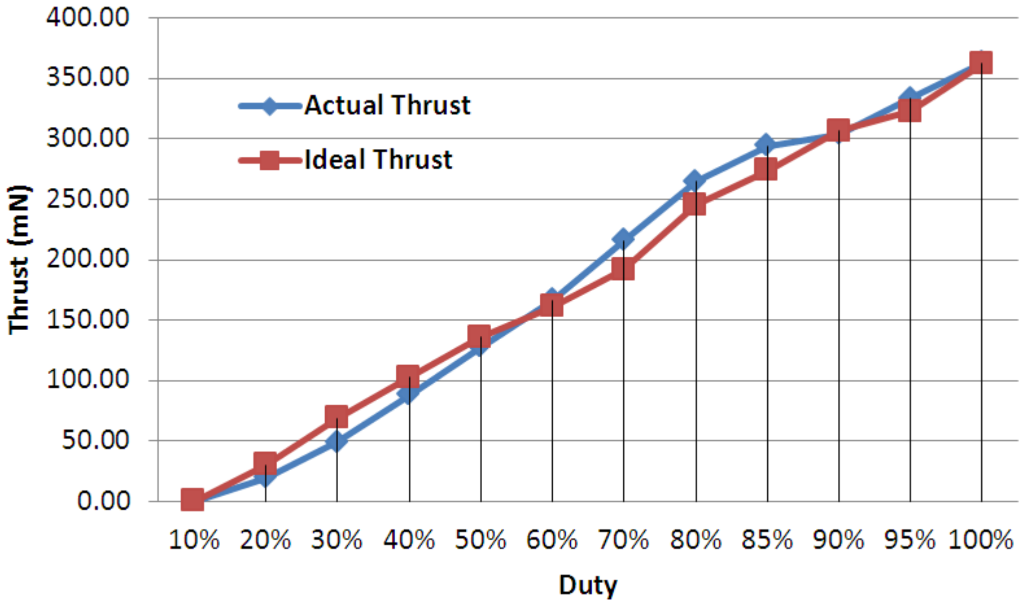

(b) Downward thrust

Figure 4- 16 Results of average vertical thrust

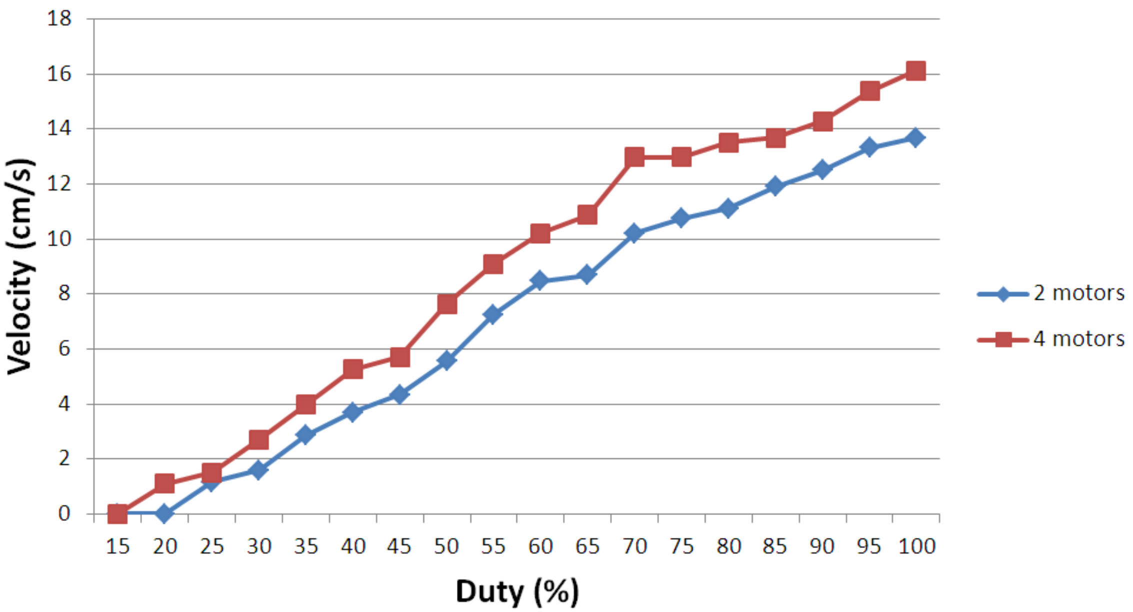

Figure 4- 17 Experimental results during underwater surge motion in the semi-submerged state

Figure 4-18 shows experimental results of the robot while rotation. As we know, the drag torque of a spherical robot is relatively small while rotation. Thus the robot can achieve a relatively high rotational velocity. Under a duty of 100%, we got a maximal rotational velocity of 64.3 °/s. With a high rotation performance, the robot is capable of flexible locomotion in the complicated environments.

The robot was also programmed to rise and sink for 1m in a pool. We measured the time and then calculated the average rising velocity and sinking velocity. From the experimental results, a maximum rising velocity of 8.4 cm/s and a sinking velocity of 8.4 cm/s were achieved.

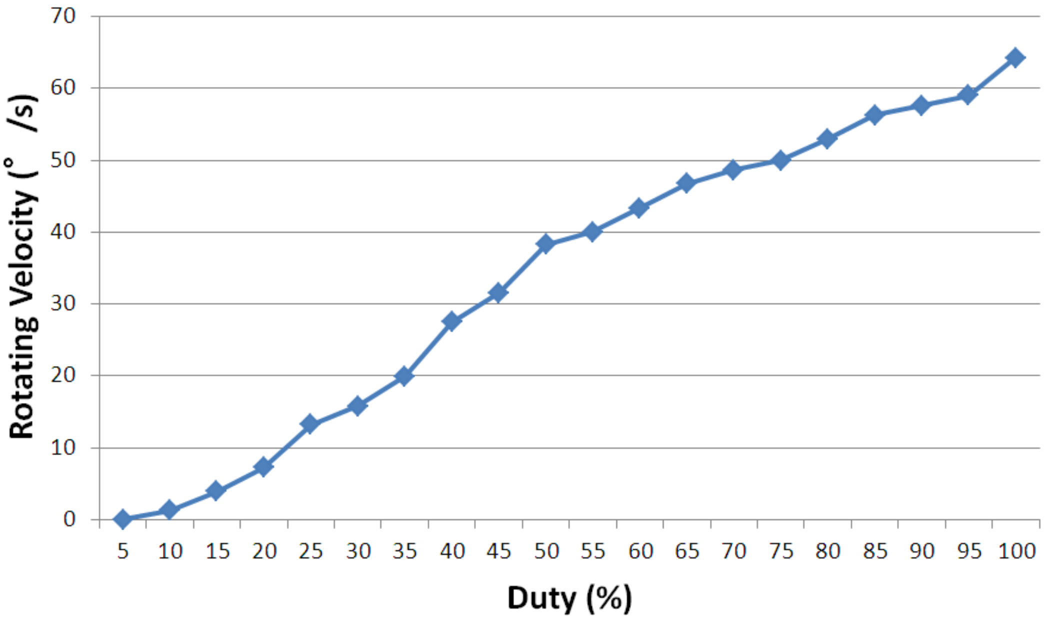

Figure 4- 18 Experimental results during underwater rotating motion in the semi-submerged state

4.6 Summary

The on-land and underwater performance of the amphibious robot was evaluated. A braking mechanism was proposed to realize the transformation of state of each passive wheel between free rolling and braking states by controlling the vertical servo motor to compress and release the spring. The braking mechanism can be used as a transformation mechanism to apply a walking gait to the wheeled robot to implement walking motion meantime. Hence, the experiments on smooth flat terrains and down a slope were described to evaluate the performance of roller-skating motion. Additionally, plenty of walking experiments of the robot with walking gait are conducted.

At low frequencies, the sliding velocity and walking velocity on the flat terrain were roughly equal. A maximum walking velocity of 22 cm/s was achieved. At a control frequency of 5.56 Hz, we got a maximum roller-skating velocity of 37.8 cm/s. And the robot was able to move down a slope with an incline of 10 ° with roller-skating gait. Roller-skating gait showed a better performance than walking gait in terms of mobile velocity and energy efficiency, especially moving down a slope.

Since there is a different step loss for four legs during walking, the direction of movement of the robot is unstable. For the improvement of the walking stability of the wheeled robot in longitudinal direction, we proposed a closed-loop control method by carrying a gyroscope sensor to measure the yaw angle of the robot in real time. And we conducted plenty of walking experiments to evaluate a good performance of directional control.

Finally, underwater thrust and velocity experiments in the semi-submerged state were conducted to evaluate the underwater performance. Under a duty of 100%, a maximum thrust of 180 mN in horizontal direction, and a maximum upward thrust of 333.2 mN and a downward thrust of 362.6 mN in vertical direction were got. Furthermore, a maximum surge velocity of 16.1 cm/s and rotational velocity of 64.3 °/s were obtained, and a maximum rising velocity of 8.4 cm/s and a sinking velocity of 8.4 cm/s were achieved.

Chapter 5

Proposed insect-like cable son robot as the manipulator

5.1 ICPF actuators

Compared with other actuators, ICPF actuators are capable of the work in both air and water. As an innovative material, ICPF is made of an ionic polymer membrane Nafion 117 chemically plated with gold electrodes on both sides. Owing to the change of the chemical structure of ICPF, a bending deformation will occur when an external electric stimulus is applied across it.

In view of this phenomenon, ICPF can be used as an actuator. When voltage is applied across both electrodes of ICPF, it will bend towards the positive electrode. Consequently, we used Nafion 117 to process and fabricate the ICPF for our research. The most common shape of ICPF actuator is rectangle, which can generate a stable deflection and bending force [39].

ICPF actuators have the characteristics of soft and compact structure, quick response, and low drive voltage, low noise. What's more important is that ICPF is capable of driving in water. With these advantages, ICPF actuators are appropriate to drive the son robot for the father-son robot system. Due to its property of quick response, ICPF actuators are used as undulating and oscillating fins for fish-like microrobots [30], [40]. However, swimming motion actuated by undulating and oscillating fins cannot ensure a precise position control of the robot. Also a fish-like robot cannot use the fins to realize a backward motion. To design a legged robot as the son robot is required for underwater missions.

5.2 General design of son robot

Nature provides many perfect models for robots. And many researchers did research on the biomimetic robots. For the crayfish, it has eight legs and two claws. The crayfish can walk underwater and grasp objects with its two big claws. Thus, we design a son robot which is inspired by the crayfish. Figure 5-1 shows a crayfish in walking and grasping motions.

To design a son robot, we should consider several constraints including the finite size of the holder on the father robot and limited power supply provided by father robot. Hence, the son robot is designed with the characteristics of miniaturization, light weight, low power consumption and driven by smart actuators. An eight-legged crayfish-like underwater microrobot is proposed to be the son robot of the father-son robot system [44]. This microrobot is composed of a main body, ten ICPF actuators, eight of which are legs for driving the robot and others are hands which are used as a claw for grasping objects, and several wires connected to the father body for receiving the control signals and power supply. Four legs are used as the drivers to drive the robot to implement a two-DOF movement. And others are used as supporters to lift the robot up. Considering the size of the holder, the size of the body of the robot are determined to be 24 mm long, 24 mm wide and 3.5 mm high and the size of the ICPF actuators are all determined to be 17 mm long, 3 mm wide and 0.2 mm thick. Each ICPF actuator has one degree of freedom. The conceptual design of the microrobot is shown in Figure 5-2.

Two photodiodes, the light sensors, are mounted in front of the robot to implement the tracking motion, including tracking the target object and other microrobots, especially tracking the father robot. With the tracking mechanism, the microrobot is able to get back to the father robot. Besides, an infrared proximity sensor is mounted on the bottom of the robot. Set the sensor between the two hands to detect the target object for object recovery.

5.3 Mechanisms of movement

5.3.1 Walking and rotating mechanisms

The crayfish-like microrobot employs eight legs to implement walking and rotating motions. The microrobot can realize each step cycle of walking forward motion with the following four steps, as shown in Figure 5-3. First, four supporters bend downwards to lift the body of the robot up, and now the drivers are kept off the ground. Second, when the body is lifted by the supporters, the four drivers off the ground bend forward. Thirdly, the supporters bend upwards so that they do not connect with the ground, and now the drivers are on the ground to support the body. Finally, the four drivers bend backward to generate the friction to make the robot move forward. The drivers are adopted to drive the robot and the supporters are to reduce the resistance from the ground. The oscillating frequencies of drivers and supporters are set to the same value, and the phase of the supporters is set to a value lagging behind that of the drivers by 90°. When the drivers on different sides bend towards different directions, the microrobot can implement the rotating motion, as shown in Fig. 6. According to the above, a series of walking and rotating motions can be performed, including walking forward/backward, rotating clockwise/ counterclockwise.

Assuming that the tip displacement of ICPF actuator is equal to $d/2$, we can achieve an average speed by (Eq. 5-1).

$$v = d * f \qquad \text{(Eq. 5-1)}$$

where v is the average speed, d means the distance that the robot advances per step cycle and f is the control frequency.

(a) (b)

Figure 5- 1 The crayfish in (a) walking motion and (b) grasping motion

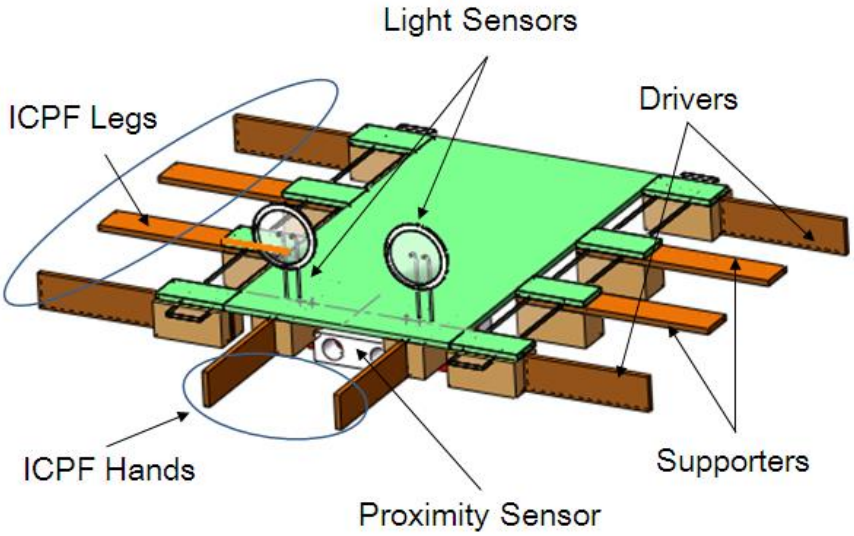

Figure 5- 2 Conceptual design of the eight-legged microrobot

5.3.2 Grasping mechanism

Two ICPF actuators as the hands of the microrobot are used to imitate a pair of the claws of a real crayfish. The mechanism of the grasping motion is shown in Figure 5-4. When the cathode of power supply is connected to the inner sides of the ICPF actuators, they bend outwards, which is in the open state. On the contrary, when the anode of power supply is connected to the inner sides of the ICPF actuators, they bend inwards, which is in the closed state. Two hands are fastened to the front of the microrobot with a distance of approximately 10 mm. The bending force generated by the two ICPF hands is determined by the driving voltage and the tip displacement. At a given voltage, with the deflection increasing, the bending force decreases. Consequently, the size of the target object determines the performance of the grasping motion.

5.4 Performance evaluations

5.4.1 ICPF actuators

Considering the compact structure of the son robot, the size of the ICPF actuators are all determined to be 17 mm long, 3 mm wide and 0.2 mm thick. As the performance of ICPF is depending on the effectiveness of fabrication processing, before mounting the ten ICPF actuators on the microrobot, we measured the tip deflection of a single ICPF actuator under different control frequencies for its performance evaluation. Figure 5-5 shows the experimental setup of deflection measurement for an ICPF actuator. The actuator is driven by a series of external control signals to bend in two directions recurrently. The tip deflection of the ICPF actuator is measured by a laser sensor, which can convert the distance to a voltage automatically. The laser sensor is connected to a personal computer (PC) with an analog-digital conversion (ADC). Through the relationship between the measured voltage and the distance, the tip displacement is calculated by the PC. The sample of ICPF actuator is 17 mm long, 3 mm wide and 0.2 mm thick.

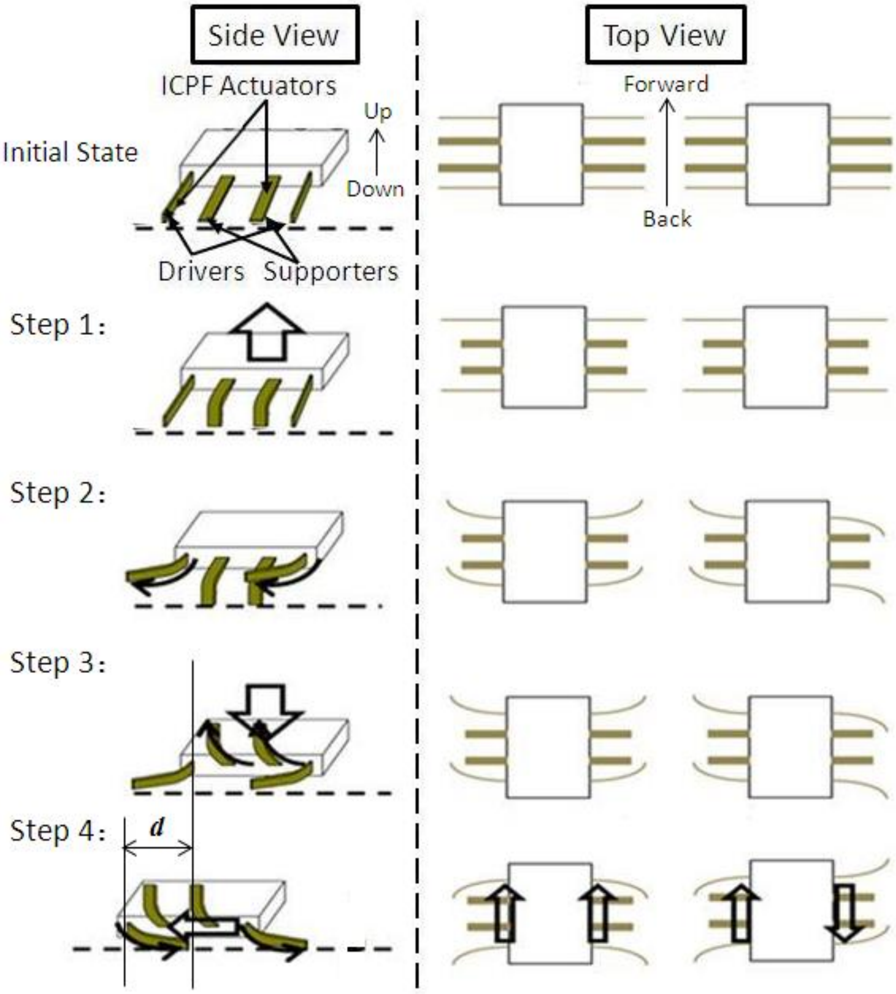

Figure 5- 3 One step cycle of moving forward and rotating clockwise motions (The marks ● indicate that the actuator contacts the ground)

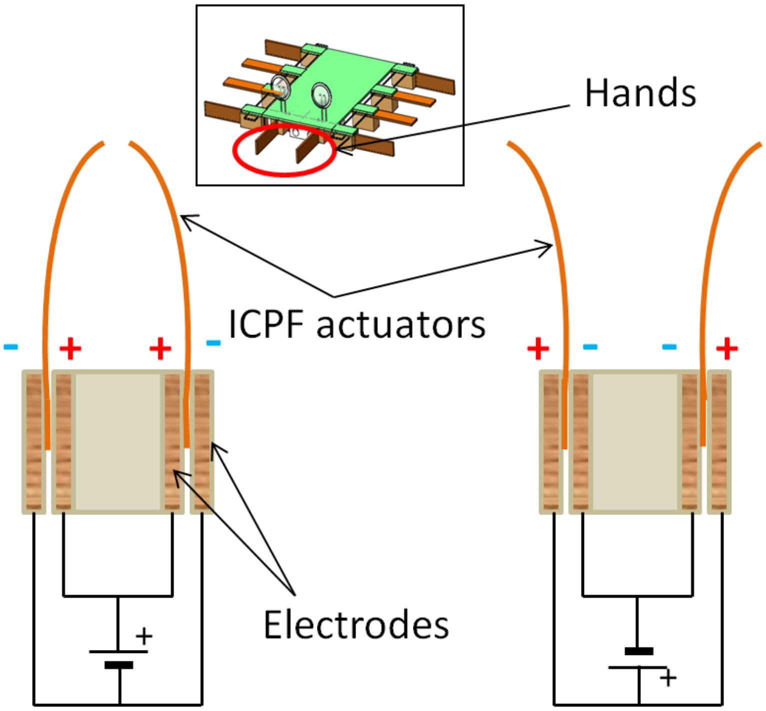

Figure 5- 4 Mechanism of the grasping motion

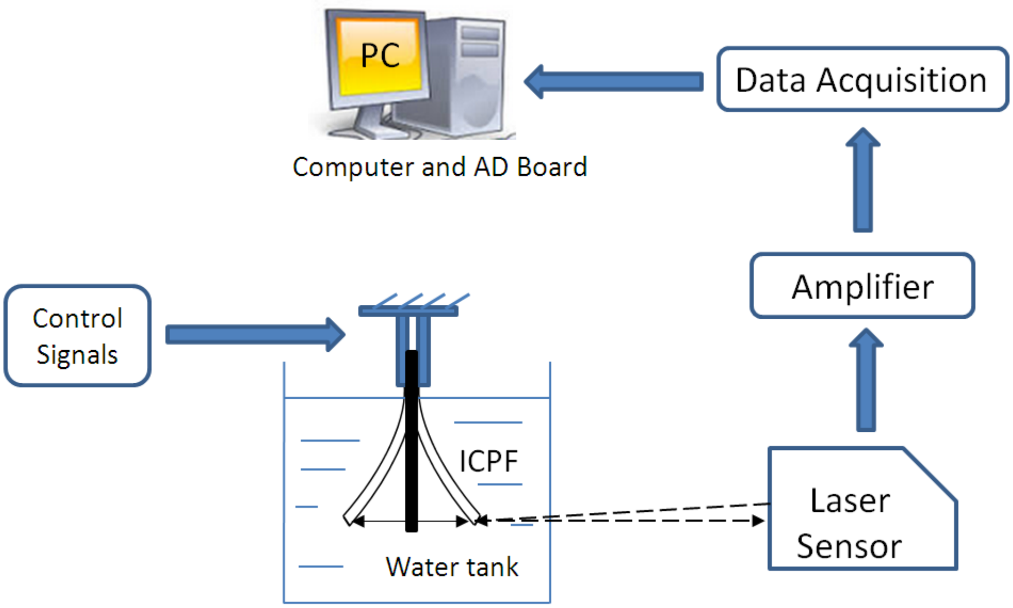

Figure 5- 5 The experimental setup of deflection measurement for an ICPF actuator

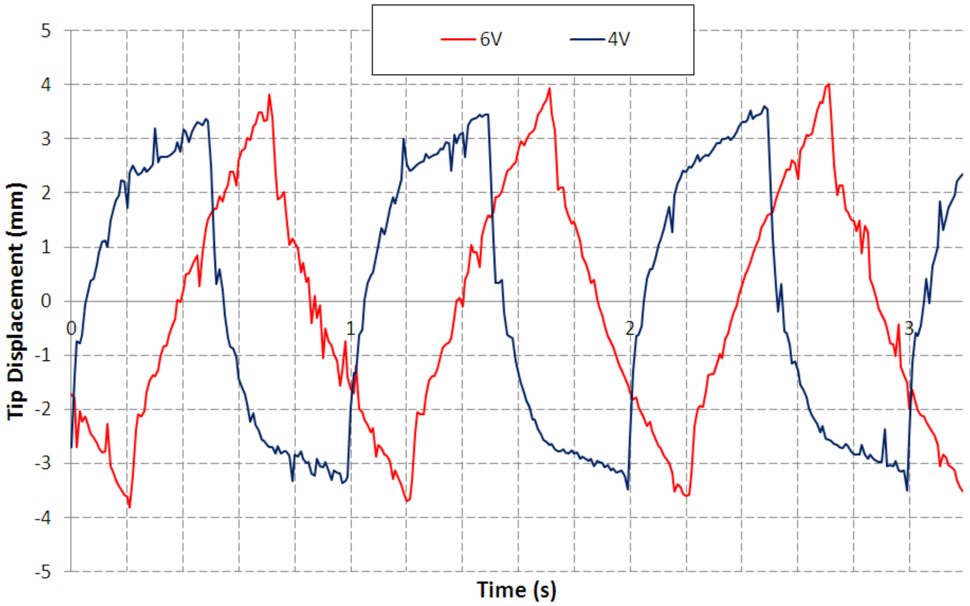

Figure 5- 6 Experimental results of deflection measurement for ICPF actuator with time

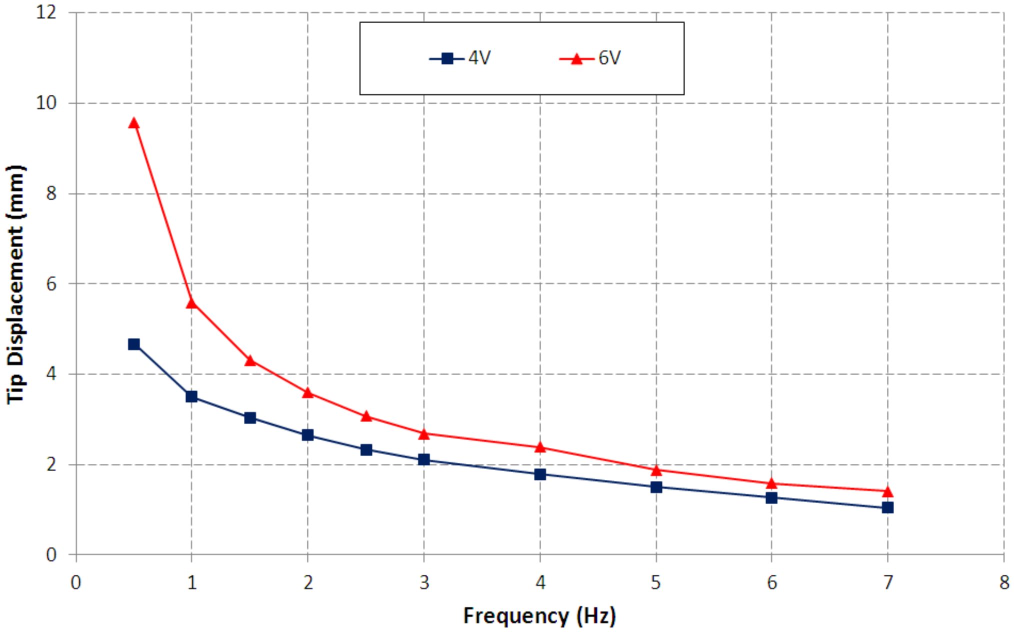

Figure 5- 7 Experimental results of deflection measurement for ICPF actuator under different control frequencies

During the experiment of the tip deflection measurement, two given voltages of 4 V and 6 V are applied to one end of an ICPF actuator respectively. These experiments are conducted under a control frequency of 1 Hz. By using the laser sensor, we measured the change of the tip displacement over time. The results of the change of the tip reflection are shown in Figure 5-6. Then, we changed the control frequency from 0.5Hz to 7Hz and measured the tip displacement under different frequencies. The experiments under each control signal are repeated 5 times to achieve an average tip displacement. The experimental results are shown in Figure 5-7. From the results, the tip displacement decreases as the control frequency increases. At relatively high voltages, the tip displacement decreases rapidly as a function of frequency. According to the Equation (Eq. 5-1), we know that with the frequency increasing, the average speed will increase first and then decrease to zero.

5.4.2 Proximity sensor

To implement the autonomous grasp for the microrobot, a proximity sensor is mounted in front of the robot right below the photodiodes. The sensor is set between the two hands to imitate the eye of the crayfish to detect the distance between the target object and the microrobot. The dimensions of the infrared proximity sensor used on the robot are 10 × 5 mm with a weight of around 0.7 g. With an angle measurement range from -30° to 30°, the proximity sensor can detect the total space between two ICPF hands.

We calibrated the proximity sensor for the distance measurement between the sensor and the target object. The calibration results indicate the relationship between the distance and the detected voltage. During the experiments, we changed the distance gradually from 60 mm to 25 mm and measured the output voltage increasing slowly from 0 V to 0.2 V. However when the distance is less than 25 mm, the output voltage increased rapidly. Depending on the measured voltages, the microrobot is able to know the remaining distance to the target object. According to the distance, the microrobot can control the ICPF hands to be open and closed to catch the object.

5.5 Prototype microrobot and experiments

5.5.1 Prototype microrobot

In order to implement the underwater missions, we proposed a crayfish-like underwater microrobot which is mounted on the father robot for object recovery and tracking. An eight-legged crayfish-inspired microrobot, as the son robot of the father-son robot system, is constructed, as shown in Figure 5-8. Eight ICPF actuators are employed to actuate the microrobot and two ICPF actuators in front of the robot are used to mimic the claw of the crayfish for grasping object. Each ICPF actuator is connected to the plastic body of the robot with a rubber band. The father robot controls the microrobot by a kind of enamel covered copper wires with a diameter of 0.03 mm. The resistance of the wires could be ignored by the reason of its high flexibility. The dimensions of the microrobot are 24 × 24 × 3.5 mm. The dimensions of ICPF actuators are 17 × 3 × 0.2 mm.

5.5.2 Walking/rotating experiments in a water tank

Walking and rotating motions are two basic motions for the microrobot. To evaluate the performance of the basic motions of the robot, walking and rotating experiments were conducted in a water tank at a given control voltage of 8 V. The microrobot is connected to the control circuit with several copper wires. During the walking and rotating experiments, we changed the applied frequencies and calculated the walking and rotational speeds of the microrobot at each control frequency separately by recording its running time. To achieve an average speed, all experiments were repeated 5 times at a set of control signals.

The experimental results of walking and rotational speeds are shown in Figure 5-9. From the results, we achieved a maximum walking speed of 18.6 mm/s and a maximum rotational speed of 0.51 rad/s at a control frequency of 3 Hz. The walking speed of the robot is related to the step size and the control frequency. From our previous research results, we know that the step size is in inverse proportion to the applied frequency.

Therefore, with the control frequency increasing, the average walking speed will increase at first and then decrease to zero. So does the rotational speed.

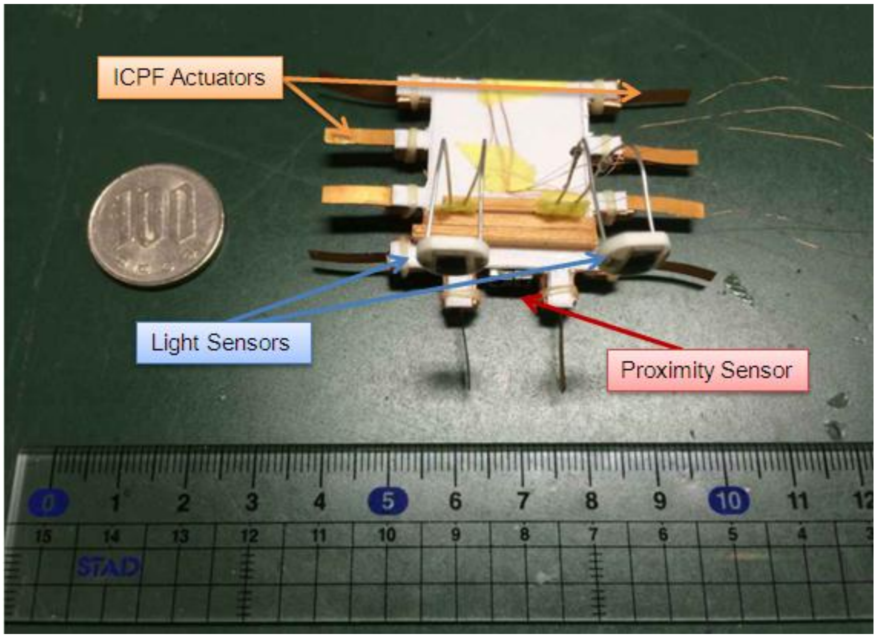

Figure 5- 8 The prototype microrobot

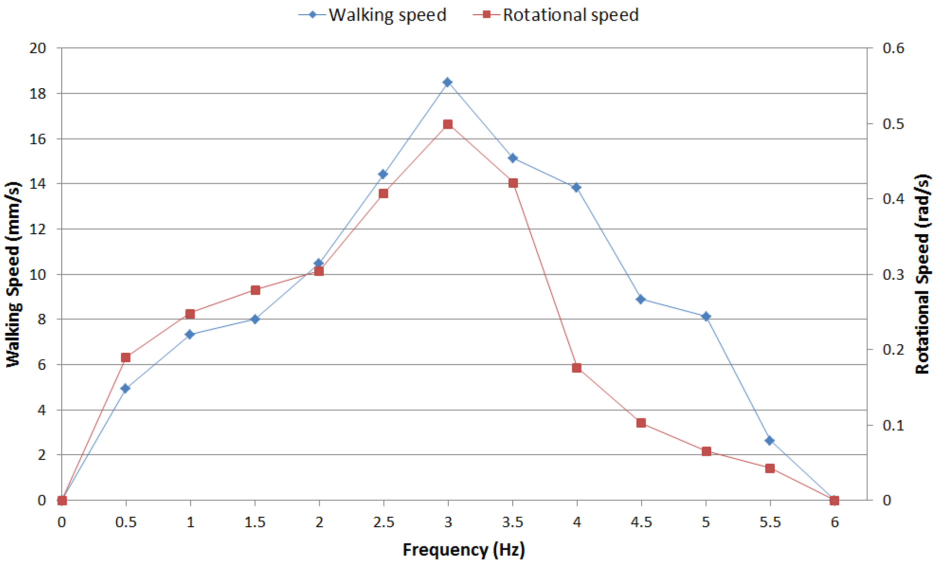

Figure 5- 9 Experimental results for the eight-legged microrobot

5.5.3 Grasping experiments

To implement the autonomous underwater object recovery, an infrared proximity sensor was mounted on the robot between the two ICPF hands, as shown in Figure 5-8. The dimemsions of the sensor is 10 × 5 mm and the weight of it is 0.7 g. As we mentioned in Section 3, the measurable distance range of the sensor is from 0 cm to 6 cm and the detectable output voltage is from 200 mV to the power voltage. During the experiments, the robot was programmed to move along the configured path. When the microrobot gets close to the target object, the micro-controller mounted on the father robot will receive data from the proximity sensor and then judge the realtime distance to the target. According to the detected distance, the robot will open the ICPF hands at a distance of over 20 mm to the target and then close them to grasp the object when the distance to the target is less than 10 mm.

We carried out the grasping experiments to evaluate its performance. At first, the robot was controlled to move along the pre-setting route. When the proximity sensor carried on the robot detected the target around 20 mm away, the robot began to open their hands. The ICPF hands were kept open until the target was detected around 10 mm away from the proximity sensor. At a distance of 10 mm from the target, the robot closed the ICPF hands to grasp the object. Then the robot carried the target object to the desired location.

5.6 Summary

A crayfish-like son robot for the father-son robot system has been developed. The son robot is an ICPF actuator-based microrobot. The crayfish-inspired son robot is adopted as the manipulator of the father-son robotic system. The son robot is actuated by ten ICPF actuators, which can perform walking, rotating and grasping motions underwater. A proximity sensor is mounted in front of the microrobot to implement the function of autonomous grasp.

The walking, rotating and grasping experiments are conducted to verify the performance of the basic motions of the robot. From the experimental results, a maximum walking speed of 18.6 mm/s and a maximum rotational speed of 0.51 rad/s at a control frequency of 3 Hz are achieved.

Chapter 6

Proposed biomimetic cableless son robot as the manipulator

6.1 Design of the underwater mcrorobot

The cableless microrobot carried on the father robot is driven by the ICPF actuators. To operate the underwater mission of the object recovery, the cableless microrobots should be capable of multi-functional motions, including finding and recycling the target object remotely controlled by the father robot. Two light sensors are mounted on the front part of each microrobot to receive the control signals from the father robot, which controls two sets of the blue LED lights to light up/off orderly. Additionally, a red LED light and a green LED light mounted on the microrobot are used as the indicator lights to show the indication signals of receiving the infrared signals. Without cables, the microrobot can be launched by one father robot to recycle object and then received by another one.

A biomimetic cableless microrobot is proposed to be the manipulator of the father robot, as shown in Figure 6-1 [46]. The microrobot consists of a main body, a transparent front cover and nine ICPF actuators, including two fingers for grasping motion, one tail fin for swimming motion, and two supporters and four drivers for walking, rotating and floating motions. Nine actuators are all 20 mm long, 5 mm wide and 0.2 mm thick and have one degree of freedom. It weighs 68.24 g. Two light sensors are mounted on the front part of the microrobot right behind the transparent cover. Moreover, two indicator lights are carried on the microrobot.

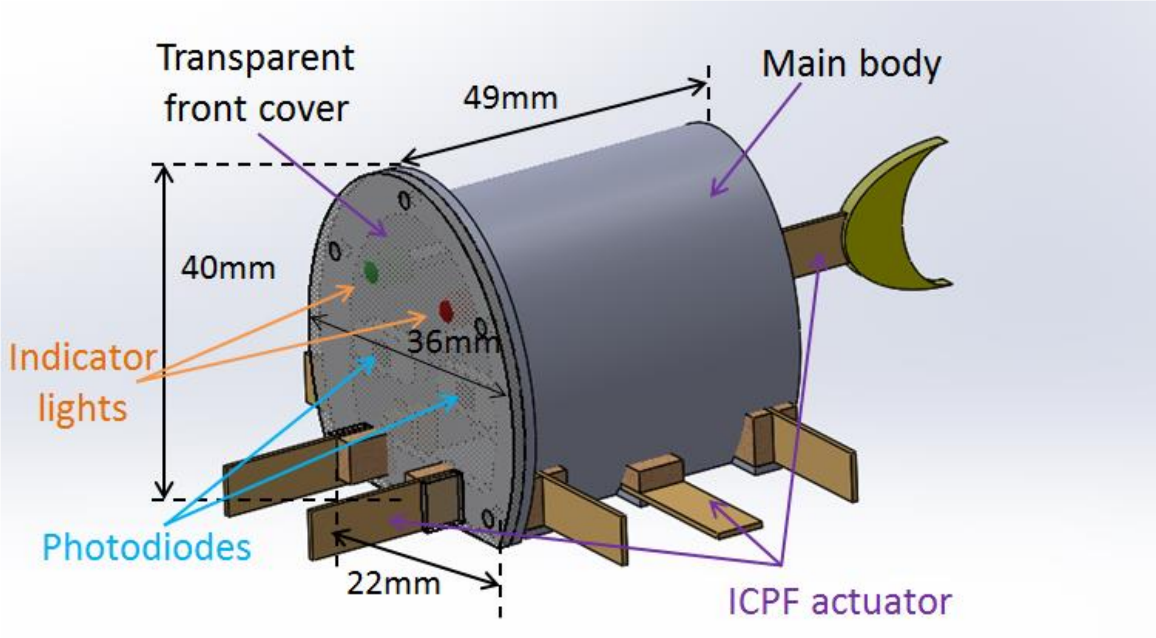

Figure 6- 1 The proposed wireless microrobot

6.2 Mechanisms of the walking and rotating motions

The microrobot is actuated by four drivers and two supporters which are driven by the square signals with the same oscillating frequency. And the phases of the supporters are set to lag behind the phase of the drivers by 90 °. Figure 6-2 shows one step cycle of the moving forward motion of the microrobot. When the four drivers bend to the same direction, the robot will walk forwards or backwards. When the drivers on different side of the robot bend to two different directions, the robot will rotate in clockwise or counterclockwise.

We assumed that the tip displacement of ICPF actuator is equal to $d/2$. Then an average speed of the microrobot can be achieved by (Eq. 5-1).

$$v = d * f \qquad \text{(Eq. 5-1)}$$

where d is the moving distance of the microrobot in one step cycle, v is the average speed and f is the control frequency.

6.3 Proposed underwater communication system

Nowadays, there are several kinds of communication methods, including radio communication, acoustic communication and optical communication. However, underwater robots cannot employ radio frequency signal for communication as its high attenuation underwater. As an established technology, acoustic underwater communication typically requires high power and high cost, and delivers low data rates, and is used for relatively large devices. Therefore, it is difficult for small underwater robots to use it. And optical communication becomes a compact, high-data rate and inexpensive alternative, which is used for short-to-median distance communication [41]-[43]. Compared with laser-based communication systems, LED-based communication systems with the characteristics of low cost, small size and no stringent requirement on directionality are appropriate for smallsized underwater robots. And the light attenuation of blue light is less than that of others in clear water.

Consequently, in order to realize the communication among the father robot and several son robots, we designed a blue LED-based underwater optical communication system, including the transmitter, the receiver and an agreed communication protocol between them. In our design, the super blue LED is applied as the transmitter and the photodiode is used as the receiver. The receiver on the robot can acquire the light signal which is emitted by the transmitter. The blue LED is sealed in a plastic bag for waterproof. To implement high efficiency and low cost underwater, an Advanced Photonix PDB-V107E with the advantages of high response and low noise is employed as the light sensor, which is a blue enhanced photodiode and enlarges the sensitivity of blue light.

We evaluated the performance of the communication system before equipping the light sensors on the microrobot. A photodiode and a blue LED constitute an optical coupler. The experiments are conducted in a huge water tank. In order to avoid interference generated by other light sources, during the whole experiments only the blue LED can be lighted on. The experimental setup of the communication system is placed in a water tank including a blue LED and a photodiode, as shown in Figure 6-3 (a). When the center of the photodiode and the center of the blue LED are in a straight line, we set the input angle of blue LED to 0 °, as show in Figure 6-3 (b). We measured the signal strength detected by the photodiode by changing the input angle and the transmission distance for the communication performance test.

Three kinds of communication experiments are carried out. The first one is to detect the variation of the signal strength under a fixed input angle of 0 ° and different transmission distances. In this experiment, we place a blue LED in a fixed position in the water tank and place the photodiode from the transmitter at 24 different distances. We used the photodiode to measure the signal strength at intervals of 5 cm. Figure 6-4 shows the experimental results of signal strength at different transmission distances. From the results, the detected signal strength declines as the distance between the transmitter and the receiver increases. The communication system can be applied at a maximum transmission distance of 120 cm, which is enough for the communication between the father robot and the son robot.

The second experiment is conducted to detect the variation of the signal strength under different input angles at a fixed distance of 45 cm.

The photodiode is placed in a fixed position in the water tank and the blue LED is placed from the receiver at a constant distance of 45 cm with different input angles in the angular range from 0 º to 60 º. The experimental results of signal strength under different input angles are shown in Figure 6-5. As the input angle of the blue LED increases from 0 º to 60 º, the signal strength detected by the photodiode decreases. When the input angle is set over 60 º, the photodiode cannot detect any signal strength. Therefore, the photodiode shows a better performance when it is placed from the blue LED at a distance of 120 cm and at an input angle of 0 º.

The third experiment is to measure the detectable range of the photodiode in the coverage area of the blue LED, as shown in Figure 6-3 (b). We measured the detectable maximum distance of the photodiode at different input angles in the angular range from -60 º to 60 º. As the signal strength detected by the photodiode less than 0.05 V cannot enable the communication, the maximum distances with measured signal strength over 0.05 V at different input angles constitute the detectable range of the communication system. We recorded the maximum transmission distance at intervals of 10 º. The experimental results of the detectable range are shown in Figure 6-6. From the graph, with the increasing input angle, the detectable range of the system declines. Within this range, the light sensor can detect the signal strength emittd by the blue light source well.

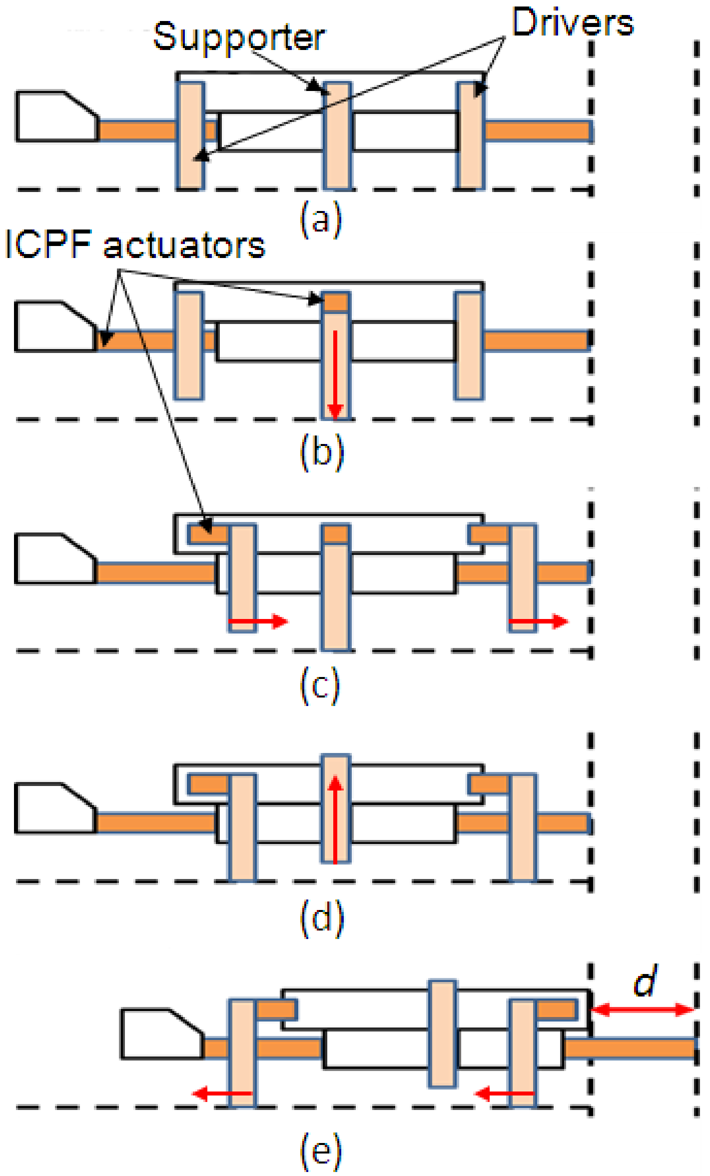

Figure 6- 2 One step cycle of walking motion: (a) In the initial state; (b) Two supporters bending downwards to lift the body up; (c) Four drivers bending forwards; (d) Two supporters bending upwards to use the drivers to lift the body up; (e) Four drivers bending backwards to make the robot move forwards. (The red arrows indicate the moving direction of each leg)

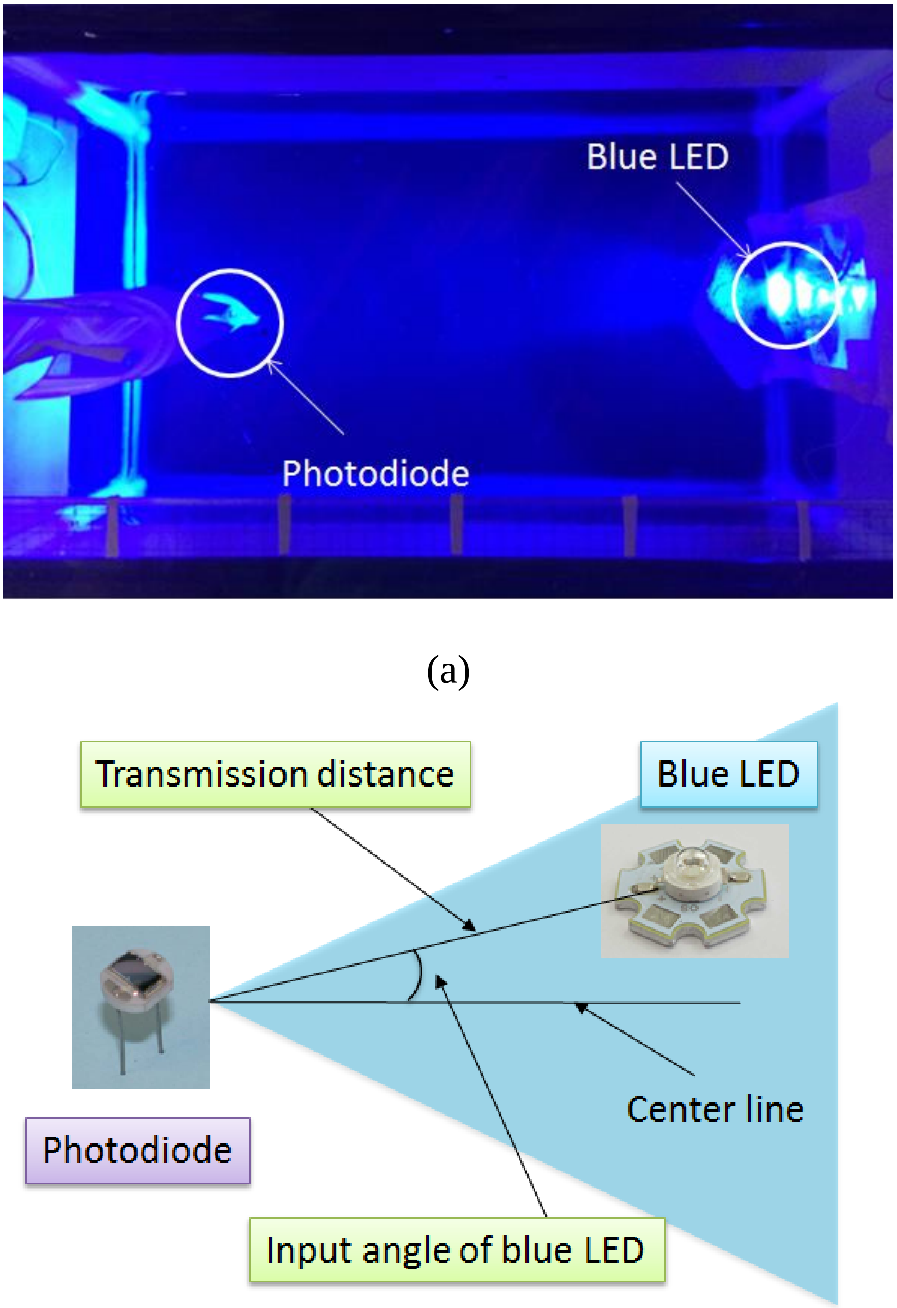

(a)

(b)

Figure 6- 3 (a) The experimental setup for performance evaluation of communication system in a water tank and (b) illustration of experimental variables

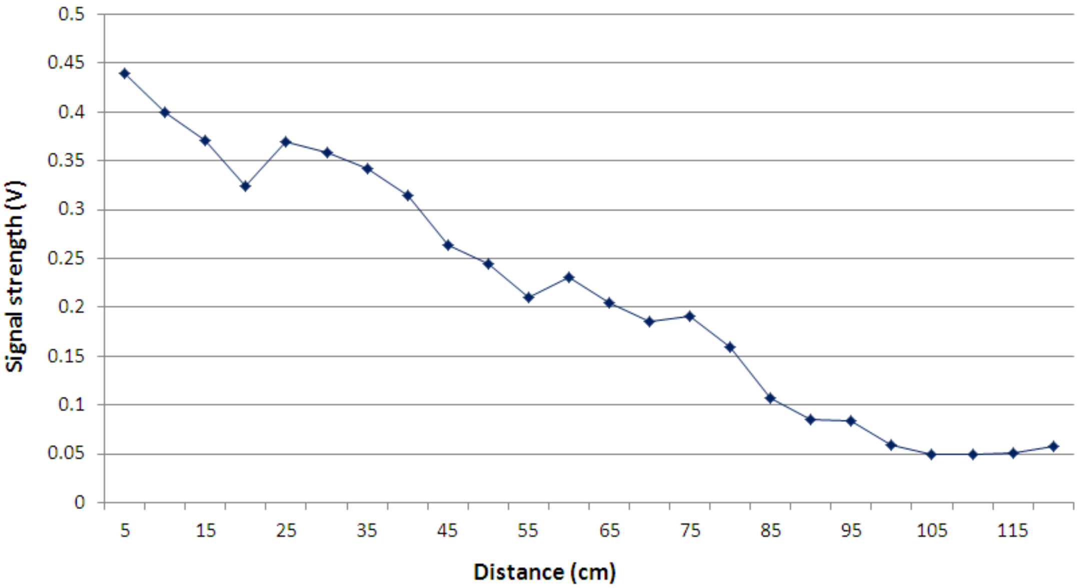

Figure 6- 4 Experimental results of signal strength at different transmission distances

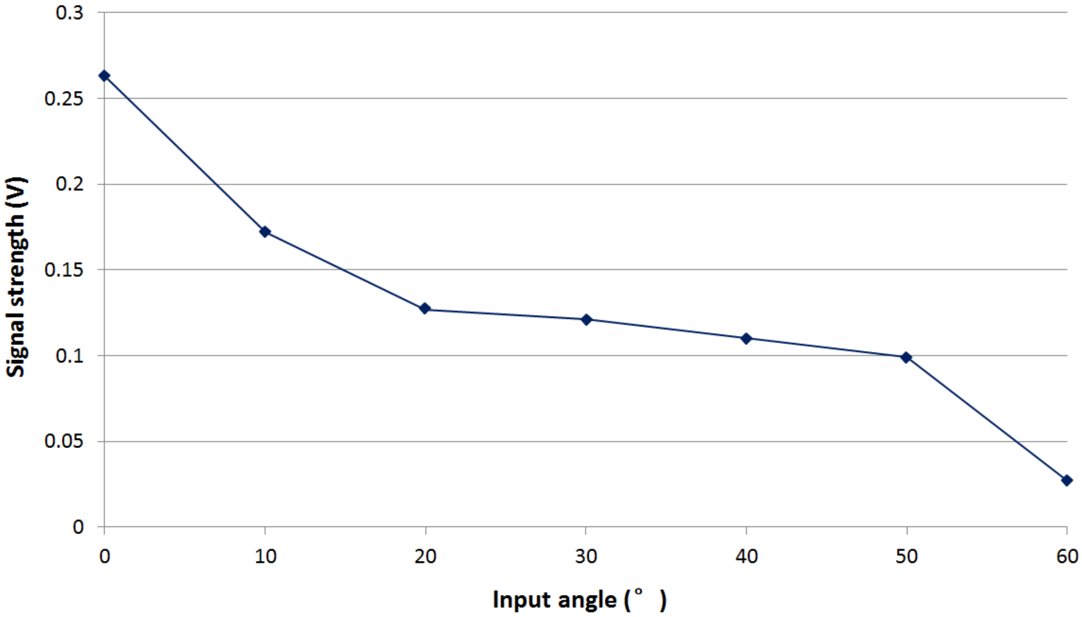

Figure 6- 5 Experimental results of signal strength under different input angles at a distance of 45 cm

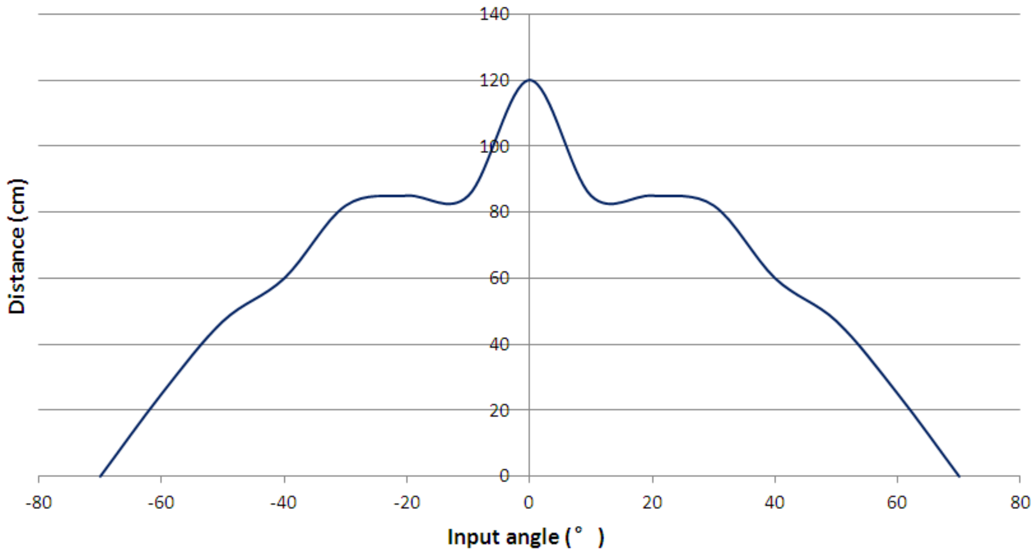

Figure 6- 6 Detectable range of the communication system

6.4 Communication protocol

A blue LED-based underwater optical communication system is proposed for the communication between the amphibious father robot and the microrobots, as shown in Figure 6-7. A new communication protocol is proposed to facilitate the communication. To control the microrobot to complete the assigned work, an 8-bit binary encoding consisted of one parity bit, three control bits and four numerical bits need to be sent to the microrobot from the father robot. The parity bit indicates whether a correct 8-bit binary encoding is sent or not. Also, three control bits that can form eight different combinations are employed to correspond to eight different functions of the microrobot, as shown in Table I. Additionally, four numerical bits indicate the numerical values of the corresponding function of the microrobot.

For the microrobot, two light sensors (sensor 1 and sensor 2) attached to the front part are applied to receive binary bits from the father robot. Binary value 0 is defined when the difference of the received voltage between sensor 1 and sensor 2 is greater than 20 mV. On the contrast, binary value 1 is defined when the difference of the received voltage between sensor 1 and sensor 2 is less than -20 mV. The initial voltage value of the two light sensors is 0. The received voltage value of the light sensor will be changed as a function of the intensity of the blue LED light and the value increases smoothly as the distance between the sensor and the blue LED light decreases.

The father robot sends a binary bit to the microrobot by two sets of blue LED lights located on the left side (Blue LED 1) or the right side (Blue LED 2) of the quarter spherical shell respectively, as shown in Figure 2-2. When the father robot turns on the Blue LED 1, the voltage value received by sensor 1 is greater than that received by sensor 2 due to the relatively smaller distance between Blue LED 1 and sensor 1. Thus, the microrobot receives binary value 0. Inversely, the microrobot receives binary value 1 when the Blue LED 2 is turned on. The corresponding indicator light (red LED light or green LED light) will be lightened according to the received binary value 0 or 1 respectively, which provides a feedback to the father robot.

The control protocol between the father robot and the microrobot is described as following:

1) The microrobot turns on the red and green indicator lights simultaneously and keeps the two lights on for two seconds to send the father robot a status feedback that the microrobot is waiting for a binary value of an 8-bit control instruction;

2) The father robot detects the status of the red and green LED lights by the camera module. If the two LEDs are both lightened, the father robot starts to send an 8-bit control instruction;

3) The father robot sends an 8-bit control instruction made up of the binary value 0 and 1 by turning on the Blue LED 1 or Blue LED 2 respectively;

4) The microrobot receives the 8-bit control instruction by computing the difference of the received voltage between the two sensors and then turns on the red LED light or green LED light according to the received binary value 0 or 1 respectively;

5) The father robot detects the feedback from the microrobot through the camera module. If the microrobot receives a correct bit, the father robot prepares to send the next binary bit. Otherwise, father robot sends an error code with parity bit 0 to the microrobot to stop the current communication;

6) The process repeats from step 1) to step 5) until the microrobot receives a correct 8-bit control instruction; then the microrobot turns off the red and green LED lights simultaneously and starts the corresponding work according to the 8-bit control instruction. After the work is completed, the two indicator lights will be lightened.

TABLE I. Binary encoding rules for the motion control of the microrobot

Parity b	**Control bits**			**Numerical bits**				**Functions**
Bit7	Bit 6	Bit 5	Bit 4	Bit 3	Bit 2	Bit 1	Bit 0	
1	0	0	0	0<N≤15				Walking forward N steps
1	0	0	1	0<N≤15				Walking backward N steps
1	0	1	0	0<N≤15				Rotating in clockwise
1	0	1	1	0<N≤15				Rotating in anticlockwise
1	1	0	0	0	0	0	0	Grasping
				0	0	0	1	Loosening
1	1	0	1	0<N≤15				Floating N steps
1	1	1	0	0<N≤15				Swimming N steps
1	1	1	1	0	0	0	0	Returning (Received by father robot)
				1	1	1	1	Stop all the motions
0	0~8			0~15				Error codes

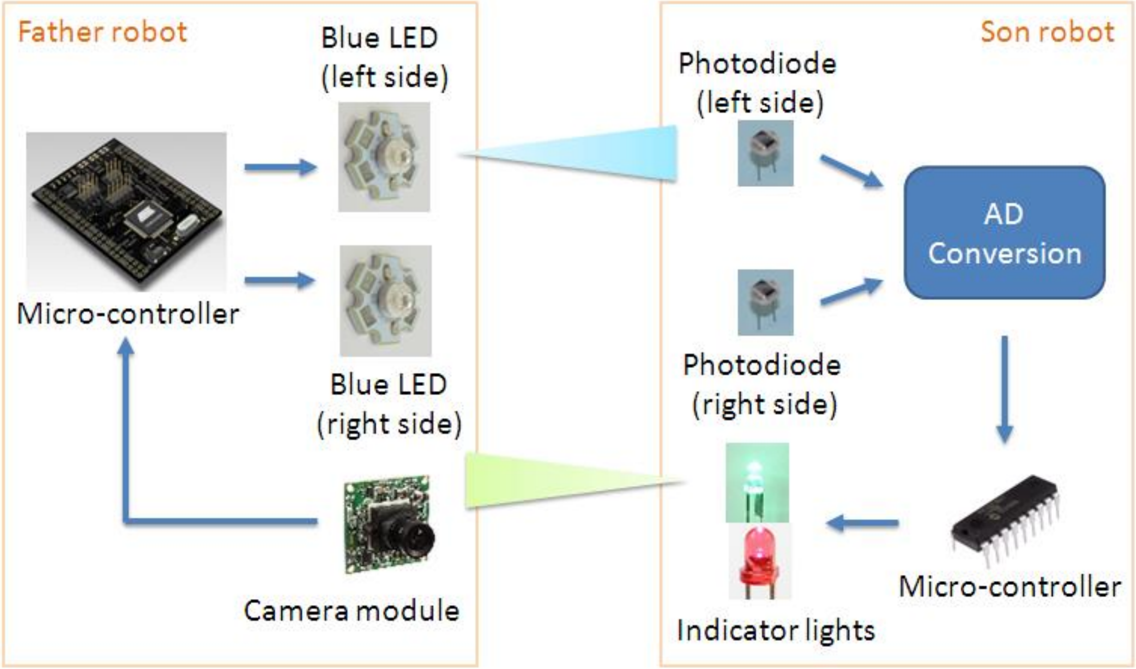

Figure 6- 7 The general structure of the underwater optical communication system

6.5 Prototype microrobot and experiments

6.5.1 Prototype microrobot and performance evaluation of the ICPF actuators

A prototype biomimetic wireless underwater microrobot is developed, as shown in Figure 6-8 (a). The power supply of the microrobot is two 3.7 V Li batteries with a 200 mAh capacity. The control center of the microrobot is based on a PIC16 microcontroller. The control circuit of the microrobot is shown in Figure 6-8 (b). The volume of the body of the microrobot is 62.314 cm^3 and the weight of it is 68.245 g.

Before we decide the value of the applied control voltage, we did the performance evaluation of the ICPF actuator. The tip displacement of the ICPF actuator is related to the applied voltage. In order to get an appropriate voltage for the ICPF actuator control, we apply different voltages on both electrodes of ICPF to measure the change of the tip displacement with time. We conduct the experiments in both water and salt water with a density of 3.4 %. During the experiments, as the change of the tip displacement at a control voltage over 5 V become large with time which is not suitable for the microrobot actuation, the control voltage is set in a range from 1 V to 5 V. Figures 6-9 and 6-10 show the experimental results of the change of the tip displacement of the ICPF actuator with time in water and salt water respectively. From the results, applying a voltage over 4 V to the ICPF actuator shows a better performance of tip displacement. Considering that a large tip displacement will be better for the movement of the robot, the driving voltage is set to be 5 V.

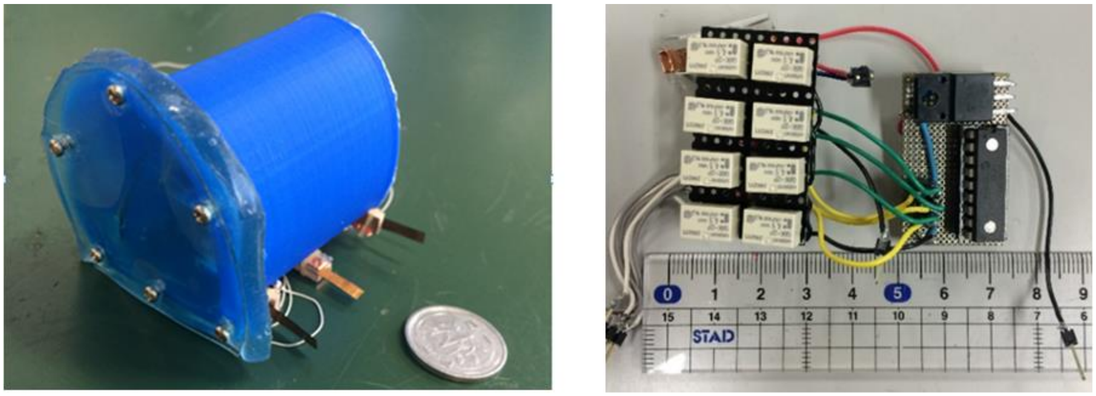

(a) (b)

Figure 6- 8 (a) The prototype microrobot and (b) the control circuit

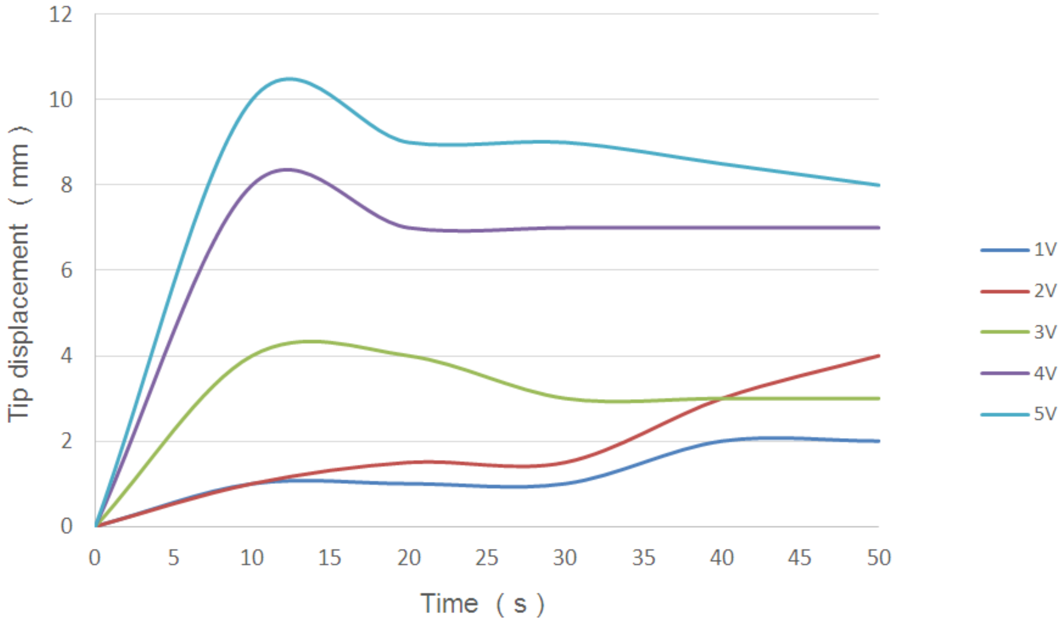

Figure 6- 9 Experimental results of the change of the tip displacement of the ICPF actuator with time (in water)

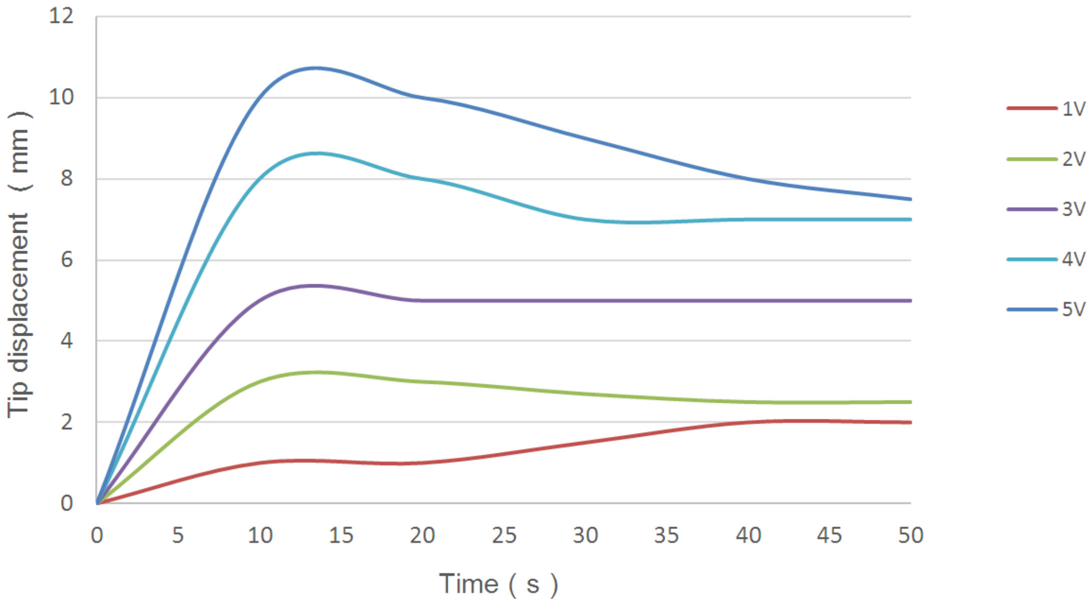

Figure 6- 10 Experimental results of the change of the tip displacement of the ICPF actuator with time (in salt water)

6.5.2 Experiments of walking and rotating motions in a water tank

Walking and rotating experiments of the microrobot were conducted in a water tank to evaluate the performance of the robot at a given control voltage of 5 V. During the experiments, we changed the control frequency and calculated the walking speed and rotational speed of the microrobot in each signal by recording the time separately. All experiments were repeated five times at a set of control signals to achieve an average speed. The experimental results of walking and rotating motions are shown in Figures 6-11 and 6-12 respectively. From the results, a maximum walking speed of 9.85 mm/s and a maximum rotational speed of 13.13 °/s were achieved at a control frequency of 1.25 Hz. As we mensioned in Chapter 5, the tip displacement of the

ICPF actuator will decrease as a function of control frequency. According to (Eq. 5-1), the average speed of the robot is related to the step distance and the frequency. Consequently, with the control frequency increasing, the speed will increase at first and then decrease to zero.

6.5.3 Communication experiments

To realize the communication between the father robot and the microrobot without cables, a new communication protocol is proposed. Moreover, an experiment setup is established for the communication experiments to verify the proposed communication protocol, as shown in Figure 6-13 (a). The experiment setup is consisted of an blue LED light, a PIC micro-controller of microrobot, two indicator lights, two LED lights, in which the red LED indicates a successful receiving of the signal 1 (a specified 8-bit binary encode) and the green LED indicates a successful receiving of the signal 2 (another specified 8-bit binary encode). Using this experiment setup, two kinds of experiments were conducted by sending two kinds of signals: signal 1 and signal 2, as shown in Figure 6-13. During the experiments, the process repeats 8 times from step (a) to (c) until the microrobot receives an 8-bit control instruction. When the microrobot receives signal 1, the red indicator light is turned on, as shown in Figure 6-13 (d); when it receives signal 2, the green light is turned on, as shown in Figure 6-13 (e). From the results, we know that this communication protocol can be used to realize the communication between the father and son robots.

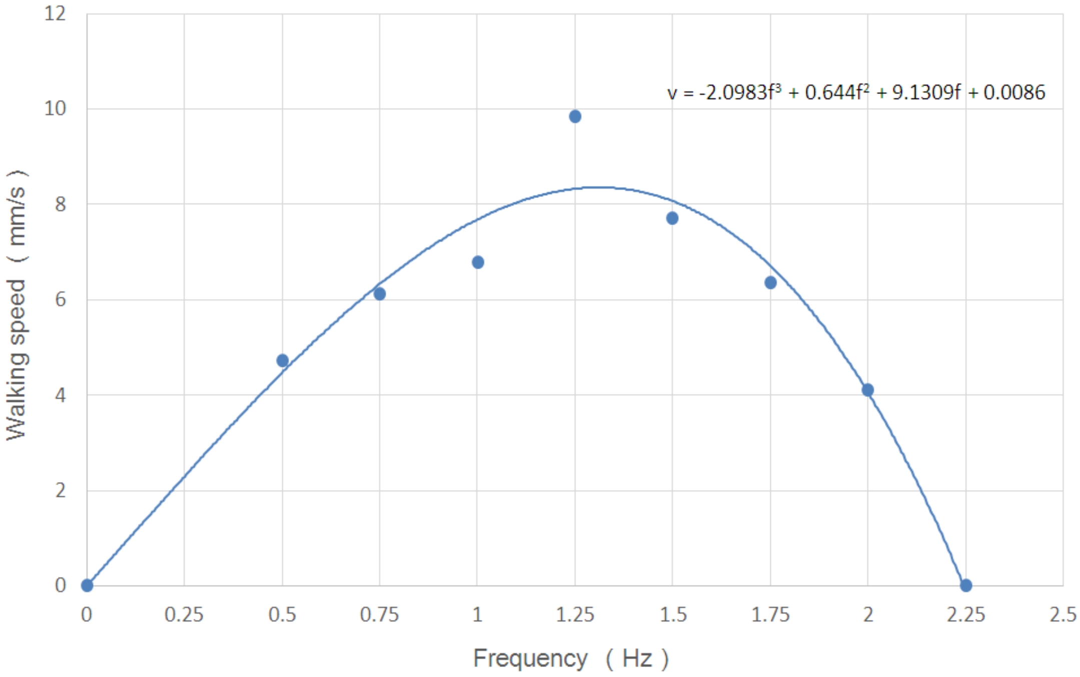

Figure 6- 11 Experimental results of the walking motion

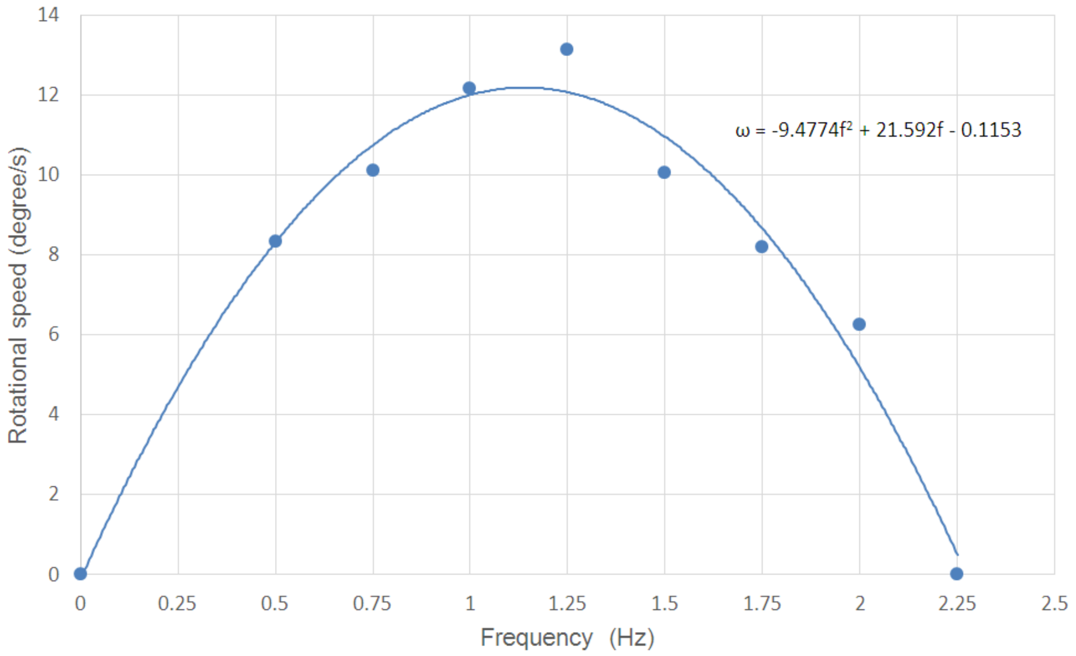

Figure 6- 12 Experimental results of the rotating motion

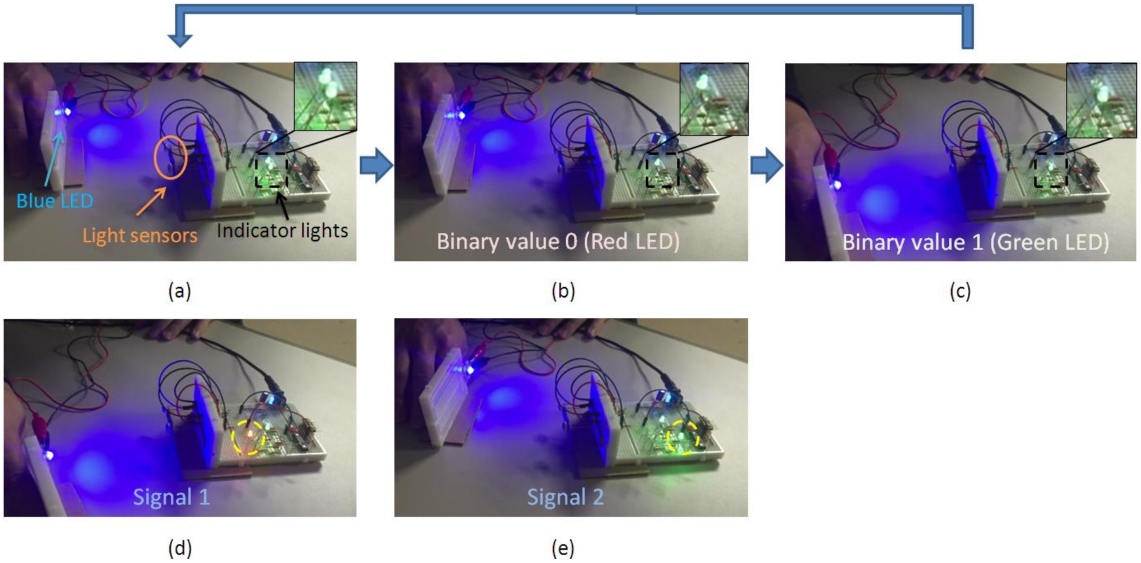

Figure 6- 13 Communication experiments: (a) The blue LED light can be lightened to send optical signals when the two indicator lights are on; (b) The indicator light on the left side is turned on when the light sensor on the left side receives a higher light intensity than the other side; (c) The indicator light on the right side is turned on when the light sensor on the right side receives a higher light intensity than the other side; (d) When the micro-controller receives signal 1, the red LED is lightened; (e) When the micro-controller receives signal 2, the green LED is lightened

6.6 Summary

A biomimetic wireless microrobot has been developed as the manipulator of the father-son robotic system. The microrobot is actuated by nine ICPF actuators. It can implement the walking, rotating and grasping motions. In order to realize the communication between the father robot and son robots, a blue LED-based underwater optical communication method was proposed. A novel communication protocol was proposed for the communication between the father robot and son robot. The father robot is able to carry the ICPF actuator-based wireless microrobot and send the optical signals to control the motion of it.

A blue LED-based underwater optical communication system is designed to enable the communication between father robot and son robot for microrobot recovery. The underwater experiments were carried out to evaluate the performance of the optical communication system. From the results, the photodiode can detect the blue LED at a maximum distance of 120 cm. By measuring the detectable maximum distance of the photodiode at different input angles, we achieve the detectable range of the communication system.

The walking and rotating experiments were conducted to evaluate the performance of the robot. From the experimental results, a maximum walking speed of 9.85 mm/s and rotational speed of 13.13 °/s were achieved at a control frequency of 1.25 Hz. Finally, the communication experiments were carried out to verify that the proposed communication protocol can be used for the communication between the father and son robots.

Chapter 7

Deployment and recovery of the manipulator by the father robot

7.1 Fixture/release mechanism of the microrobots

In order to integrate the son robot into the father robot to form a father-son robotic system, the fixture and release mechanism is proposed. For carrying and deploying the microrobots, we developed a fixture mechanism installed on lower hemisphere of the amphibious robot. To simplify the control system, we propose a mechanism with no actuating parts, as shown in Figure 7-1. It is a block that can move up and down freely on a plate. When the amphibious robot walks on land or swims underwater, the block falls down to fix the position of the microrobots by gravity. When deploying the microrobots, the four actuating units rotate upwards to allow the robots to be supported by the plate, and push the block up so that the micro-robots can leave the amphibious robot.

The microrobot can be carried and deployed by the amphibious robot with the simple fixture mechanism. The mechanism has no actuating parts, which consists of a block that can move up and down freely on a plate in the lower hemisphere. The block on the amphibious robot drops down by gravity to fix the position of the microrobot, during walking on land or swimming underwater. When the amphibious robot deploys the micro-robot, the four actuating units rotate upwards to allow the robots to be supported by the plate, and push the block up so that the micro-robot can leave the amphibious robot. To prove the feasibility of the fixture and deployment mechanism, the microrobot deployment experiment was conducted on the bottom of the pool, as shown in Figure 7-2.

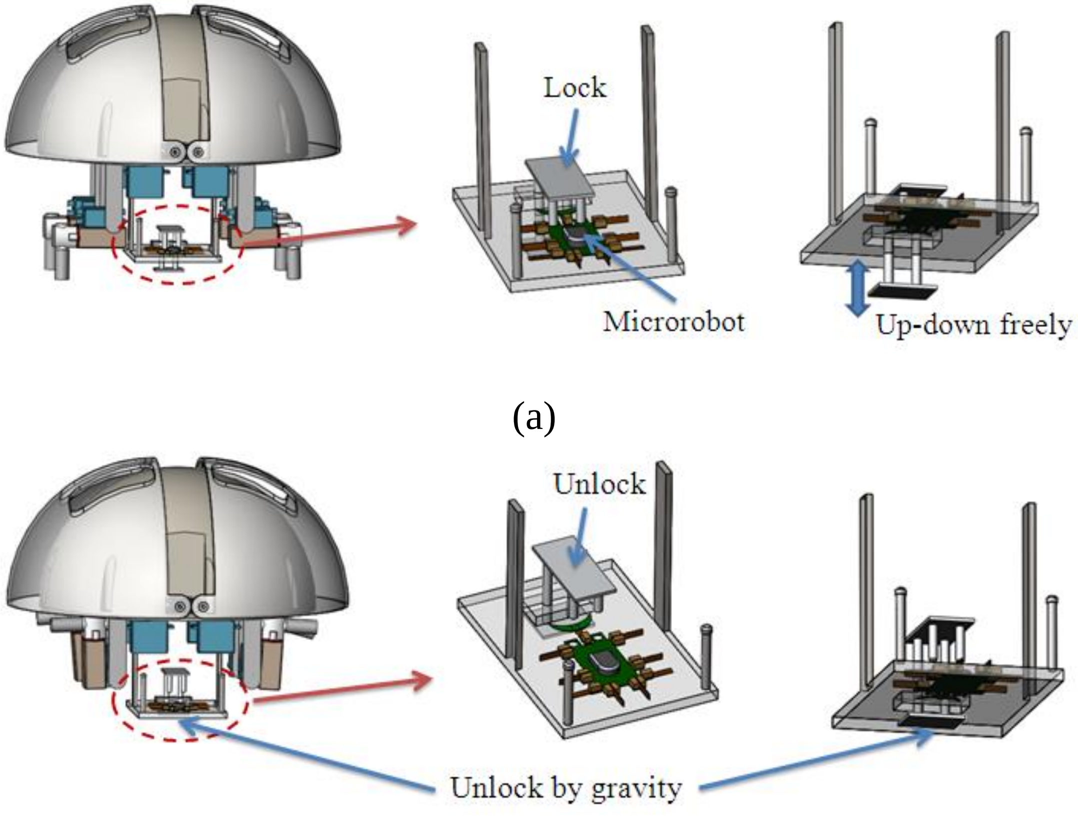

(a)

(b)

Figure 7- 1 Fixture mechanism of the micro-robots: (a) locked state and (b) free state

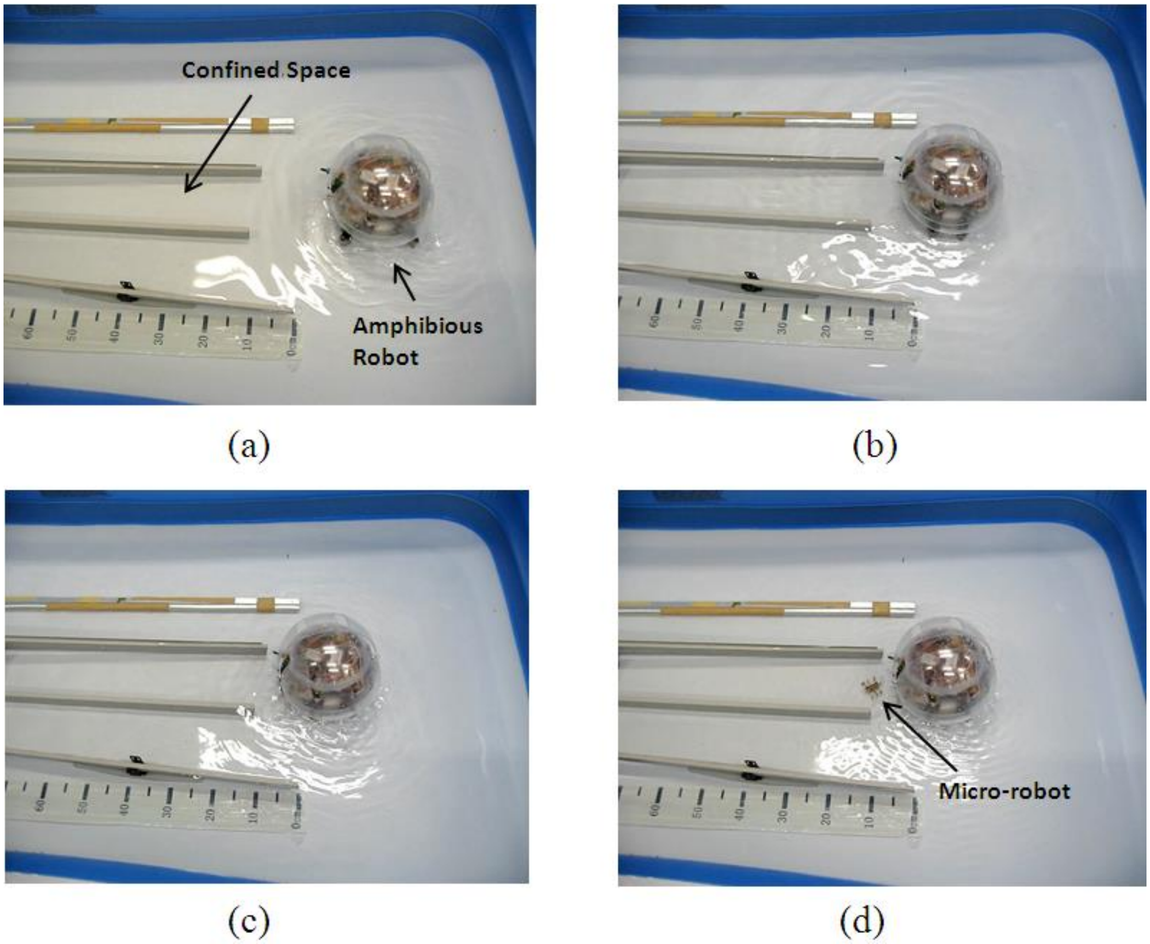

(a) (b)

(c) (d)

Figure 7- 2 Microrobot deployment experiment: (a) initial position, (b) encountering a confined space, (c) deploying the microrobot and (d) microrobot enters the confined space

7.2 Recovery mechanism of the microrobots

For the father-son robot system, the father robot should recover the microrobot with the target object after the son robot finished the underwater tasks. In order to realize the microrobot recovery, a blue LED-based underwater optical communication system is designed for the father-son robot system. A super blue LED is installed on the shelf of the lower hemisphere, which is used as transmitter of the optical communication system. And two light sensors used as the receiver are mounted in front of the microrobot symmetrically. The two receivers on the microrobot can acquire the light signal emitted by the transmitter.

By comparing the strength of light signal received by the two light sensors, the microrobot is able to change its motion among walking straight, turning left and turning right motions. When the signal strength acquired by the photodiode on the left is larger than that acquired by the photodiode on the right, the microrobot will turn left. On the contrary, the microrobot will turn right. We conducted the blue LED tracking experiments in a water tank, as shown in Figure 7-3. To avoid interference generated by other light sources during the whole experiments, only the blue LED is lighted on. During the experiments, the microrobot turned left until it faced to the blue LED, and then moved to the LED straightly. From the experimental results, we know that the son robot can realize the tracking motion underwater.

Thus, the microrobot will track the blue LED carried on the bottom of the father robot for son robot recovery. With the function of tracking the blue LED, the microrobot can get back to the father robot.

7.3 Summary

To implement the father-son robotic system, the fixture/release and recovery mechanisms are proposed for the manipulator release and recovery. The microrobot deployment experiment was carried out to prove the feasibility of the fixture and deployment mechanism. And, we conducted the blue LED-based tracking experiments. From the results, the robot can realize the function of LED tracking motion underwater. With the function of tracking blue LED, the son robot can be recovered by the father robot.

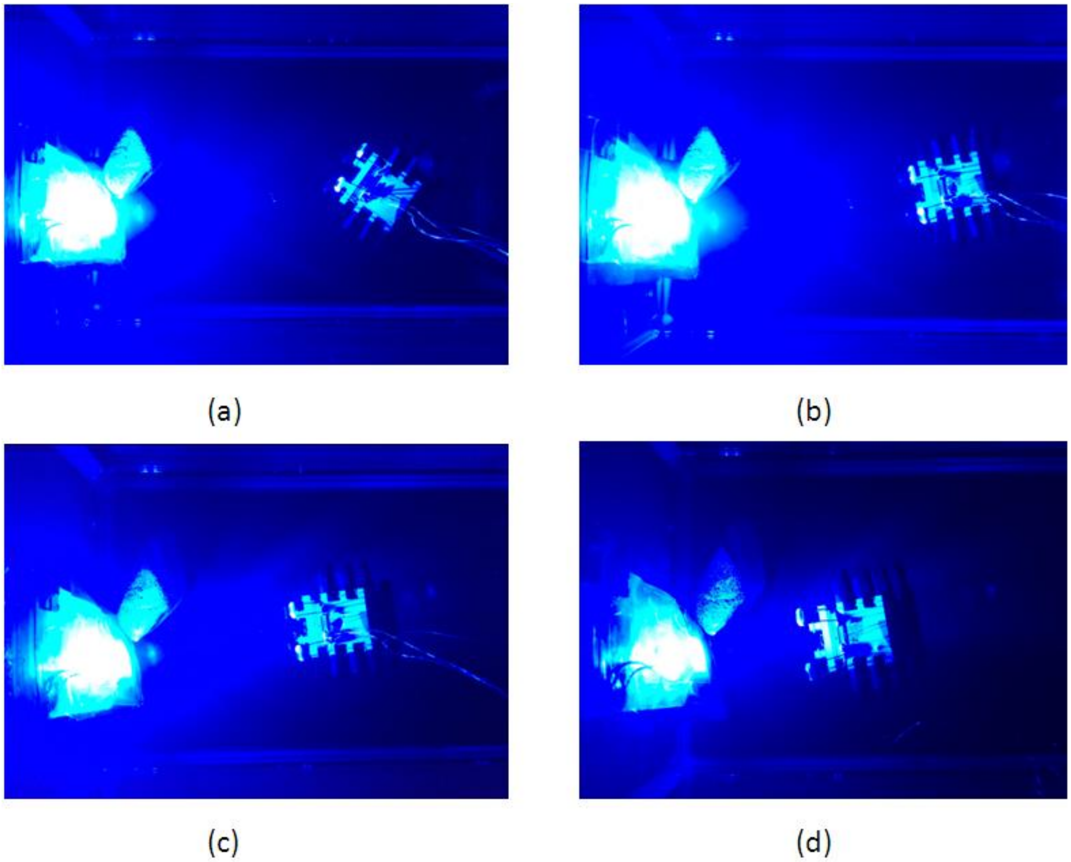

Figure 7- 3 Blue LED tracking experiments

Chapter 8

Conclusions and future work

8.1 Conclusions

This thesis presents an amphibious father-son robotic system for the underwater intervention tasks (Chapter 2), which is consisted of an amphibious spherical father robot with three actuation modes (Chapter 3) and two kinds of microrobots used as the manipulators of the system (Chapter 5 and Chapter 6).

An amphibious spherical father robot was proposed with three actuation modes, including the quadruped walking mode, roller-skating mode and water-jet propeller mode. The father robot consists of a sealed upper hemispheroid, two quarter spherical shells, and a plastic circular plate. The robot is capable of motion on land, as well as underwater.

The on-land and underwater performance of the amphibious robot was evaluated. A braking mechanism was proposed to realize the transformation of state of each passive wheel between free rolling and braking states by controlling the vertical servo motor to compress and release the spring. The braking mechanism can be used as a transformation mechanism to apply a walking gait to the wheeled robot to implement walking motion meantime. Hence, the experiments on smooth flat terrains and down a slope were described to evaluate the performance of roller-skating motion. Additionally, plenty of walking experiments of the robot with walking gait are conducted.

At low frequencies, the sliding velocity and walking velocity on the flat terrain were roughly equal. A maximum walking velocity of 22 cm/s was achieved. At a control frequency of 5.56 Hz, we got a maximum roller-skating velocity of 37.8 cm/s. And the robot was able to move down a slope with an incline of 10 ° with roller-skating gait. Roller-skating gait showed a better performance than walking gait in terms of mobile velocity and energy efficiency, especially moving down a slope.

Since there is a different step loss for four legs during walking, the direction of movement of the robot is unstable. For the improvement of the walking stability of the wheeled robot in longitudinal direction, we proposed a closed-loop control method by carrying a gyroscope sensor to measure the yaw angle of the robot in real time. And we conducted plenty of walking experiments to evaluate a good performance of directional control.

Additionally, underwater thrust and velocity experiments in the semi-submerged state were conducted to evaluate the underwater performance. Under a duty of 100 %, a maximum thrust of 180 mN in horizontal direction, and a maximum upward thrust of 333.2 mN and a downward thrust of 362.6 mN in vertical direction were got.

Furthermore, a maximum surge velocity of 16.1 cm/s and rotational velocity of 64.3 °/s were obtained, and a maximum rising velocity of 8.4 cm/s and a sinking velocity of 8.4 cm/s were achieved.

A crayfish-like son robot for the father-son robot system has been developed. The son robot is an ICPF actuator-based microrobot. The crayfish-inspired son robot is adopted as the mechanical arm of the father-son robot system. The son robot is actuated by ten ICPF actuators, which can perform walking, rotating and grasping motions underwater. A proximity sensor and two photodiodes are mounted in front of the microrobot to implement the functions of autonomous grasp and blue LED tracking.The walking, rotating and grasping experiments are conducted to verify the performance of the basic motions of the robot. From the experimental results, a maximum walking speed of 18.6 mm/s and a maximum rotational speed of 0.51 rad/s at a control frequency of 3 Hz are achieved.

A biomimetic wireless microrobot has been developed as the mechanical arm of the father-son robot system. The microrobot is actuated by nine ICPF actuators. It can implement the walking, rotating and grasping motions. In order to realize the communication between the father robot and son robots, a new cableless communication method was proposed. The father robot is able to carry the ICPF actuator-based wireless microrobot and send the optical signals to control the motion of it. Two light sensors were equipped on the microrobot to receive the optical data from the father robot and two indicator lights were used for the closed-loop control to the communication protocol.

A blue LED-based underwater optical communication system is designed to enable the communication between father robot and son robot for microrobot recovery. The underwater experiments were carried out to evaluate the performance of the optical communication system. From the results, the photodiode can detect the blue LED at a maximum distance of 120 cm. By measuring the detectable maximum distance of the photodiode at different input angles, we achieve the detectable range of the communication system.

The walking and rotating experiments were conducted to evaluate the performance of the robot. From the experimental results, a maximum walking speed of 9.85 mm/s and rotational speed of 13.13 º/s were achieved at a control frequency of 1.25 Hz. Finally, the communication experiments were carried out to verify that the proposed communication protocol can be used for the communication between the father and son robots.

The objective of my research is to present a novel father-son robotic system for underwater intervention missions. In this system, an amphibious spherical robot is designed and developed as the father robot, which has three actuating modes. Two kinds of smart actuator-based biomimetic microrobots are developed as the son robots of the father-son robotic system, which are mounted on the plastic plate in the lower hemisphere of the father robot to be used as the manipulators of the father robot.

1) To adapt to the complex underwater environments, an amphibious spherical father robot was developed with three actuating modes: quadruped walking mode, roller-skating mode and water-jet propulsion mode. To improve the walking stability, a closed-loop control method was employed to control the stability of the direction of movement.

2) To implement the underwater missions, two kinds of biomimetic son microrobots driven by smart actuators were developed as the manipulators of the father-son robotic system. Additionally, the launching and recovery mechanisms of the manipulators were designed.

3) To realize the communication between the father robot and the wireless son robot, a blue LED-based underwater optical communication system was designed.

8.2 Future work

Future work mainly involves the improvement of the on-land and underwater performance of the father-son robotic system and the implementation of carrying out image processing of the images taken by the camera module and the function of color recognition. And we consider using the father-son robotic tele-communication system to implement the underwater operations.

References

[1] S. Hirose, H. Yamada, “Snake-like robots [Tutorial]”, IEEE Robotics & Automation Magazine, Vol. 16, pp. 88–98, 2009.

[2] A. S. Boxerbaum, P. Werk, R. D. Quinn, R. Vaidyanathan, “Design of an autonomous amphibious robot for surf zone operation: Part I-Mechanical design for multi-mode mobility”, Proceedings of the IEEE International Conference on Advanced Intelligent Mechatronics, pp. 1459–1464, 2005.

[3] J. Yu, R. Ding, Q. Yang, M. Tan and J. Zhang, “Amphibious Pattern Design of a Robotic Fish with Wheel-propeller-fin Mechanisms”, Journal of Field Robotics, pp. 1-15, 2013.

[4] A. J. Ijspeert, A. Crespi, D. Ryczko, J. M. Cabelguen, “From swimming to walking with a salamander robot driven by a spinal cord model”, Science, Vol. 315, pp. 1416–1420, 2007.

[5] K. Tadakuma, R. Tadakuma, M. Aigo, M. Shimojo, M. Higashimori, M. Kaneko, “"Omni-Paddle": Amphibious Spherical Rotary Paddle Mechanism”, Proceedings of 2011 IEEE International Conference on Robotics and Automation, pp.5056-5062, 2012.

[6] G. Dudek, P. Giguere, C. Prahacs, S. Saunderson, J. Sattar, L. Torres-Mendez, M. Jenkin, A. German, A. Hogue, A. Ripsman, J. Zacher, E. Milios, H. Liu, and P. Zhang, M. Buehler, C. Georgiades,

"AQUA: An Amphibious Autonomous Robot", Computer, Vol. 40, No. 1, pp. 46-53, 2007.

[7] S. Zhang, X. Liang, L. Xu, M. Xu, "Initial Development of a Novel Amphibious Robot with Transformable Fin-Leg Composite Propulsion Mechanisms", Journal of Bionic Engineering, Vol. 10, No. 4, pp. 434-445, 2013.

[8] G. Endo, S. Hirose, "Study on roller-walker (system integration and basic experiments)", Proceedings of 1999 IEEE international conference on robotics and automation, pp 2032–2037, 1999.

[9] G. Endo, S. Hirose, "Study on roller-walker (Adaptation of characteristics of the propulsion by a leg trajectory)", Intelligent Robots and Systems, IROS 2008, pp. 1532–1537, 2008.

[10] G. Endo, S. Hirose, "Study on roller-walker (energy efficiency of roller-walker)", Proceedings of 2011 IEEE international conference on robotics and automation, pp 5050–5055, 2011.

[11] G. Endo, S. Hirose, "Study on Roller-walker (Multi-mode Steering Control and Self-contained Locomotion)", Proceedings of the 2000 IEEE International Conference on Robotics and Automation, pp. 2808-2814, 2000.

[12] X. Ding, K. Xu, "Design and analysis of a novel metamorphic wheel-legged rover mechanism", Journal of Central South University, (S1), pp. 91–101, 2009.

[13] S. Shen, C. Li, C. Cheng, J. Lu, S. Wang, P. Lin, "Design of a leg-wheel hybrid mobile platform", Intelligent Robots and Systems, IROS 2009, pp. 4682–4687, 2009.

[14] F. Michaud and S. Caron, "Multi-modal locomotion robotic platform using leg-track-wheel articulations," Autonomous Robots, pp. 137–156, 2005.

[15] G. Marani, S. Choi, J. Yuh, "Underwater autonomous manipulation for intervention missions AUVs", Ocean Engineering, Vol. 36, pp. 15–23, 2009.

[16] S. Mohan, J. Kim, "Indirect adaptive control of an autonomous underwater vehicle-manipulator system for underwater manipulation tasks", Ocean Engineering, Vol. 54, pp. 233–243, 2012.

[17] S. Mohan, J. Kim, "Coordinated motion control in task space of an autonomous underwater vehicle–manipulator system", Ocean Engineering, Vol. 104, pp. 155–167, 2015.

[18] G. De Novi, C. Melchiorri, J. C. Garcia, P. J. Sanz, P. Ridao, G. Oliver, "A New Approach for a Reconfigurable Autonomous Underwater Vehicle for Intervention" Systems Conference, 2009 3rd Annual IEEE. pp. 23-26, 2009.

[19] S.-C. Yu, J. Yuh, J. Kim, "Armless underwater manipulation using a small deployable agent vehicle connected by a smart cable",

Ocean Engineering, pp. 149-159, 2013.

[20] C. Yue, S. Guo, L. Shi, “Design and Performance Evaluation of a Biomimetic Microrobot for the Father-son Underwater Intervention Robotic System”, Microsystem Technologies, DOI: 10.1007/s00542-015-2457-z, 2015.

[21] R. Chase, A. Pandya, “A Review of Active Mechanical Driving Principles of Spherical Robots”, Robotics, pp. 1 – 21, 2012.

[22] X. Lin, S. Guo, K. Tanaka, and S. Hata, “Development and Evaluation of a Vectored Water-jet-based Spherical Underwater Vehicle”, INFORMATION: An International Interdisciplinary Journal, Vol. 13, No. 6, pp. 1985-1998, 2010.

[23] L. Shi, S. Guo, M. Li, S. Mao, N. Xiao, B. Gao, Z. Song, K. Asaka,“A Novel Soft Biomimetic Microrobot with Two Motion Attitudes”, Sensors, Vol. 12, No. 12,pp. 16732-16758, 2012.

[24] S. Guo, M. Li, L. Shi, S. Mao, C. Yue, “Performance Evaluation on Land of an Amphibious Spherical Mother Robot.” Proceedings of 2013 ICME International Conference on Complex Medical Engineering (ICME CME 2013), pp.602-607, 2013.

[25] P. Brunetto, L. Fortuna, S. Graziani, S. Strazzeri, “A model of ionic polymer–metal composite actuators in underwater operations”, Journal of Smart Material and Structures, Vol. 17, No. 2, pp. 025-029, 2008.

[26] Toshiba 4-legged nuclear plant inspection robot (2012). [Online]. Available: http://www.exponentialtimes.net/videos/toshiba-4-legged-nuclear-plant-inspection-robot/

[27] M. Li, S. Guo, H. Hirata, H. Ishihara, "Design and Performance Evaluation of an Amphibious Spherical Robot", Robotics and Autonomous Systems, doi:10.1016/j.robot.2014.11.007, Vol. 64, pp. 21–34, 2015.

[28] S. Zhang, Y. Zhou, M. Xu, X. Liang, J. Liu, J. Yang, "AmphiHex-I: Locomotory Performance in Amphibious Environments With Specially Designed Transformable Flipper Legs", IEEE/ASME Transactions on Mechatronics, Vol. 21, No. 3, pp. 1720–1731, 2016.

[29] Kim, H. J., “Smart Soft-morphing Structure: Design, Manufacturing, and Application,” Ph.D. Thesis, School of Mechanical and Aerospace Engineering, Seoul National University, 2011.

[30] Chen, Z., Shatara, S., and Tan, X., “Modeling of biomimetic robotic fish propelled by an ionic polymer–metal composite caudal fin,” IEEE/ASME Transactions on Mechatronics, Vol. 15, No. 3, pp. 448-459, 2010.

[31] Yeom, S. W. and Oh, I. K., “A biomimetic jellyfish robot based on ionic polymer metal composite actuators,” Smart Materials and

Structures, Vol. 18, Paper No. 085002, 2009.

[32] M. Yu, H. Shen, Z. Dai, “Manufacture and Performance of Ionic Polymer-Metal Composites”, Journal of Bionic Engineering, Vol. 4, No. 3, pp. 143-149, 2007.

[33] A. Crespi, K. Karakasiliotis, A. Guignard, A. J. Ijspeert, "Salamandra Robotica II: An Amphibious Robot to Study Salamander-Like Swimming and Walking Gaits", IEEE Transactions on Robotics, Vol. 29, No. 2, pp. 308–320, 2013.

[34] S. Guo, M. Li, C. Yue, “Performance Evaluation on Land of an Amphibious Spherical Mother Robot in Different Terrains”, Proceedings of 2013 IEEE International Conference on Mechatronics and Automation, pp. 1173-1178, 2013.

[35] C. Iverach-Brereton, J. Baltes, J. Anderson, A. Winton, D. Carrier, " Gait design for an ice skating humanoid robot", Robotics and Autonomous Systems, Vol. 62, pp. 306–318, 2014.

[36] S. Guo, M. Li, C. Yue, "Underwater Performance Evaluation of an Amphibious Spherical Mother Robot ", Proceeding of 2013 IEEE International Conference on Information and Automation, pp. 1038-1043, Yinchuan, China, August 26-28, 2013.

[37] J. Kim, W. Chung, “Accurate and Practical Thruster Modeling for Underwater Vehicles”, Ocean Engineering, Vol. 33, pp. 566-585, 2006.

[38] C. P. Santos, V. Matos, “Gait transition and modulation in a quadruped robot: A brainstem-like modulation approach”, Robotics and Autonomous Systems, Vol. 59, pp. 620-634, 2011.

[39] K. Abdelnour, A. Stinchcombe, M. Porfiri, J. Zhang and S. Childress, “Wireless Powering of Ionic Polymer Metal Composites Toward Hovering Microswimmers”, IEEE/ASME Transactions on Mechatronics, Vol. 17, pp. 924-35, 2012.

[40] B. Gao, S. Guo, “Development of an Infrared Sensor-based Wireless Intelligent Fish-like Underwater Microrobot”, Proceedings of 2010 IEEE International Conference on Information and Automation, pp. 1314-1318, Harbin, China, June 20-23, 2010c.

[41] B. Tian, F. Zhang, X. Tan, “Design and development of an LEDbased optical communication system for autonomous underwater robots”, Proceedings of 2013 IEEE/ASME international conference on advanced intelligent mechatronics, pp.1558–1563, 2013.

[42] H. Brundage, “Designing a wireless underwater optical communication system”, Master’s thesis, Massachusetts Institute of Technology, Cambridge, MA, 2010.

[43] W.C. Cox, J.A. Simpson, C.P. Domizioli, J.F. Muth, B.L. Hughes, “An underwater optical communication system implementing Reed-Solomon channel coding”, Proceedings of 2008 OCEANS

conference, Boston, MA, pp. 1–6, 2008.

[44] M. Li, S. Guo, J. Guo, H. Hirata, H. Ishihara, “Development of a Biomimetic Underwater Microrobot for a Father-son Robot System”, Microsystem Technologies, DOI 10.1007/s00542-016-2817-3, 2016.

[45] M. Li, S. Guo, H. Hirata, H. Ishihara, “A Roller-skating/Walking Mode-based Amphibious Robot”, Robotics and Computer Integrated Manufacturing, doi:10.1016/j.rcim.2016.06.005, Vol. 44, pp. 17-29, 2017.

[46] M. Li, S. Guo, “A Wireless Biomimetic Underwater Microrobot for a Father-son Robot System”, Proceedings of 2016 IEEE International Conference on Mechatronics and Automation, pp. 392-397, August 7-10, 2016.

[47] U. A. Korde, “Study of a jet-propulsion method for an underwater vehicle”, Ocean Engineering, Vol.31, No.10, pp.1205-1218, 2004.

[48] C. P. Santos, V. Matos, “CPG modulation for navigation and omnidirectional quadruped locomotion”, Robotics and Autonomous Systems, Vol. 60, No. 6, pp. 912-927, 2012.

[49] S. Yu, S. Ma, B. Li, Y. Wang, “An amphibious snake-like robot with terrestrial and aquatic gaits”, 2011 IEEE International Conference on Robotics and Automation (ICRA), pp. 2960 - 2961, 2011.

[50] C. Zhou, K. Low, “Better Endurance and Load Capacity: An Improved Design of Manta Ray Robot (RoMan-II)”, Journal of Bionic Engineering, Vol.7, Supplement, pp. 137-144, 2010.

[51] D.R. Yoerger, J.G. Cooke, J.-J.E. Slotine, “The influence of thruster dynamics on underwater vehicle behavior and their incorporation into control system design”, IEEE Journal of Ocean Engineering, Vol.15, No.3, pp. 167-178, 2009.

[52] W. Zhou, W. Li, “Micro ICPF actuators for aqueous sensing and manipulation”, Sensors and Actuators A: Physical, Vol. 114, No. 2-3, pp. 406-412, 2004.

[53] S. Kim, I. Lee and Y. Kim, “Performance enhancement of IPMC actuator by plasma surface treatment,” Journal of Smart Material and Structures, Vol. 16, pp.N6-N11, 2007.

[54] D. Lee, G. Kim, D. Kim, H. Myung, H. Choi, “Vision-based object detection and tracking for autonomous navigation of underwater robots.”, Ocean Engineering, Vol. 48, pp. 59–68, 2012.

[55] Y. Li, S. Staicu, "Inverse dynamics of a 3-PRC parallel kinematic machine", Nonlinear Dynamics, Vol. 67, No. 2, pp. 1031-1041, 2012.

[56] S. Guo, M. Li, L. Shi and S. Mo, “A Smart Actuator-based Underwater Microrobot with Two Motion Attitudes”, Proceedings of 2012 IEEE International Conference on Mechatronics and

Automation, pp.1675-1680, 2012.

[57] G. Antonelli, S. Chiaverini and N. Sarkar, “External Force Control for Underwater Vehicle-Manipulator Systems”, IEEE Transactions on Robotics and Automation, Vol. 17, pp. 931-38, 2001.

[58] B. Jun, P. Lee, S. Kim, “Manipulability analysis of underwater robotic arms on ROV and application to task-oriented joint configuration”, Journal of Mechanical Science and Technology, Vol. 22, pp. 887-894, 2008.

[59] M. Li, S. Guo, C. Yue, “A Roller Skating Mode-based Amphibious Spherical Robot”, Proceedings of 2014 IEEE International Conference on Mechatronics and Automation, pp. 1957-1961, August 3-6, Tianjin, China, 2014.

[60] A. Villanueva, C. Smith and S. Priya, “A biomimetic robotic jellyfish (Robojelly) actuated by shape memory alloy composite actuators”, Bioinspiration &Biomimetics, Vol. 6, No. 3, 036004, pp.1–16, 2011.

[61] N. Kamamichi, M. Yamakita, K. Asaka and Z. Luo, “A snake－like swimming robot using IPMC actuator/sensor”, Proceedings of the 2006 IEEE International Conference on Robotics and Automation, pp. 1812－1817, 2006.

[62] H. Nakadoi, A. Sera, M. Yamakita, K. Asaka, Z. Luo and K. Ito, “Integrated Actuator－Sensor System on Patterned IPMC Film:

Consideration of Electronic Interference”, Proceedings of the 2007 4th IEEE International Conference on Mechatronics, pp. 4280007, 2006.

[63] H. Cilingir, Y. Menceloglu, M. Papila, “The effect of IPMC parameters in electromechanical coefficient based on equivalent beam theory”, Journal of Electroactive Polymer Actuators and Devices (EAPAD), Proc. of SPIE. Vol. 6927, 69270L, 2008.

[64] S. Guo, Y. Okuda, W. Zhang, X. Ye, K. Asaka, “The Development of a Hybrid Underwater Micro Biped Robot”, Journal of Applied Bionics and Biomechanics, Vol.3, No.3, pp. 143-150, 2006.

[65] A. J. Healey and D. Lienard, “Multivariable sliding mode control for autonomous diving and steering of unmanned underwater vehicles”, IEEE Journal of Oceanic Engineering, Vol. 18, No. 3, pp. 327-339, 1993.

[66] Özgür YILDIZ, R. Bülent GÖKALP, and A. Egemen YILMAZ. “A Review on Motion Control of the Underwater Vehicles”, IEEE International Conference on Electrical and Electronics Engineering 2009, pp. 337-341, 2009.

Publication List

International Journal Papers

1. **Maoxun Li**, Shuxiang Guo, Jin Guo, Hideyuki Hirata, Hidenori Ishihara, “Development of a Biomimetic Underwater Microrobot for a Father-son Robot System”, Microsystem Technologies, DOI 10.1007/s00542-016-2817-3, 2016.
2. **Maoxun Li**, Shuxiang Guo, Hideyuki Hirata, Hidenori Ishihara, “Design and Performance Evaluation of an Amphibious Spherical Robot”, Robotics and Autonomous Systems, doi:10.1016/j.robot.2014.11.007, Vol. 64, pp. 21–34, 2015.
3. **Maoxun Li**, Shuxiang Guo, Hideyuki Hirata, Hidenori Ishihara, “A Roller-skating/Walking Mode-based Amphibious Robot”, Robotics and Computer Integrated Manufacturing, doi:10.1016/j.rcim.2016.06.005, Vol. 44, pp. 17-29, 2017.
4. Liwei Shi, Shuxiang Guo, **Maoxun Li**, Shilian Mao, Nian Xiao, Baofeng Gao, Zhibin Song, Kinji Asaka, “A Novel Soft Biomimetic Microrobot with Two Motion Attitudes”, Sensors, Vol. 12, No. 12, pp. 16732-16758, 2012.
5. Chunfeng Yue, Shuxiang Guo, **Maoxun Li**, Yaxin Li, Hideyuki Hirata, Hidenori Ishihara, “Mechantronic System and Experiments

of a Spherical Underwater Robot: SUR-II”, Journal of Intelligent and Robotic Systems, pp. 325-340, 2015.

6. Liwei Shi, Shuxiang Guo, Shilian Mao, **Maoxun Li**, and Kinji Asaka, “Development of a Lobster-inspired Underwater Microrobot”, International Journal of Advanced Robotic Systems, Vol.10, DOI: 10.5772/54868, 44:2013, pp. 1-15, 2013.
7. Liwei Shi, Shuxiang Guo, Shilian Mao, Chunfeng Yue, **Maoxun Li**, Kinji Asaka, “Development of an Amphibious Turtle-Inspired Spherical Mother Robot”, Journal of Bionic Engineering, Vol.10, No.4, pp. 446-455, 2013.

International Conference Papers

8. **Maoxun Li**, Shuxiang Guo, Chunfeng Yue, “A Roller Skating Mode-based Amphibious Spherical Robot”, Proceedings of 2014 IEEE International Conference on Mechatronics and Automation, pp.1957-1961, August 3-6, Tianjin, China, 2014.
9. **Maoxun Li**, Shuxiang Guo, Kazuhiro Yamashita, “Insect-inspired Biomimetic Underwater Microrobots for a Father-son Robot System”, Proceedings of 2015 IEEE International Conference on Mechatronics and Automation, pp.964-969, August 2-5, Beijing, China, 2015.
10. **Maoxun Li**, Shuxiang Guo, “A Wireless Biomimetic Underwater Microrobot for a Father-son Robot System”, Proceedings of 2016 IEEE International Conference on Mechatronics and Automation, pp. 392-397, August 7-10, 2016.
11. Shuxiang Guo, **Maoxun Li**, Liwei Shi, Shilian Mao, Chunfeng Yue, "Performance Evaluation on Land of an Amphibious Spherical Mother Robot", Proceedings of 2013 ICME International Conference on Complex Medical Engineering, pp. 602-607, May, 2013.
12. Shuxiang Guo, **Maoxun Li**, Chunfeng Yue, "Underwater Performance Evaluation of an Amphibious Spherical Mother Robot", Proceeding of the IEEE International Conference on

Information and Automation, pp. 1038-1043, August, 2013.

13. Shuxiang Guo, **Maoxun Li**, Chunfeng Yue, "Performance Evaluation on Land of an Amphibious Spherical Mother Robot in Different Terrains", Proceedings of 2013 IEEE International Conference on Mechatronics and Automation, pp. 1173-1178, August, 2013.
14. Shuxiang Guo, **Maoxun Li**, Liwei Shi, Shilian Mao, "Development of a Novel Underwater Biomimetic Microrobot with Two Motion Attitudes", Proceedings of the 2012 ICME International Conference on Complex Medical Engineering, pp. 763-768, July, 2012.
15. Shuxiang Guo, **Maoxun Li**, Liwei Shi, Shilian Mao, "A Smart Actuator-based Underwater Microrobot with Two Motion Attitudes", Proceedings of 2012 IEEE International Conference on Mechatronics and Automation, pp.1675-1680, August, 2012.
16. Chunfeng Yue, Shuxiang Guo, **Maoxun Li**, and Yaxin Li, "Characteristics Evaluation of a Biomimetic Microrobot for a Father-son Underwater Intervention Robotic System", Proceedings of the 2015 IEEE/RSJ International Conference on Intelligent Robots and Systems (IROS), pp. 171-176, Sept 28 - Oct 2, 2015.
17. Chunfeng Yue, Shuxiang Guo, Yaxin Li, **Maoxun Li**, "Bio-Inspired Robot Launching System for a Mother-Son Underwater Manipulation Task", Proceedings of 2014 IEEE International

Conference on Mechatronics and Automation, pp.174-179, August, 2014.

18. Chunfeng Yue, Shuxiang Guo, **Maoxun Li**, "ANSYS FLUENT-based Modeling and Hydrodynamic Analysis for a Spherical Underwater Robot", Proceedings of 2013 IEEE International Conference on Mechatronics and Automation, pp.1577-1581, August, 2013.

19. Chunfeng Yue, Shuxiang Guo, **Maoxun Li**, Liwei Shi, "Electrical System Design of a Spherical Underwater Robot (SUR-II)", Proceeding of the IEEE International Conference on Information and Automation, pp. 1212-1217, August, 2013.

20. Chunfeng Yue, Shuxiang Guo, **Maoxun Li**, Yaxin Li, "Passive and Active Attitude Stabilization Method for the Spherical Underwater Robot (SUR-II), Proceeding of the IEEE International Conference on Robotics and Biomimetics (ROBIO), pp.1019-1023, December, 2013.

21. Shuxiang Guo, Shilian Mao, Liwei Shi, **Maoxun Li**, Chunfeng Yue, "Development of a Spherical Amphibious Mother Robot", Proceedings of 2013 ICME International Conference on Complex Medical Engineering, pp.614-619, May, 2013.

22. Liwei Shi, Yanlin He, Shuxiang Guo, Hiroki Kudo, **Maoxun Li**, and Kinji Asaka, "IPMC Actuator-based a Movable Robotic Venus

Flytrap", Proceedings of 2013 ICME International Conference on Complex Medical Engineering, pp. 375-378, May, 2013.

23. Shuxiang Guo, Shilian Mao, Liwei Shi, **Maoxun Li**, "Design and Kinematic Analysis of an Amphibious Spherical Robot", Proceedings of 2012 IEEE International Conference on Mechatronics and Automation, pp. 2214-2219, August, 2012.

24. Shuxiang Guo, Shilian Mao, Liwei Shi, **Maoxun Li**, "Development of an Amphibious Mother Spherical Robot Used as the Carrier for Underwater Microrobots", Proceedings of the 2012 ICME International Conference on Complex Medical Engineering, pp. 758-762, July, 2012.

Biographic Sketch

Maoxun Li received the B.S. degree in electrical engineering and automation from Harbin Engineering University, China, in 2011, and the M.S. degree in intelligent machine system from Kagawa University, Japan, in 2014, respectively. Currently, she is a Ph.D. candidate in intelligent machine at Kagawa University, Japan. She researches on underwater microrobots powered by smart actuators, such as IPMC (ionic polymer metal composite) actuators, and amphibious spherical robots for industry and biomedical applications. Her current research interests include an amphibious spherical robot and the father-son robotic system. She has published about 26 refereed journal and conference papers in the recent years.